CHARACTERIZATION OF PERIODIC DISTURBANCES IN ROLLING ELEMENT BEARINGS

by

Nicholas A. Kirsch

B.S. in Mathematics, St. Vincent College, 2008

B.S. in Mechanical Engineering, University of Pittsburgh, 2009

Submitted to the Graduate Faculty of

Swanson School of Engineering in partial fulfillment

of the requirements for the degree of

Master of Science

University of Pittsburgh

2012

UNIVERSITY OF PITTSBURGH

SWANSON SCHOOL OF ENGINEERING

This thesis was presented

by

Nicholas A. Kirsch

It was defended on

October 14, 2011

and approved by

Daniel G. Cole, Ph.D. Assistant Professor

Jeffrey S. Vipperman, Ph.D. Assistant Professor

Stephen J. Ludwick Jr., Ph.D. Lecturer

Thesis Advisor: Daniel G. Cole, Ph.D. Assistant Professor

CHARACTERIZATION OF PERIODIC DISTURBANCES IN ROLLING ELEMENT BEARINGS

Nicholas A. Kirsch, M.S.

University of Pittsburgh, 2012

The objective of this research is to observe and characterize periodic fluctuations in friction force of ball-element bearings that occur during velocity tracking motion. It is proposed that this periodic fluctuation in friction force is caused by the motion of the balls. We hope to show this relation by demonstrating that the frequency of the periodic fluctuation is equal to the frequency of the balls passing a position in the race.

To illustrate the relation between the fluctuating friction force and the motion of the balls, a testbed has been built to measure friction force, ball passage rate, and velocity error during velocity tracking motion. The velocity error will be calculated from the measurement of position, and may show how the periodic fluctuations in friction force act like a periodic disturbance to the velocity. This paper will discuss the design and fabrication of the testbed, and the resulting measured signals that will be processed to determine their periodic content and to show how they are correlated. However, before inspecting the test results, some qualitative analysis of the system and models of the measured signals will be discussed to give insight into what we may expect from the results of the velocity tracking tests.

An optical sensor has been designed and built to detect the motion of the balls in the race. The optical sensor measures the light reflected off the surface of a ball as it passes the sensing fiber. It was necessary to make some adjustments to the initial design of the sensor to correct for an instability in the signal. These adjustments, and the cause of the instability, will be discussed in this paper.

Some ball bearings display an odd sticking behavior, where the friction force greatly increases beyond the approximated static friction force. This sticking behavior will be discussed, and how it relates to the motion of the balls in the race will be illustrated. It will also be discussed how the spectral density of friction force can be used to evaluate the performance of a bearing.

TABLE OF CONTENTS

LIST OF TABLES

LIST OF FIGURES

1.0 INTRODUCTION

Rolling element bearings are important components of many mechanical devices. They allow devices to make constrained relative movements while minimizing wear that can result due to friction. Some linear stages that use rolling element bearings are capable of one axis motion with micrometer precision; however, some applications of linear stages require greater precision. In the field of metrology, the science of measurements, to obtain a high degree of accuracy for measurements taken during tracking velocity motion it is necessary to maintain the desired tracking velocity, to a certain degree of accuracy that depends on the size of the features being measured. Objects, such as integrated circuits or MEMS devices, have features on the order of tens of microns. To scan these small features a linear stage capable of maintaining a constant velocity with a high degree of accuracy is required. For these high precision applications linear stages that use non-contact bearings, such as air bearings and magnetic bearings, are favored. This is because they are capable of tracking a velocity with less variance than rolling element bearings. Although air and magnetic bearings are capable of tracking a velocity with less variance than rolling element bearings, due to reduced friction during motion, they are considerably more expensive due to the higher tolerances that are necessary in their manufacturing. Presently, rolling element bearings provide a considerably higher performance/cost ratio than non-contact bearings, which is why they are more commonly used. Improving how well linear stages that use rolling element bearings can track a velocity would make precision linear motion available at a lower cost.

Linear stages that use rolling element bearings have seen considerable improvements in precision due to refined manufacturing techniques; however, their precision could be increased using control methods. In this paper precision is defined as how well a linear stage can track a velocity. A linear stage that varies greatly from the tracking velocity during tracking velocity

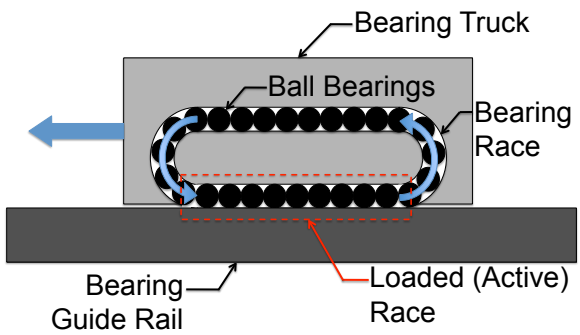

Figure 1: The ball bearing experiences fluctuating friction forces as the balls transition from the unloaded region to the loaded region of the race.

motion would be considered to have poor precision. Improving the precision of linear stages that use rolling element bearings with control methods, instead of increasing tolerances in manufacturing, could improve precision without increasing the cost of production typically associated with higher tolerances. In this thesis, it is proposed that linear bearings that use ball rolling elements experience fluctuations in friction force as the balls move from the unloaded race to the loaded race, thus causing poor precision during velocity tracking. This is illustrated in Figure 1, which shows a simple schematic of a rolling element bearing that uses ball elements. For velocity tracking motion the balls move through the race at a constant speed. This means that if the fluctuating friction force is related to the motion of the balls, as proposed, then the fluctuations will be periodic. In this thesis, the fluctuating friction force, which acts like a disturbance in the tracking velocity, will be discussed as a periodic disturbance whose frequency is equal to the frequency of the balls traveling through the race. The goal of this research is to observe and characterize this periodic disturbance found in linear stages using rolling element bearings.

The frequency of the balls passing a position in the race can be determined by dividing the velocity of each ball by their distance from center to center. If the bearing truck is moving at a constant velocity, v, relative to the guide rail then the balls will move within

the race at a velocity of $v/2$. If the balls are close-packed, meaning there is no space between each ball, then the distance between each ball will simply be their diameter. For a constant tracking velocity, v, and for balls with diameter d the ball frequency is

$$f = \frac{v}{2d}. \tag{1.1}$$

This expression for the frequency of the balls passing a position in the race assumes that both the velocity and spacing between the balls are constant. However, it is known that not only can the velocity vary about the reference velocity, but the distance between balls can also vary. The variation in spacing between the balls is due to balls not being closely packed within the race.

Since the distance between the balls can vary, it is necessary to measure the balls as they travel through the race. This allows us to determine how the inconsistent spacing between the balls affects the variation in the frequency. To measure the ball motion in the race, an optical sensor has been designed and built to detect the balls passing a position in the race. The optical sensor allows for more accurate measurements of the rate at which the balls are traveling through the race than the previously discussed estimation in Equation (1.1). Although the measurements allow us to determine the frequency of the balls traveling through the race more accurately, the dynamic based estimation expressed in Equation (1.1) can still be used to predict the approximate frequency. Also, the physical characteristics of the bearings, such as the amount of extra space in the race, could be used to determine limitations to the variation in the frequency.

For ball bearings, whose distance between each ball can vary, it is suggested that the center frequency of the fluctuations will occur at a frequency that is dependent upon the average distance between the balls in the race. Similar to Equation (1.1) the center frequency is

$$f_c = \frac{v}{2d_{\text{avg}}}, \tag{1.2}$$

where d_{avg} is the average distance between each ball. The average distance between the centers of each ball is calculated as

$$d_{\text{avg}} = d + \frac{d_{\text{ext}}}{N_B}, \tag{1.3}$$

where d_{ext} is the total extra space between balls within the race and N_B is the number of balls within the race. For a THK SR25W bearing, which is used in the experiments, $d = 4\,\text{mm}$, $d_{\text{ext}} = 2\,\text{mm}$, and $N_B = 36$; thus $d_{\text{avg}} = 4.056\,\text{mm}$ and the center frequency of the periodic disturbance for tracking velocity motion is $f_c = \frac{v}{8.112\,\text{mm}} = 0.123v$.

Knowing how much the distance between balls can vary allows us to create an expression for how much the frequency can vary. If the balls are evenly spaced then the distance between the balls from their centers would be 4.056 mm, as determined from Equation (1.3) and the characteristics of an SR25W bearing. Assuming that the balls spacing will vary about their average, the variance in their distance can be approximated as plus or minus the surface to surface distance. Knowing that the distance between each ball can vary by d_{var}, which for this ball bearing is $\pm 0.056\,\text{mm}$, and using Equation (1.2), we can calculate f_d, the frequency of the disturbance, to be

$$f_d = \frac{v}{2}\left(\frac{1}{d_{\text{avg}} \pm d_{\text{var}}}\right) = v(0.123 \pm 0.002). \tag{1.4}$$

The distance that each ball can vary, d_{var}, is determined from the number of balls in a race, the length of the race, and the total extra space between balls in the race. Equation (1.4) allows us to approximate the frequency range of the balls traveling in the race. This will be valuable when inspecting the frequency content of the friction force, the tracking velocity error, and the rate of the balls traveling through the race. If the signals contain some periodic content at the frequency of the expected periodic disturbance it can be concluded that the disturbance is related to the motion of the balls in the race.

The signal from the optical sensor may also be used to determine how the motion of the balls traveling through the race are correlated to the velocity error and the friction force between the guide rail and the ball bearing during velocity tracking motion. A testbed has been designed and built to make measurements of velocity error and friction force to show this correlation.

In designing the testbed it was important to remember that the desired measurements needed to be obtained while the ball bearing moved at a controlled constant velocity relative to the guide rail. The chosen design, discussed in Chapter 3, uses a linear air bearing table to move the guide rail while the ball bearing is held in position by a load cell. It was decided

it would be easier to move the guide rail instead of the ball bearing to create the relative motion between the guide rail and the ball bearing because this makes it unnecessary to move the sensors that are attached to the ball bearing. The air bearing table was ideal because it allowed the guide rail to be moved at a constant controlled velocity. Also, the linear encoder in the air bearing table can be used to determine the relative velocity error between the guide rail and the ball bearing.

2.0 BACKGROUND AND STATE OF THE ART

2.1 INTRODUCTION

In this research we desire to measure the friction force of a rolling element bearing during velocity tracking motion. Although friction has been measured and studied for a long time, dating as far back as Guillaume Amontons in 1699 [9], its mechanisms are still not fully understood. Some friction phenomena, which have been observed in research, are Coulomb friction, static friction (stiction), viscous friction, the Stribeck effect, and hysteresis. Friction has two regimes where the different phenomena occur, the pre-sliding and sliding regime. In the pre-sliding regime the moving mass (slider) has not broken stiction, and friction force is primarily a function of the sliding mass's position with respect to the stationary component (stator). Friction phenomena such as stiction and hysteresis are apparent in this regime. In the sliding regime the stiction has been exceeded and now the friction force is primarily a function of the relative velocity between the stator and slider. Friction phenomena such as Coulomb friction, viscous friction, and the Stribeck effect are apparent in this regime.

Coulomb friction, developed by Coulomb in 1785 [7], can be described as

$$F_c = -\text{sgn}(v)\mu_c F_n, \tag{2.1}$$

where F_c is the Coulomb friction, μ_c is the Coulomb friction coefficient, and F_n is the normal force. Coulomb friction states that the friction force is dependent on the sign of velocity and the normal force. The Coulomb model of friction is often used to model friction because of its simplicity.

Stiction, which was first described by Morin in 1833 [24], describes the condition where although a force greater than Coulomb friction is being applied to the slider there is no

displacement. When a force greater that the static friction force is applied the slider will begin to move, indicating that it has left the pre-sliding regime and is now in the sliding regime.

Lubricants are used to reduce friction, and the wear of the bearing elements that can result due to friction. Viscous friction is a phenomenon that is caused by the viscosity of the lubricant used and was first described by Reynolds [30]. Viscous friction is proportional to the product of the velocity of the slider and the normal force. If no lubricant is used then this friction phenomenon will not be present.

In 1901 Stribeck observed that for low velocities, the kinetic friction force decreased continuously with increasing velocities [32]. Kinetic friction force refers to the force of friction that occurs between two materials in contact when there is some relative motion occurring. The effect observed by Stribeck is referred to as the Stribeck effect and the velocity where the friction force reaches its maximum is called the Stribeck velocity. Stribeck showed that the friction force also has a dependence the magnitude of the velocity.

The research of Hess and Soom showed that the friction force is lower for deceleration than for acceleration [16]. The hysteretic behavior of friction is apparent in the plots of friction versus velocity, and occurs in the regime which is referred to as the pre-sliding regime. It was also observed by Hess and Soom that the hysteresis loops become wider as the velocity variations become faster.

Much research has been done to better understand friction, using many different measurement methods. Some researchers have measured friction using a load cell [8, 10, 13, 14, 15, 29]. Typically in these setups the stator held in position using a load cell, which measures the forces between the stator and slider as the slider is moved. This method directly measures the forces acting on the stator; however, friction may not be the only force that is measured. If the load cell is attached to the actuator of the slider, instead of being attached to the stator, then inertial forces are also measured. In some cases, such as cases where the acceleration is small, inertial forces can be ignored. Also, if the mass of the moving object is known and the acceleration can be directly measured, or calculated from another measurement, then the frictional forces can be isolated from the forces measured by the load cell.

Accelerometers, which are very similar to load cells, can also be used in some research to calculate friction force from acceleration [5, 15]. Bucci et al. actuated the base of a rolling element linear stage while the acceleration of the top of the stage was measured using an accelerometer. Here the only forces acting on the top of the stage are the inertial forces and friction forces. Since the mass of the top of the stage can be measured, the friction of the rolling element bearings can be determined from the measured acceleration of the top of the stage.

Other researches have measured friction force using strain gauges, which are used to determine force from a measurement of strain [3, 19, 23]. By placing a strain gauge onto a flexure joint that is controlling the motion of the slider the friction force between the slider and stator can be determined. Changes in strain at the joint where the strain gauge is placed causes the resistivity of the strain gauge to change. From the change in the resistivity of the strain gauge the force applied can then be determined.

Since force is proportional to acceleration, which is position twice differentiated, it is possible to measure friction force by measuring the relative position between the stator and slider [11, 21, 22, 33, 34]. This is a non-contact method of determining the friction force, since many sensors that measure position are non-contact. However, numerically differentiating position twice to get acceleration often results in a signal with a lot of noise. Since force is proportional to the acceleration by the mass of the slider the calculated force signal would be very noisy.

A very simple, and commonly used method, for determining friction force in linear stages is to use the actuator current scaling method, which determines the actuator force from the actuator current [4, 12, 28, 31]. Since all linear stages use an actuator to control the motion of the slider this method can be used with all linear stages. It can also be used to determine the friction torque in angular bearings. Similar to some of other methods discussed, if the inertial force is not negligible, the mass of the moving part must determined so the friction force can be determined from the actuator force.

Although all of the discussed methods for measuring friction are different, as stated by Lampaert et al. [20] all friction testing devices have several features in common.

- They provide a means to fix or support the two bodies for which friction data are desired.
- They can move the two bodies relative to one another in a controlled fashion.
- They can apply a normal force.
- They can measure or infer the magnitude of the tangential friction force.

This chapter will discuss the research that have used the different friction measurement methods, mentioned previously, in detail. The method for determining the friction force and what has hoped to observed will be discussed. The different methods will be broken up into two sections. The first will discuss friction measurement methods that are used to measure the friction force between two materials, and the second will discuss product friction testing apparatuses.

Another important consideration discussed by Lampaert et al. is that it is impossible to completely decouple the dynamics of the actuator and some sensors from the friction force [20]. Although the dynamics of friction, actuators, and sensors cannot be completely decoupled it is possible to minimize their interactions. It will also be discussed what steps, if any, have been taken to minimize the coupling between the dynamics of actuators and sensors from the friction dynamics.

2.2 MATERIAL FRICTION TESTING APPARATUSES

Many test apparatuses have been built and used to research the frictional properties of materials. These test apparatuses were built with many different purposes. Some were built to directly measure the friction force between two surfaces in contact, others were built to determine the coefficients of friction between materials, and some were built to observe and characterize frictional dynamics. This section will discuss in detail the design of each test apparatus and what characteristic of friction they are trying to measure or observe.

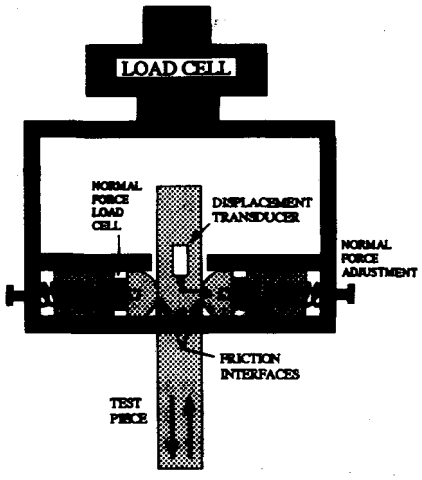

Figure 2: The schematic shown here is the double-shear friction fixture of Dupont et al. that was used to measure the friction force of line contacts of hardened tool steel (*Source:* [10]).

As previously mentioned one method for measuring friction force is to use a load cell. In material friction testing the research by Dupont et al. [10] and Ramasubramanian et al. [29] both use load cells to measure friction force. The research of Dupont et al. [10] used a double-shear friction fixture, as shown in Figure 2 to measure the friction force of line contacts of hardened tool steel. In the test apparatus of Dupont et al. a load cell is clamped to a rigid frame while the test piece is clamped to a hydraulic actuator. Two semi-cylindrical riders hold the test piece and act as the friction interface. As the test piece is actuated the friction force between the test piece and the and the riders resists the motion of the test piece. The test apparatus also has a mechanism so that the normal force between the test piece and the riders can be adjusted. Other sensors, such as another load cell that measures the normal force, and a displacement sensor that measures the displacement of the test piece, are used so that the relationships between friction force, position, and normal force can be shown.

For the test apparatus of Dupont et al. the coupling between the dynamics of the friction and the dynamics of the frame is minimized by making the frame rigid. Dupont et al. do not discuss how inertial forces affect the force measurement of the load cell. If the acceleration of the test piece is large the inertial forces would be large and would need to be isolated from the force measured by the load cell.

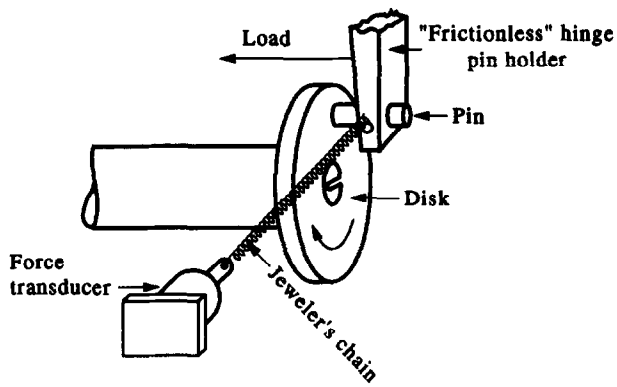

Figure 3: Shown is a schematic for a friction testing apparatus proposed by Godfrey that measures the friction between the disk and the pin using a load cell that is attached to the pin holder (*Source:* [13]).

Godfrey [13] measured the friction force using a pin-on-disk tribometer, which uses a load cell to measure the friction force between the pin and disk specimens. The pin is held in position, in contact with the rotating disk, by a hinge pin holder that can be used to change the load of the pin on the disk. The load cell, which is attached to the pin holder, measures the friction force that results from the motion of the disk and the load between the pin and the disk. The measurements from the pin-on-disk tribometer are used to obtain the kinetic coefficient of friction of the pin and disk specimens.

One issue with measuring friction force using a pin-on-disk tribometer is that friction force oscillations are often observed. It has been concluded that these oscillations corresponded with the disk rotation rate, and are a result of non-uniform conditions around the circular wear track on the disk. These friction force oscillations often result in large uncertainty in the calculated values of the kinetic coefficients of friction. Although Godfrey used the pin-on-disk tribometer only to determine kinetic coefficients of friction the tribometer

can be used to study static and dynamic friction characteristics. The biggest limit of Godfrey's tribometer is that the normal force loading between the pin and disk is asymmetric, and causes oscillations in the friction force measured by the force transducer. It is likely that as the normal force is increased the amplitude of the friction force oscillations increase. Also, to know the relative displacement between the disk and the pin exactly the displacement of the pin must also be measured.

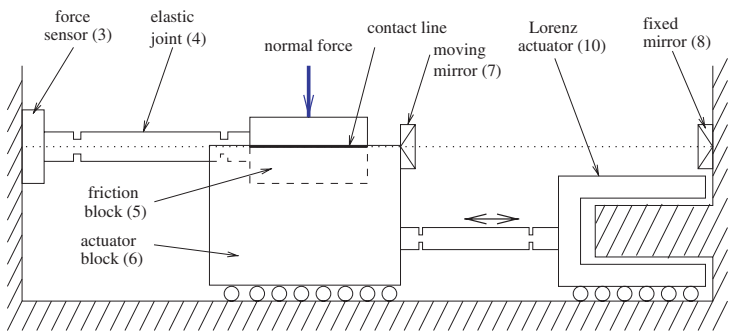

(a)

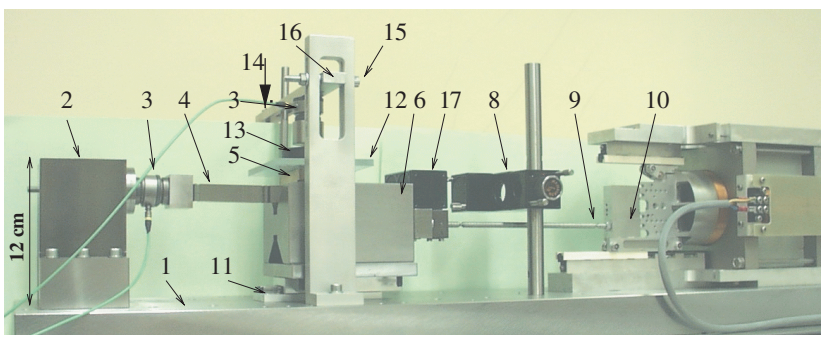

(b)

Figure 4: This tribometer, designed by Lampaert et al., uses a load cell (Feature 3) to measure the friction force between two materials in line contact. The friction block (Feature 5), which is held in position by a load cell, sits on the actuator block (Feature 5), which is actuated using a Lorenz actuator (Feature 10) (*Source:* [20]).

Another friction testing apparatus which uses a load cell is the tribometer designed by Lampaert et al. [20]. The friction block, which is held in position by a load cell, sits on top of the actuator block that is actuated by a Lorenz actuator, which is a linear electromagnetic motor where the actuator force is linearly proportional to the current. Relative position is

measured using interferometry, and strain gauges are placed on the elastic joint. Lampaert et al. states that the differences between their tribometer and standard tribometers are: (i) the possibility to apply different force or desired displacement trajectories to the block, (ii) a separation between the actuation part and the friction part, (iii) a separation of the normal load and the tangential load, and (iv) a separation of the force measurement and the relative displacement measurement. The tribometer of Lampaert et al. is capable of observing the break-away force, pre-sliding and sliding behavior, the transition from pre-sliding to sliding, and the stick-slip phenomena. The test apparatus of Lampaert et al. is certainly one of the most comprehensive friction measurement devices because it is capable of observing every friction behavior that has been discussed. It is also an excellent tribometer because the relative motion between the stator and slider can be controlled, the normal force can be controlled, and it can take DC friction force measurements because it uses strain gauges in line with piezoelectric load cells.

The research of Ramasubramanian et al. [29] measured the friction between a roller and flexible web. This friction sensor designed by Ramasubramanian et al. is referred to as the tribosensor, and it is used to acquire real-time friction coefficient measurement between materials, where the flexible web is being processed or manufactured at high speeds. This sensor can be used in the manufacturing of materials to determine their coefficients of friction as the materials are being manufactured. The friction force between the roller and the web is determined from a load cell that measures the axial load of the roller. Another load cell is used to measure the normal force between the roller and the web and an angular encoder is used to measure the angle of the roller.

Although the results of the research by Ramasubramanian et al. showed good agreement with other experimental results there is no mention of whether the friction force between the roller and yoke is negligible. The bearings of the roller would certainly introduce friction that would be measured by the load cell. However, since the results of Ramamsubramanian

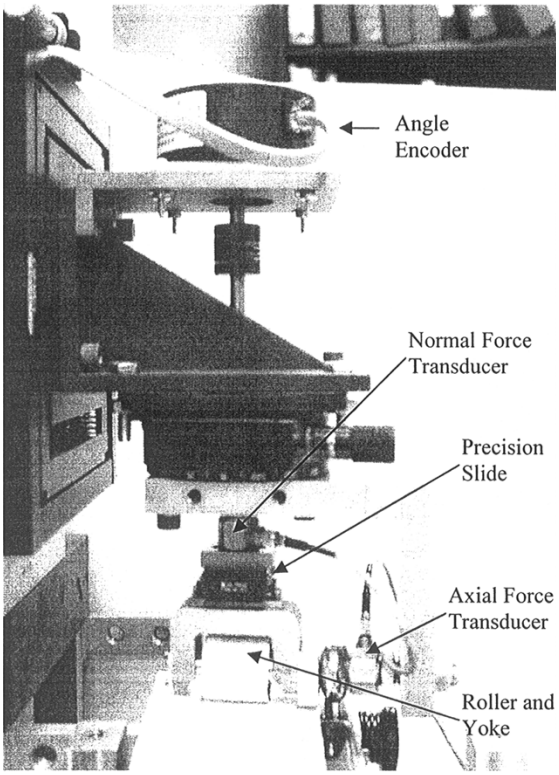

Figure 5: The friction force between a roller and a flexible web is measured using a load cell in the test apparatus designed by Ramasubramanian et al. [29] (*Source:* [29]).

et al. were in agreement with other experimental results it is likely that the friction between the roller and yoke is negligible in comparison to the friction between the roller and the web. Since the tribosensor is used to measure the coefficient of friction between two materials, which is a static property, it is not necessary to attempt to minimize the frictional dynamics from the dynamics of the test apparatus.

The research of de Vicente et al. [8] used a mini-traction machine (MTM), shown in Figure 6, to measure sliding and rolling friction between a steel ball and a silicone elastomer disc. This test apparatus is very similar to the pin-on-disk tribometer used by Godfrey [13]. However, the test apparatus of Godfrey can only measure sliding friction while the apparatus of de Vincente et al. is used to observe rolling and sliding friction. In the MTM a ball is loaded and rotated against the flat surface of a rotating disc immersed in lubricant

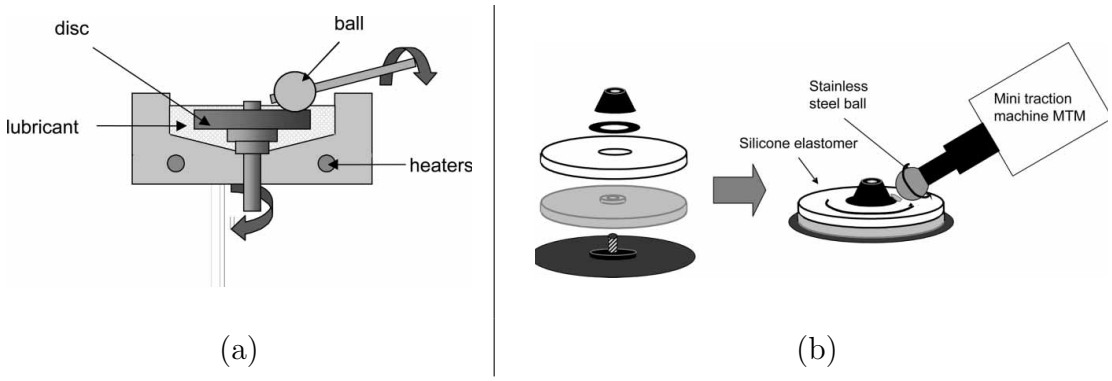

Figure 6: This mini-traction machine (MTM) was used by de Vincente et al. [8] to measure sliding and rolling friction between a steel ball and a silicone elastomer disc. The schematic diagram of the MTM (a) and the arrangement of the silicone elastomer disc holder (b) are both shown here (*Source:* [8]).

at a controlled temperature. The ball and the disc are driven independently to achieve any desired sliding-rolling speed combination. The friction force, which may occur due to rolling or sliding friction, is measured using load cells attached to the ball motor. Through combining four friction measurements the measurement of rolling friction can be separated from the measurement of sliding friction.

The MTM used by Vincente et al. is a good friction measurement apparatus because it can measure both sliding and rolling friction. Because the motion of the disc and ball can both be controlled the MTM can also be used to observe static and dynamic friction characteristics. The MTM is also good for friction measurement because it uses different measurement to determine friction force due to sliding and friction force due to rolling. Since rolling and sliding friction can be differentiated from one another it is possible to use the MTM to characterize rolling friction and sliding friction separately.

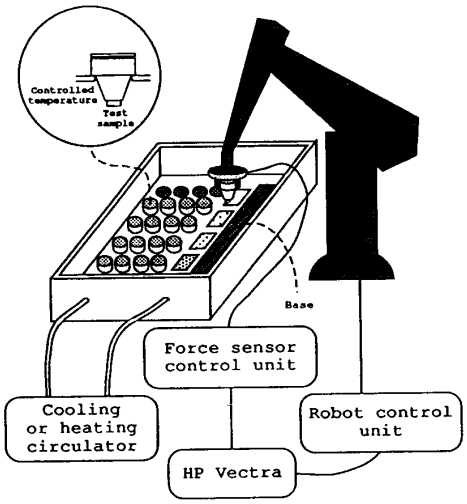

Figure 7: The test apparatus of Korpiharju et al. [19] uses a robotic arm with a six-component force/moment sensor head, which uses strain gauges to measure the forces, to measure the friction force between different materials (*Source:* [19]).

Some test apparatuses that have been used to research the friction of materials use strain gauges to make their force measurements. The research of Korpiharju et al. [19] uses a six-component force/moment sensor head that is attached to a robotic arm to measure the friction force between materials. The sensor head use an arrangement of strain gauges to measure the force/moment components. The sensor head can also measure the normal force between the two surfaces. This information can be fed to the robotic arm so that the normal force can be changed and controlled. The sensor head is actuated using a robotic arm so that the process of determining coefficients of friction between many different materials can be automated. Since the research of Korpiharju et al. is only looking to measure the coefficients of friction of materials, similar to the research of Ramasubramanian et al. [29], it is not necessary to attempt to minimize the coupling between the frictional dynamics and the dynamics of the robotic arm.

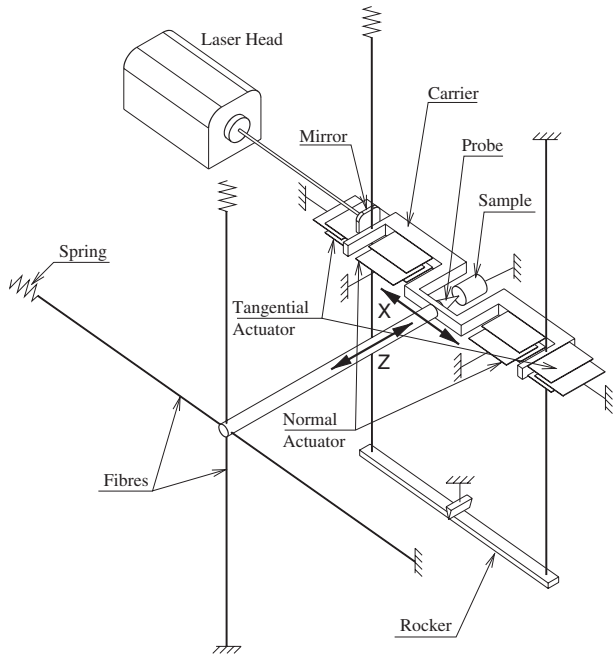

Figure 8: The test apparatus of Sidobre and Heyward [31] uses the current scaling method to determine the friction force between the probe and the sample (*Source:* [31]).

Another previously mentioned method for measuring friction force between two surfaces in contact is to convert the actuator current to the actuator force, using the current scaling method. One research that used actuator feedback to determine the friction force was the research by Sidobre and Heyward [31]. Sidobre and Heyward constructed an apparatus to investigate the behavior of junctions using a probe and a sample, each supported by leaf springs arranged orthogonally. The probe is actuated using comb actuators, and the friction force is determined from the electrostatic feedback of the comb actuators. The suspension of the probe provides a nearly perfect kinematic guidance in order to reduce the number of degrees of freedom to exactly two. This is done to simplify the modeling and calibration of the sensor. Also, the tunable suspension compliance is linear over the operating range, and parasitic terms due to mechanical hysteresis and gravity are eliminated. Since the suspension and actuators do not have any hysteresis any hysteresis that appears in the measurements are a result of friction. This sensor has three major contributors

of measurement noise; mechanical and sound vibration, interferometer intrinsic noise, and thermal drift. Sidobre and Heyward do an excellent job at minimizing the coupling between the frictional dynamics and the actuator and structural dynamics, which allows them to make dynamics measurements of friction. This tribometer can be used to observe many friction characteristics; however, its travel is limited by the size of the sample, the limitations of the kinematic coupling, and the limitations of the comb actuator.

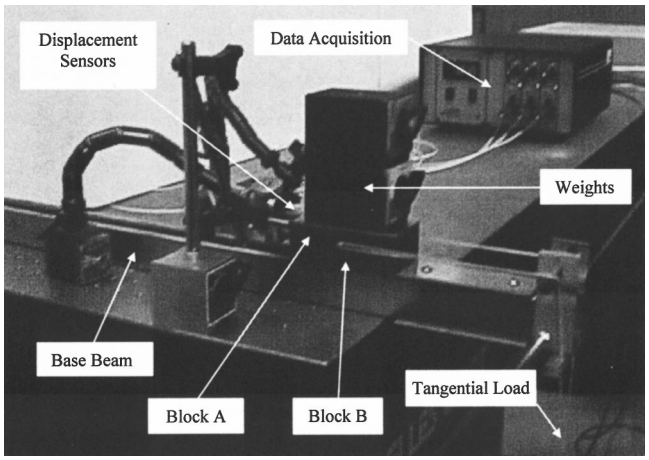

Figure 9: The test apparatus of Ni and Zhu [25] applies a tangential load to Block A that sits on Block B by adding water to a bucket attached to Block A. The relative displacement between the two blocks is measured using two capacitive proximity sensors (*Source:* [25]).

The apparatus used by Ni and Zhu [25] measures the friction force by controlling the applied load. Ni and Zhu attach a bucket to Block A (slider) that sits on top of Block B (stator), shown in Figure 9. A known amount of water is added to the bucket, increasing the friction force between the surfaces of Block A and Block B. The displacement of each block is measured using capacitive proximity sensors. The normal force between Block A and Block B is increased by adding weights to Block B. The apparatus of Ni and Zhu was used to study friction force in the stick-slip motion under different normal loads. The tangential load was increased by slowly adding water to the buck attached to Block A until the friction force would saturate, and Block A would begin to slide. Sliding was determined as the point where the displacement of Block A continues to increase, but the displacement of Block B would stop.

The apparatus of Ni and Zhu is good for observing stick-slip motion and the sticking regime. However, it cannot be used to observe any other characteristics such as hysteresis, which cannot be observed because the tangential load can only be controlled in one direction. Ni and Zhu did not mention how the momentum of the water being added to the bucket affected the applied load. Since there are no noticeable peaks in tangential load or displacement it is likely that the momentum of the water being added to the bucket is small, and therefore can be neglected. There is no mention of how Block B is adhered to the base beam, and how that may affect the measurements by introducing other dynamics. This apparatus is good for observing stick-slip motion, but because there is little control over the actuating force it would not be good for observing other friction characteristics.

2.3 PRODUCT FRICTION TESTING APPARATUSES

The previous section discussed several different material friction testing apparatuses that have been used in research. This section will discuss different methods used for testing friction that occurs in products, such as bearings. The methods discussed in this section are more relevant to my research since I will be measuring and observing the friction that occurs in ball element bearings.

First, product friction testing apparatuses that use load cells to measure friction will be discussed. In the research of Harnoy et al. [15] an apparatus for measuring dynamic friction in a lubricated journal bearing was described. The apparatus, which used load cells to measure friction force, was designed to test each of the parameters effect on dynamic friction so that the role of each can be assessed separately. The described apparatus allows for adjustable loading of the journal bearings and the friction of the journal bearings is isolated from any other friction present in the system. The shaft that is supported by the journal bearings is driven by a DC servo-motor through a timing belt and two pulleys.

The motor, timing belts, and pulleys will introduce some dynamics that will be observed in the load cell measurement. If the belts and pulleys are properly loaded their dynamics will

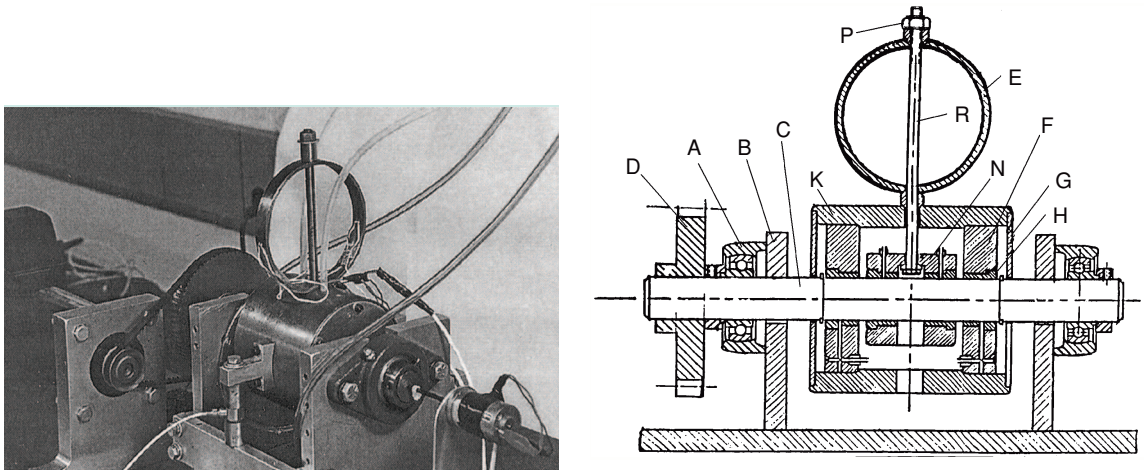

(a) (b)

Figure 10: This test setup designed by Harnoy et al. [14] uses a load cell to measure dynamic friction in a lubricated journal bearing. The load cell is attached to the outer bearing housing, K, and measures the torque that attempts to rotate the bearing housing. The elastic steel ring, E, is used to change the load between the journal bearings and shaft (*Source:* [15]).

be negligible compared to the frictional dynamics. This method is excellent for measuring the friction force in journal bearings, or even other types of rotary bearings, but this method clearly cannot be used for linear motion.

In a later research of Harnoy et al. [14] they discussed two more test apparatuses for measuring friction, the first uses a load cell and the second uses an accelerometer. For the first apparatus, which uses a load cell, a sliding table driven by a servomotor and a ball screw drive slides underneath a short, finely ground, cylindrical shaft. The shaft is held in position by a load cell, which measures the forces acting on the shaft in the direction of motion of the sliding table.

Similar to the previous work of Harnoy et al., this method of actuating will introduce some non-frictional dynamics that will be measured by the load cell. The frictional dynamics of the ball screw drive will likely also be measured by the load cell. If the magnitude of the friction in the ball screw drive is greater than the magnitude of the line contact friction then

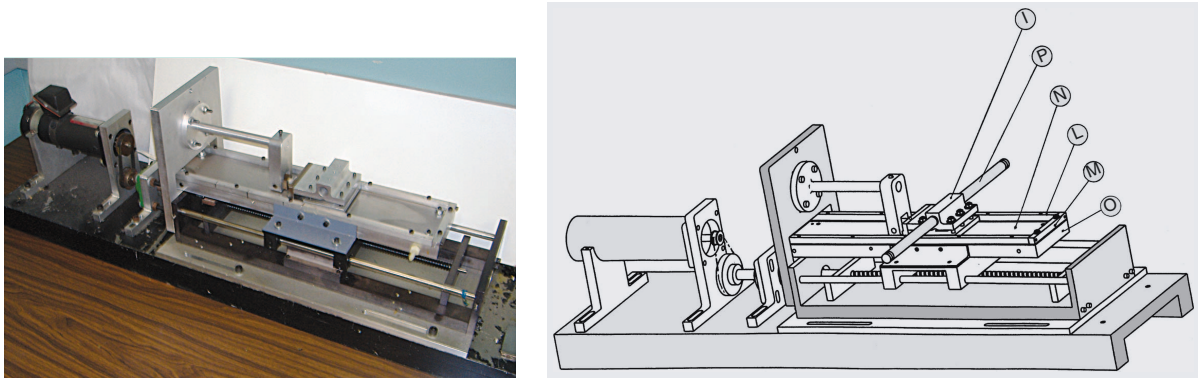

(a) (b)

Figure 11: A finely ground cylindrical shaft is held by housing assembly I, which is held in position by a load cell. The shaft sits on top of the flat friction surface, which is actuated by a screw drive. As the friction surface moves underneath the cylindrical shaft the friction force between them is measured by the load cell (*Source:* [14]).

it will be difficult to discern the line contact friction from the load cell measurement. Using an actuator that introduces minimal friction, such as an air bearing instead of a ball screw driven mechanical bearing stage, would be an excellent improvement to this test apparatus.

The second test apparatus of Harnoy et al. proposed a method where a reciprocating base, non-contacting velocity sensor, and accelerometer can be used to measure friction force. A test mass, with an accelerometer attached, is placed on the reciprocating base, whose motion can be controlled by an actuator. As the base moves the inertial forces of the test mass will act to move it independently of the base. If the relative displacement between the base and the test mass is small then the test mass is still in the sticking regime. If the relative displacement is large then the test mass has broken stiction, due to ample inertial forces, and is now in the sliding regime.

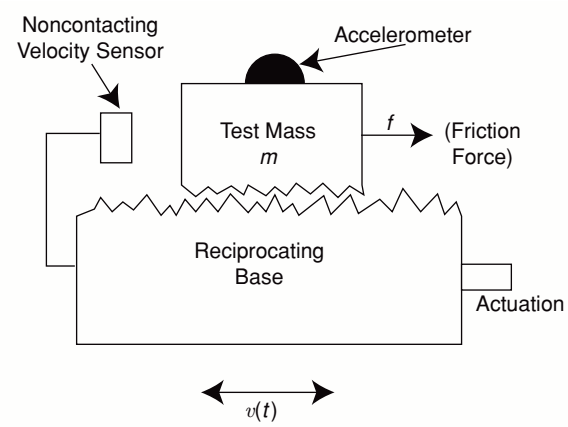

Figure 12: Shown is a schematic for a friction testing apparatus proposed by Harnoy et al. [14]. As the reciprocating base moves the test mass will move along with it, until inertial forces allow the test mass to break stiction. The friction force between the base and test mass can then be determined from the accelerometer signal (*Source:* [14]).

Although the motion of the base can be controlled it is difficult to create a desired relative displacement between the test mass and base using this apparatus. Also, it would be very challenging to use this test apparatus to observe friction characteristics that occur during constant relative velocity motion. This test apparatus proposed by Harnoy et al. is just a concept, and its design was not discussed in detail. The test apparatus was not built and not actual tests were conducted.

Bucci et al. [5] built a test apparatus similar to the conceptual friction testing apparatus proposed by Harnoy et al. The test apparatus of Bucci et al. used an air bearing stage to actuate the base of a crossed-roller bearing linear stage. The air bearing is ideal because it can make controlled motions and introduces minimal frictional effects. The friction force of the crossed-roller bearings is determined from an accelerometer, which is placed on top of the crossed-roller bearing stage. The linear encoder in the crossed-roller bearing stage is used to determine the relative displacement and velocity between the base and stage of the crossed-roller bearing stage.

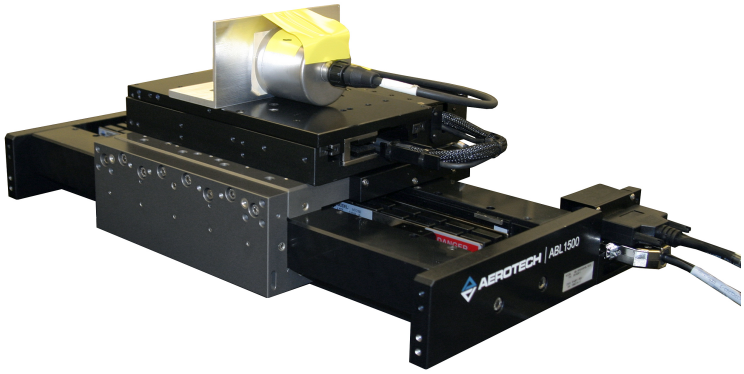

Figure 13: In this test apparatus by Bucci et al. [5] the air bearing actuates the base of the crossed-roller bearing stage. The friction force, present in the crossed-roller bearing stage, is determined from the signal measured by the accelerometer (*Source:* [5]).

The test apparatus of Bucci et al. minimizes the coupling between the actuator dynamics and the frictional dynamics by using an actuator whose controllable precision is significantly better than the precision of the crossed-roller bearings. Also, by measuring the mass of the crossed-roller stage and using the measurement from the accelerometer inertial forces can be determined and isolated from the frictional dynamics. This is a good method for measuring the friction force in crossed-roller bearing stages. However, similar to the conceptual test apparatus of Harnoy et al. the relative displacement and velocity between the stator and the slider cannot be controlled very well.

The test apparatus of Biyiklioğlu et al. [3] uses strain gauges to measure the friction force. Biyiklioğlu et al. used their test apparatus to measure the friction properties of journal bearings under dynamics loading conditions. The test apparatus allows the bearings to be tested at different dynamic loads, speeds, and lubricating conditions. Strain gauges were placed on tension bars attached to four, equidistantly placed, loading cylinder the held the shaft in position. The strain gauges were calibrated, prior to testing, by hanging known

weights from the tension bars. The tension bars are preloaded to ensure that the strain gauges are operating in a linear range. The shaft is actuated using a cam and belt-pulley system.

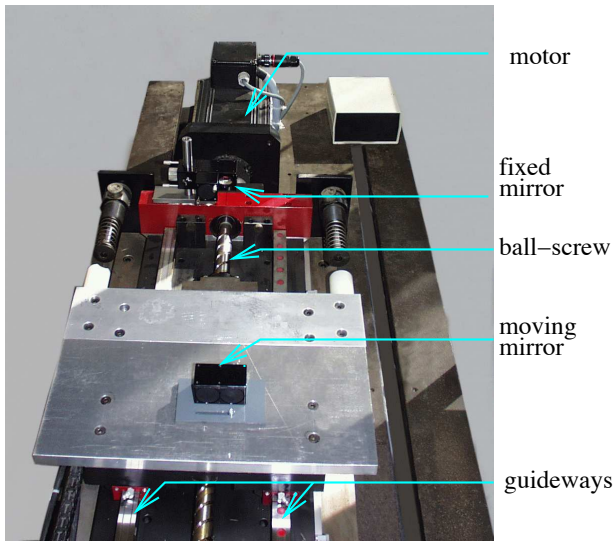

Figure 14: In the research of Lampaert et al. [21] the friction force of a machine tool table was determined from position, which was measured using interferometry (*Source:* [21]).

Another method for determining friction force is to use acceleration that is derived by numerically differentiating position twice. The research of Lampaert et al. [21] measured the friction force of a machine tool linear table system, shown in Figure 14 from the measurement of position, which is obtained using interferometry. The base of the tool table is actuated using a ball-screw drive. A mirror is placed on the tool table and a laser is placed on the base of the tool table. The interference pattern of the incident light from the laser and the light reflected by the moving mirror is used to determine the position of the tool table. A low velocity of 1 mm/s was used to minimize the inertial effects, which are not removed from the acceleration calculated from the measured position. The cogging force was identified by using the motor current and compensated for so that the only forces that remain are inertial forces, which are minimal at 1 mm/s, and the frictional forces. Previously discussed research did not discuss any method of reducing the cogging force of ball-screw drives so that only the friction force is observed.

Lampaert et al. uses information about the cogging force and the inertia of the stage to isolate the friction force in the force determined from the twice differentiated position measurement. This ensures that only the friction force is observed in this test apparatus. Also the long range of travel of the machine tool table allows Lampaert et al. to measure the friction force during velocity tracking motion, even at velocities higher than 1 mm/s.

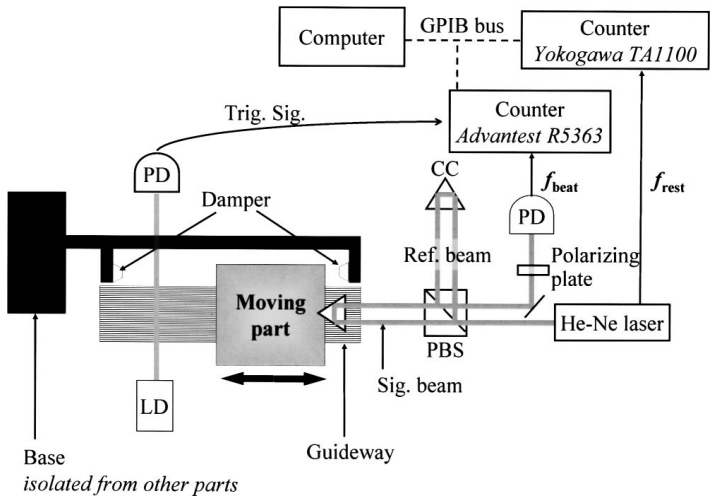

Figure 15: The friction force in a pneumatic linear bearing was determined by Fuji et al. [11] from the position of the moving part, which was measured using interferometry (*Source:* [11]).

Fuji et al. [11] also uses twice differentiated position, measured using interferometry, to determine friction force. The test apparatus is used to measure the friction force in a pneumatic linear bearing, which is actuated by changing the tilt angle of the linear bearing. A mirror is placed on the stage of the pneumatic bearing and the position of the stage is determined from the interference pattern between the incident light of the HeNe laser and the light reflected by the moving mirror. The friction force is then determined from the measured position using regression analysis. Regression analysis assumes that the force acting on the moving part is the sum of the components in proportion to the position, velocity, and tilt angle. These coefficients are then determined using the least-squares method.

The test apparatus of Fuji et al. is probably best used to observe stick-slip motion. However, since the tilt angle is being used to actuate the moving part there will be very

little control over the motion of the moving part. It would be very difficult to use this test setup to measure friction during velocity tracking motion because it would be almost impossible to control the velocity of the moving part using the tilt angle of the guideway.

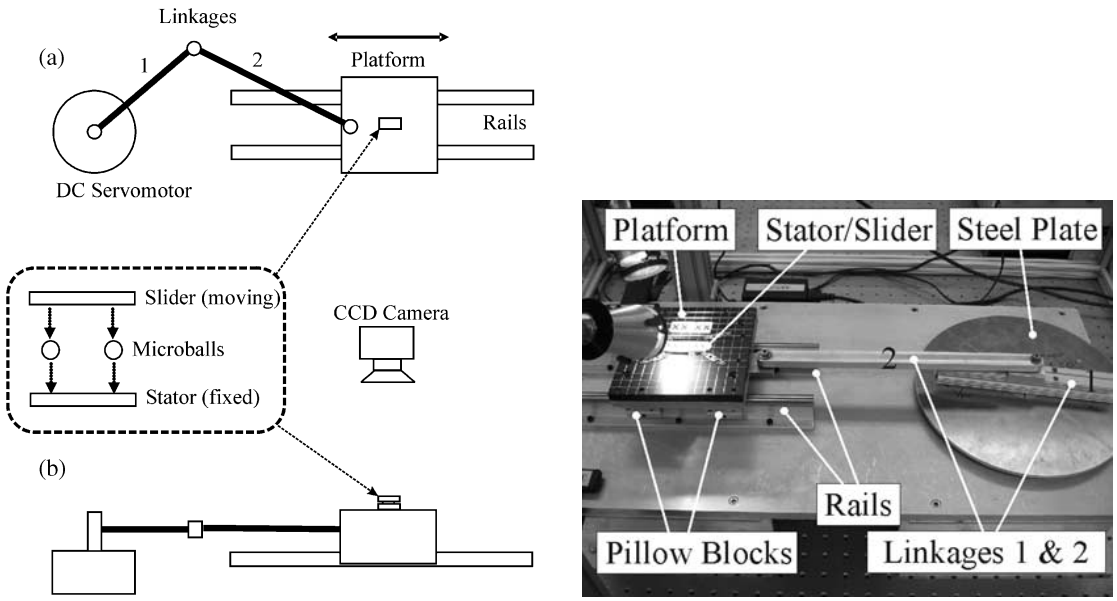

(a) (b)

Figure 16: Lin et al. [22] and Tan et al. [34] determined the friction of linear microball bearings from the relative position between the slider and stator, which was measured using image processing (*Source:* [22]).

The research of Lin et al. [22] and Tan et al. [34] also used twice differentiated position to determine the fiction force. Lin et al. and Tan et al. designed and built an in-situ, non-contact, measurements system to characterize the dynamic friction of linear microball bearings. Microball bearings are place in V-grooves between a stator and slider. The base which the stator is attached to is actuated using a servomotor through a crank-slider, as can be seen in Figure 16. The relative position between the slider and stator is determined by using tracking marks, etched into the stator and the slider, and a vision system. There are several sources of error in this measurement system such as blur, jitter, noise, and lens aberration. Lin et al. and Tan et al. discuss how these measurement errors can be prevented or corrected.

This method is far less dependable, and more complicated, for position measurement than previously discussed methods, such as interferometry. There is no discussion in this paper of how the coupling between test apparatus dynamics and the friction dynamics is minimized, or how they are discerned from one another in the force determined from the measured relative position. It is very likely that the structural, actuator, and inertial dynamics will appear in the determined force, which is believed to be the friction force. Also, like some of the other apparatuses already discussed, because the base of the stator is being actuated there is very little control over the relative displacement between the stator and slider. And because the base of the stator is actuated using a crank-slider this setup is only capable of oscillating motion.

Perhaps the simplest method for determining the friction force in commercial products is to use the current scaling method. Futami et al. [12] use the actuating current in a single axis stage mechanism, shown in Figure 17, that has coarse and fine position control. The stage mechanism is driven by an AC linear motor and guided by a rolling ball guide. Coarse position measurements are taken using an interferometer, while fine position measurements are taken using a capacitive gap sensor. The test apparatus of Futami et a. was used to study force-to-displacement and force-to-velocity relationships. The motor current was scaled to determine the actuator force, and the friction force was determined from the actuator force. Futami et al. were able to classify friction force into three regimes, and through using dynamic models for each regime with the coarse and fine position measurements a resolution better than 1 nm was achieved.

Futami et al. do not mention if they remove the inertial forces from the friction force, which was determined from the actuating current. This means that during some motions where the acceleration is great enough the inertial forces are measured along with the friction force. Also, because capacitive gap sensors often only work over small distances the range of motion of the stage is likely very limited. Therefore, this control method of using fine precision measurements, obtained using a capacitive gap sensor, would not be suitable for velocity tracking motion.

Johnson and Lorenz [18] use the actuator current to determine the friction force present in a robotic gripper. The determined friction force was then used to extract the friction

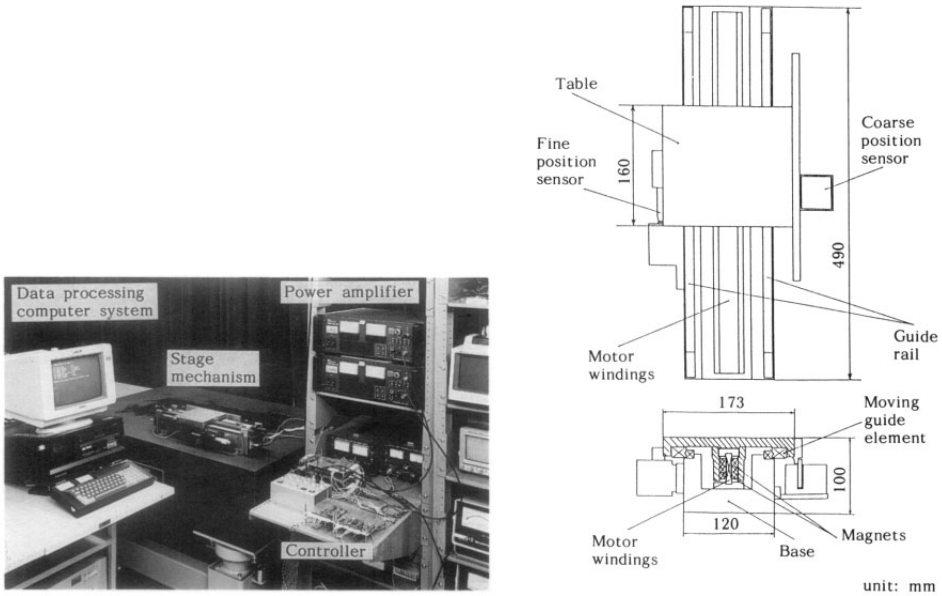

(a) (b)

Figure 17: Illustrated here is the test apparatus of Futami et al. [12]. The experimental set-up of the nanometer positioning system is shown in (a), and the stage mechanism using an AC linear motor and a rolling guide is shown in (b) (*Source:* [12]).

characteristics from the loop errors of a state feedback motion controller. Once the frictional characteristics of the robotic gripper were accurately defined state feedback and a state feedforward compensation methods were implemented to produce a substantial reduction in position and velocity errors.

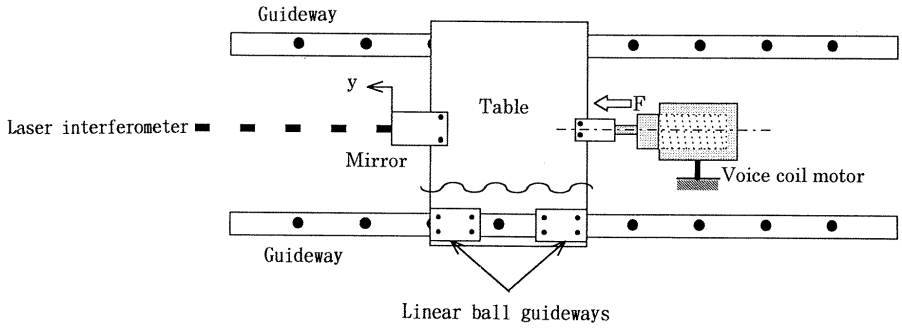

Figure 18: Shown is the first test apparatus used by Otsuka and Masuda [28]. This apparatus measures the friction force in a linear ball guideway by using feedback from the voice coil motor that actuates the table (*Source:* [28]).

Otsuka and Masuda [28] used the actuator current to determine the friction force in three different apparatuses. The first apparatus, which is illustrated in Figure 18, uses the feedback current of the voice coil motor to determine the friction force in a stage that uses linear ball guideways. The position of the stage is measure using interferometry. The voice coil motor does not make a good actuator if a large range of motion is desired though. Because this apparatus is not capable of a large range of motion it may not be suitable for observing friction force during velocity tracking motion.

The second apparatus of Otsuka and Masuda, Figure 19, determines the friction force in a DC servomotor using current feedback. The angular position of the rotor shaft is measured by a rotary encoder inside the DC motor and an eddy current displacement sensor. Using the eddy current displacement sensor to obtain more precise measurements of the angular position of the rotor shaft greatly limits the range of motion of the shaft. Therefore friction force can only be observed over small displacements of the rotor shaft because of the eddy current sensor. This apparatus wold be good for observing stick-slip motion but would not be good for observing friction characteristics that occur during constant angular velocity.

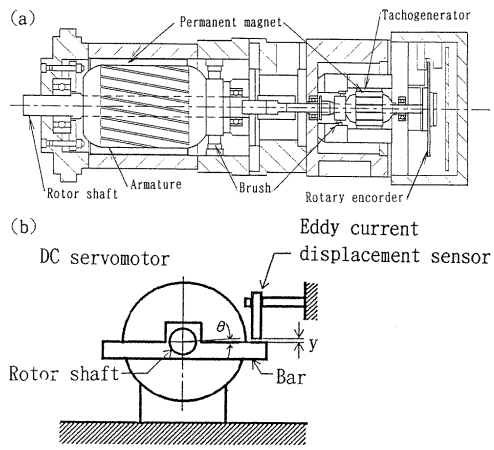

Figure 19: Shown is the second test apparatus used by Otsuka and Masuda [28]. This apparatus measures the friction force in a DC servomotor using feedback from the current applied to the DC motor (*Source:* [28]).

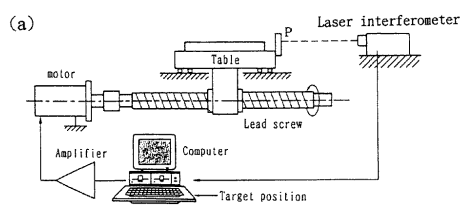

Figure 20: Shown is the third test apparatus used by Otsuka and Masuda [28]. This apparatus measures the friction force of a ball screw and linear ball guideway (*Source:* [28]).

The final apparatus of Otsuka and Masuda, Figure 20, measure the friction force of a ball screw and linear ball guideway from the motor current. An interferometer is used to measure the displacement of the table that sits on the linear ball guideway. This apparatus is similar to the first apparatus of Otsuka and Masuda except because it is driven by a ball screw drive instead of a voice coil motor it is capable of a greater range of motion. This means

that this apparatus could be used to observe friction force characteristics during velocity tracking motion. However, if it is desired that only the friction of the linear ball guideway is measured, and not the friction of the ball screw drive, the cogging force must be identified as was done by Lampaert et al. [21].

The research of Swevers et al. [33] used the current scaling method to determine the friction force present in a joint of a KUKA IR 361 robot arm. The research of Swever et al. focused on the friction force that results due to stick slip motion. The acceleration is small in this regime and the structural dynamics of the robotic arm would be minimal because the displacement is small. Therefore the friction force is the major contributor to the force measured using the current scaling method.

Figure 21: Bucci [4] determined the friction in a crossed-roller linear bearing stage, shown here, using the current scaling method (*Source:* [4]).

The research of Bucci [4] also used the current scaling method to estimate the friction force. Bucci used the motor current scaling method to estimate the friction force in a crossed-roller bearing linear stage. Like the research of Swevers et al. [33] the research of Bucci focused on frictional dynamics that occur due to stick slip motion during point-to-point motion. As previously mentioned, this means that inertial dynamics are negligible. For large point-to-point motions the inertial forces are not negligible. To accommodate for large point-to-point motions Bucci measured the mass of the stage so that friction force may be isolated from the inertial forces.

2.4 CONCLUSION

As previously stated in the abstract the objective of this research is to observe and characterize periodic fluctuations in friction force of ball-element bearings that occur during velocity tracking motion. From the information presented by the research that have been discussed in this section a test apparatus to measure the friction force in ball-element linear bearings will be designed and built. Some of the requirements of my apparatus are as follows.

First the actuating method must be capable of performing velocity tracking motion. This means that it is required that the relative displacement between the ball bearing and the guide rail can be controlled. Some of the previously discussed apparatuses, such as the one presented by Ni and Zhu [25], Harnoy et al. [14], Bucci et al. [5], Fuji et al. [11], and Lin et al. [22], offered very little control over the relative motion between the stator and the slider. Some had little control because they were not directly actuating the relative displacement [5, 14], while others had little control because their method of actuation had limitations as to the movements that could be performed [11, 22, 25].

Some method of actuation that could be used for the apparatus discussed in this research are the methods used by the tribometer of Lampaert et al. [20] and the apparatus for measuring point contact friction force of Harnoy et al. [14]. The apparatus of Lampaert et al. measured line contact friction force by actuating one block, which sits on rollers, while the block that sits on top of the actuated block is held in position by a load cell.

The actuating method which will be used for my apparatus must also not introduce any of its own dynamics that could be measured along with the friction force. Some apparatuses, such as the apparatuses of Godfrey [13], Harnoy et al. [14], and Lin et al. [22], use actuating methods that introduce forces that could appear in their friction force measurements. Other research have used actuating methods that introduce other forces; however, they use methods that compensate for these forces so that they do not appear in their measurement of friction force [21]. The pin-on-disk tribometer of Godfrey measures oscillations in friction force due to non-uniform conditions around the circular wear track on the disk. The apparatus of Lin et al. uses a linkage system to create an oscillating motion, and the linkages may cause periodic increases in force at velocity reversals. The line contact friction measurement apparatus of

Harnoy et al. uses a drive belt system and a ball-screw drive to create the desired motion. The belts can introduce unanticipated dynamics if they are not properly tensioned, and the ball-screw drive has its own friction, which will appear in the force measured by the load cell.

Perhaps a better actuating method that Harnoy et al. [14] could have used is an air bearing stage driven by an AC linear motor. The air bearing has negligible friction, compared to the line contact friction that is being tested, and can be controlled without any physical transmitters, such as the drive belts. The apparatus of Bucci et al. [5] uses an air bearing to actuate the base of a crossed-roller bearing stage. The friction of the air bearing is negligible compared to the friction present in the crossed-roller bearing, which means that the displacement of the crossed-roller stage is primarily due to the friction of the crossed-rollers.

Another important consideration in designing an apparatus to measure friction force is the linkages that are used to hold the components in position. The test apparatus of Dupont et al. [10] uses very stiff linkages to ensure that their deflection is negligible, and therefore can be assumed to be rigid. Sidobre and Heyward [31] use a suspension that provide a nearly perfect cinematic guidance in order to reduce the number of degrees of freedom to exactly two. The kinetic coupling also ensures that the dynamics of the linkages to not cause any undesirable forces to appear in the measurement of the friction force.

Finally the method selected to measure the friction force must be able to measure the friction force during velocity tracking motion. Using method such as twice differentiating position can be useful because they are non-contact methods that do not disturb the motion of the bearing. However, twice differentiating a digital signal can result in a noisy and inaccurate signal [11, 21, 22]. To measure the friction force during velocity tracking motion a method similar to the methods of Lampaert et al. [20] and Harnoy et al. [14] would be best. Both apparatuses hold one of the masses in position using a load cell while the other mass, which is in contact with the stationary mass, is moved at some controlled velocity. For my apparatus the two masses in contact are the ball bearing and the guide rail. The bearing or rail can be held in position by a load cell, while the other moves at a controlled constant velocity. If an air bearing is used to actuate the bearing or guide rail the only force

that will be measured by the load cell will be the friction force between the bearing and rail. The linkage that holds the load cell in position will need to be stiff, similar to the linkages of Dupont et al. [10], so that the deflections of the load cell are minimized.

3.0 TESTBED DEVELOPMENT

As discussed in Chapter 1, it is desired that friction force, velocity error, and the motion of the balls are measured while a rolling element bearing moves at a controlled velocity. To obtain these measurements a testbed was designed and built. This chapter focuses specifically on the design considerations concerning the measurement of the friction force between the rolling element bearing and the guide rail. Other design considerations pertaining to the measurement of the velocity error and the motion of the balls will be discussed in Chapters 4 and 5.

The purpose of this design is to measure the dynamic friction force in rolling element, linear bearings during velocity tracking motion. Thus, it is necessary to move the bearing at a controlled velocity while measuring the forces acting between the ball bearing and the guide rail. For the measurement of the friction force a load cell is used and a controlled linear stage is used to perform the velocity tracking motion. It is also necessary that the design of the testbed allow for the addition of other sensors used to measure the motion of the balls traveling through the race and the relative velocity between the ball bearing and the guide rail.

3.1 LINEAR ROLLING ELEMENT BEARING USED IN TESTING

The linear ball bearings used in this research are radial type, ball-element, linear motion guides from THK (Model SR25W), as shown in Figure 22. This ball bearing is not a caged ball type; that is, the balls are not separated from one another by dividers that keep them consistently spaced. Since the bearing race is not a caged ball type, and because the race

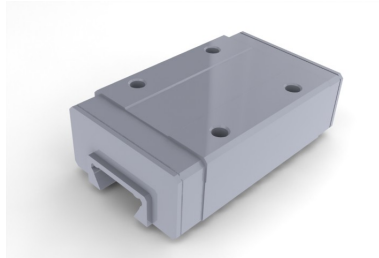

Figure 22: THK SR25W ball bearing to be used in tests.

is not tightly packed, the balls may have some space between them, which could vary from ball to ball. For the SR25W the total space between the balls in the race is 2 mm; that is, a single ball could possibly vary in position by up to ±1 mm.

3.2 TEST SETUP DESIGN AND FABRICATION

In order to allow the bearing to remain stationary, the guide rail is moved instead. This configuration is illustrated in Figure 23. This allows the bearing to be instrumented to measure the forces acting on it and the motion of balls in the bearing. The ball bearing is held in position by a bracket while the guide rail is moved at a controlled velocity by an ABL20100 linear air bearing stage, shown in Figure 24. The friction force between the bearing and rail are measure by a load cell, which is place between the ball bearing and the bracket.

The ABL20100 is an air bearing linear stage that has a 1000 mm range of travel, allowing the ball bearing to travel the full length of the 780 mm guide rail. Use of the entire guide rail allows for longer data records.

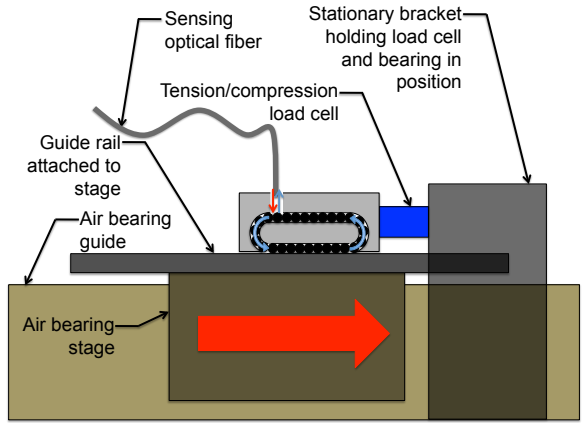

Figure 23: Detailed schematic of proposed test setup design. The guide rail is moved using an air bearing stage while the ball bearing is held in position by a load cell that measures any forces that attempt to put the ball bearing in motion.

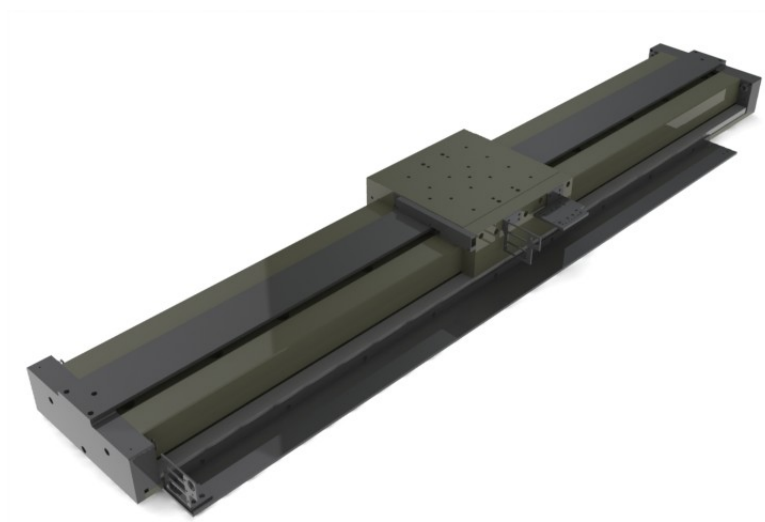

Figure 24: Aerotech ABL20100 air bearing stage that will be used to move the guide rail while the ball bearing is held in position.

(a) Aerotech ABL20100 with aluminum stage and rail guide attached.

(b) Test setup for measuring fluctuations in friction force resulting from balls traveling through the race.

Figure 25: Bearing truck is held in position while guide rail, attached to aluminum stage, is moved underneath it at a constant velocity.

Although the range of the air bearing is enough to use the entire length of the guide rail, the stage of the air bearing is not large enough to support the guide rail. To achieve the desired support length a longer stage was machined out of aluminum, to hold the guide rail in position and keep it parallel to the direction of motion of the air bearing. The aluminum stage is bolted to the stage of the air bearing and the guide rail is then bolted to the aluminum stage. This configuration is illustrated in Figure 25 (a).

The ball bearing is attached to a tension/compression load cell that is attached to a bracket. The bracket is then attached to the table, which for practical purposes, is an inertial frame of reference. The final assembly of the test setup can be seen in Figure 25 (b). The side view of the complete test setup, as seen in Figure 26, shows the bearing attached to the bracket by a load cell that holds the bearing in position while the rail is moved by the air bearing stage. Due to the size of the load cell, a mount is attached to the top of the ball bearing so that the load cell does not make contact with the rail. The extra material can be seen on top of the ball bearing in Figures 25 (b) and 26.

Using the optical encoder in the air bearing the displacement of the guide rail can be measured. If the bearing truck is assumed motionless then the displacement of the rail is

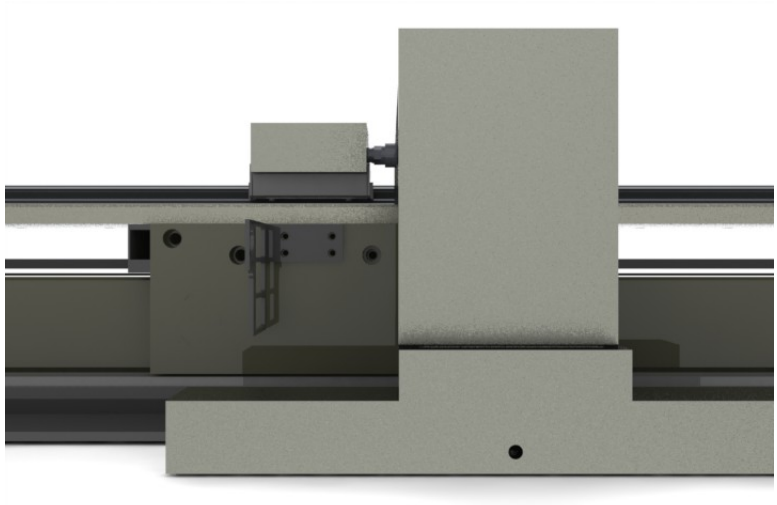

Figure 26: Side view of test setup for measuring fluctuations in friction force resulting from balls traveling through the race.

the relative displacement between the ball bearing and the rail. Should a more accurate approximation of the relative displacement be required, the bearing's displacement can be approximated using Hooke's law, an equivalent stiffness of the bracket and load cell, and the force measurement from the load cell.

The bracket that is used to hold the ball bearing in place with the load cell was fabricated using 1018 steel. A stiff and heavy material was chosen to reduce the deflections of the bracket. This increases the validity of the assumption that the bearing is motionless. Also the bracket was made considerably oversized to reduce the bracket's deflections and increase its weight. The bracket assembly with the load cell attached is illustrated in Figure 27. Feature A shows the load cell and Feature B shows a pair of through holes. The load cell (Feature A) is used to hold the ball bearing in position and measure the friction force. The

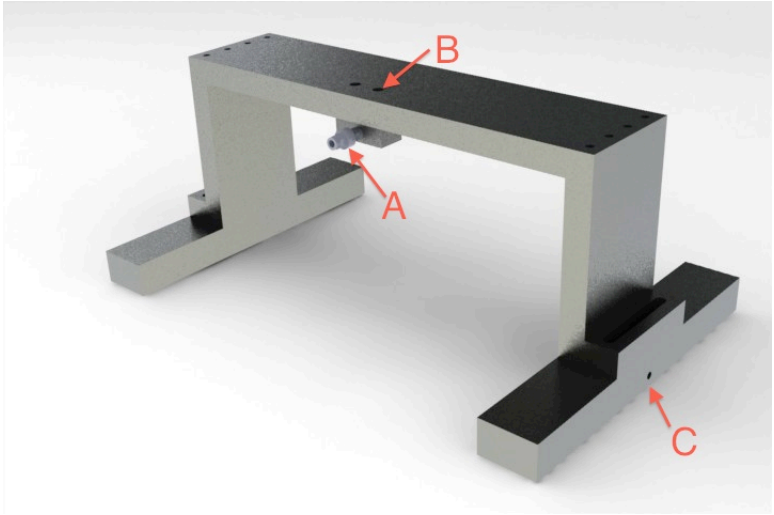

Figure 27: Bracket assembly of test setup. Feature A illustrates the load cell used to hold the ball bearing in position. Feature B shows thru holes that were specifically made oversized to allow for alignment adjustments.

through holes (Feature B) were made oversized for 1/4 inch bolts so that the load cell can be adjusted without having to move the entire bracket assembly to make sure that the axial direction of the load cell is parallel to the direction of motion of the guide rail. The load cell's position can also be adjusted vertically by adding spacers between the bracket's top plate and the block holding the load cell.

3.3 FRICTION MEASUREMENT AND LOAD CELL SELECTION

To measure the friction force a Model 208C01 tension/compression load cell from PCB Piezotronicsis used to hold the ball bearing in position. This sensor was chosen due to its small size, ease of integration into design, measurement range, and speed of response. Some of the load cell's relevant specifications are shown in Table 1.

Table 1: Relevant specifications of PCB load cell model 208C01.

Measurement Range (Compression):	44.48 N
Measurement Range (Tension):	44.48 N
Maximum Static Force (Compression):	266.89 N
Maximum Static Force (Tension):	266.89 N
Low Frequency Response (-5%):	0.01 Hz
Stiffness:	1.05 kN/µm

The dimensions and physical characteristics were the first considerations in selecting an appropriate load cell to measure the friction force. The internal threads on both sides of the sensor made it simple to attach the load cell to the ball bearing and the bracket using studs. The small size of the sensor made it easy to place the bearing close to the rail. This is important because it is best to have the sensor as close to the line of action of the friction force as possible, so that the torque applied to the ball bearing is minimized. It was also important to consider the friction force to ensure it would not exceed the limitations of the load cell. It was estimated that the magnitude of the friction force would be on the order of a few newtons, which is within the tension/compression limits shown in Table 1.

A drawback of using the PCB load cell is that it is a quartz load cell and the DC component of the measurement signal will dissipate over time. The sensor specifications state that the time constant of the dissipating DC charge is $\geq$50 s. Since the most important aspect of the force signal measured is its periodic variation, the PCB quartz load cell is acceptable despite its dissipative nature.

4.0 MEASUREMENT OF POSITION AND VELOCITY

It is known that the relative position between the bearing and the rail can be measure by measuring the absolute position of the air bearing stage. The air bearing uses a Renishaw, linear-incremental, optical encoder (Model RGH22) to measure the motion of the stage. The encoder has a resolution of 0.1 μm. The optical encoder is connected to Aerotech's Soloist controller, which decodes the signal from the encoder and uses the measurement to control the stage's position. Since the guide rail is bolted to the air bearing stage, the position of the stage is also the relative position between the guide rail and the rolling element bearing.

The relative velocity is calculated from the relative position measurement using numerical differentiation. Some methods of numerical differentiation achieve a higher degree of accuracy by incorporating more terms of the Taylor series expansion of the derivative [6]. The centered finite difference formula is used to calculate the velocity from the measurement of position, and is defined as

$$v[n] = \dot{x}[n] = \frac{x[n+1] - x[n-1]}{2T_s}, \tag{4.1}$$

where $x[n]$ is the discrete position, $\dot{x}[n]$ is the discrete derivative of position, $v[n]$ is the discrete velocity, and T_s is the sampling period.

Higher order methods of calculating the discrete derivative of position can be used to improve precision but are not necessary here. This is because the Nyquist frequency is well above the frequencies that we wish to observe. There are also other formulas, such as the forward difference formula, that can be used to calculate the discrete derivative. It was decided that the centered difference formula would be used instead of the forward difference formula because the centered difference formula adds 90° of phase to all frequencies, while the forward difference formula adds more phase at frequencies close to the Nyquist frequency.

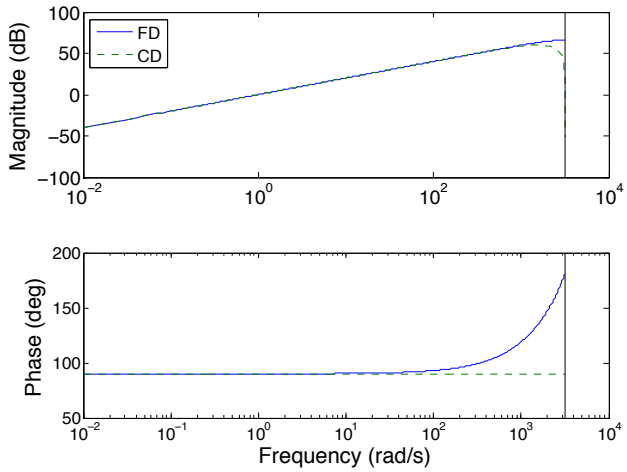

Figure 28: Comparison of Bode plots of the forward-finite divided difference formula and the centered finite-divided difference formula.

The phase of the centered difference formula and the forward difference formula are illustrated in Figure 28, which shows the Bode plots of the two numerical differentiation methods. Understanding how much phase each numerical differentiation method adds is important because when the derivative of position is calculated to get velocity the phase of all of the frequency components will be shifted by the same amount.

To approximate the current precision of the linear stages using rolling bearings some velocity tracking tests were run using the testbed discussed in Chapter 3. Standard deviations of the velocity error were calculated for tracking velocities tests ranging from 1 mm/s to 20 mm/s, incrementing by 1 mm/s. Twenty tests were run at each tracking velocity, and the resulting twenty standard deviations at each tracking velocity were then averaged. As seen in Figure 29, the least precise tracking velocity is 9 mm/s, with a standard deviation of 110 µm/s.

The signal processing techniques that will be used in determining correlation between friction force, velocity error, and the rate of the balls passing a position require that the signals are all sampled synchronously. Although the Soloist is capable of measuring analog inputs synchronously with the signal from the encoder it is only capable of sampling two

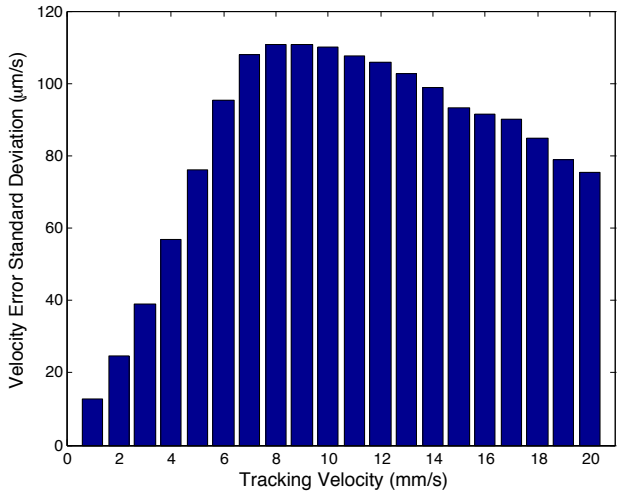

Figure 29: Averaged standard deviations of velocity error for 20 velocity tracking tests per each tracking velocity. The standard deviations appear to reach a maximum for a tracking velocity of 9 mm/s.

analog inputs, which may not be sufficient if more sensors are required. To sample the signals from the load cell, the optical encoder, and the sensor measuring the ball's motion a dSPACE board is used. The dSPACE board is capable of synchronously sampling and recording multiple signals. Also, the dSPACE board has a pin port that is capable of decoding quadrature encoders, such as the optical encoder in the air bearing. dSPACE is used instead of the Soloist analog input channels because it can decode quadrature encoders, allows for more analog inputs, can sample all channels synchronously at adjustable sampling frequencies, and recoding and saving data on dSPACE is very simple.

5.0 DESIGN OF OPTICAL SENSOR FOR DETECTION OF BALLS IN RACE

As discussed in Chapter 1, we can approximate the frequency of the balls as they pass a position in the race. Also, there may be some variance in the frequency resulting from inconsistencies in the spacing between the balls. We can determine the accuracy of the prediction of the frequency and its variance (described in Equation (1.4)) by measuring the balls as they pass a certain position in the race. The motion of the balls is measured using an optical sensor, whose design is discussed in this chapter. The evolution of the optical sensor's design from the initial design to the final design will also be discussed. A redesign was necessary to correct for an instability in the signal from the optical sensor. The source of the instability and how it was corrected is also discussed.

5.1 SENSOR CONCEPT

The purpose of the optical sensor is to detect the motion of the balls as they travel through the race of a linear motion guide. The sensor must also be minimally intrusive to the motion of the balls as they travel through the race. A sensor that interferes with the motion of the balls would most likely cause a periodic disturbance in friction force at the same frequency as the frequency of the predicted disturbance. Since we are attempting to show the existence of this periodic disturbance and show its relation to the motion of the balls in the race, having a sensor that impedes the motion of the balls at the frequency of the periodic disturbance would make the sensor valueless. It was decided that the least intrusive sensor that could be used was an optical sensor that uses an optical fiber with a small diameter, relative to the

diameter of the balls, placed in close proximity to the balls through a small hole machined into the ball bearing. Because the optical fiber does not come into contact with the balls and because the machined hole is small, the sensor will be minimally intrusive to the motion of the balls in the race.

A simple schematic of the sensor can be seen in Figure 30. The light source used in the optical sensor is a 5 mW HeNe laser that is coherent, linearly polarized, and has a wavelength of 633 nm. The incident light from the HeNe laser (red arrows) is focused into a fiber, split by a beam splitting cube, focused into another fiber, and then reflected off the surface of a ball as it passes the tip of the sensing optical fiber. The reflected light (blue arrows) returns back up the sensing fiber, is split by the beam splitting cube, and the portion of the reflected light that is split in the direction of the photodetector is measured. When a ball passes the fiber sensor tip we would expect to see an increase in the voltage of the photodetector, due to an increase in the amount of light reflected back up the sensing optical fiber. The overall efficiency of the sensor is defined as the percentage of power from the source that exits the sensing optical fiber. The components of the design that reduce the overall efficiency the most are the fiber couplers and the beam splitting cube. The beam splitting cube reduces the overall efficiency by 50%; however, without it there would be no way to direct the reflected light toward the photodetector.

5.2 SENSOR DESIGN

The fundamental concept of the sensor is that the light coming out of the tip of a fiber optic cable is reflected off the surface of a ball and back up the fiber, where it is then measured using a photodetector. It would be ideal to use a collimator for the sensor tip to capture the most reflected light. However, some of the smallest collimators are approximately the same size as the balls, which would certainly disrupt the motion of the balls. By keeping the tip of the sensor within a few millimeters of the reflective surface it is possible for the tip of the fiber optic cable to collect enough light without a collimator to obtain a detectable signal.

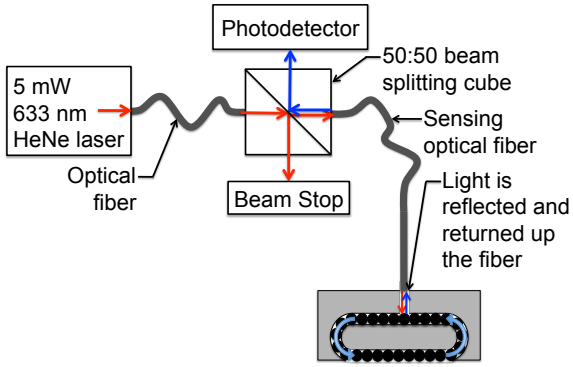

Figure 30: Schematic of optical sensor for the detection of the balls motion within the race of a ball bearing. The red arrows indicate the light from the laser and the blue arrows indicate the light reflected off of the balls as they pass the fiber sensor tip.

The light source that has been selected for the sensor is a HeNe laser, which has a wavelength of 633 nm. This means that the optical elements that have been selected in the design, such as the fibers and photodetector, all contain 633 nm within the range of their operating wavelengths.

The tip of the sensor is a fiber optic cable with a flat cleaved tip and an outer coating diameter of 245 µm, which is 6% the diameter of the balls. The small size of the sensor tip allows for detection of the balls with minimal intrusion to their motion in the race. A small hole is machined through the side of the bearing, using electrical discharge machining (EDM), into one of the loaded races of the bearing. The fiber optic tip is then placed in the hole, where it is held in position by an optical adhesive.

Before placing the fiber into the bearing some initial tests were run by holding the fiber tip in position over top of the balls in one of the open races. A known number of balls were passed under the sensor, and the AC coupled signal from the photodetector was recorded. AC coupling was used because it allowed for the use of greater gains without exceeding the dSPACE input limitations. Eight balls were passed under the sensor tip while the signal from the photodetector was recorded. The results of the initial test of the sensor are seen in Figure 31. In the initial test of the sensor the light leaving the tip of the sensing fiber had

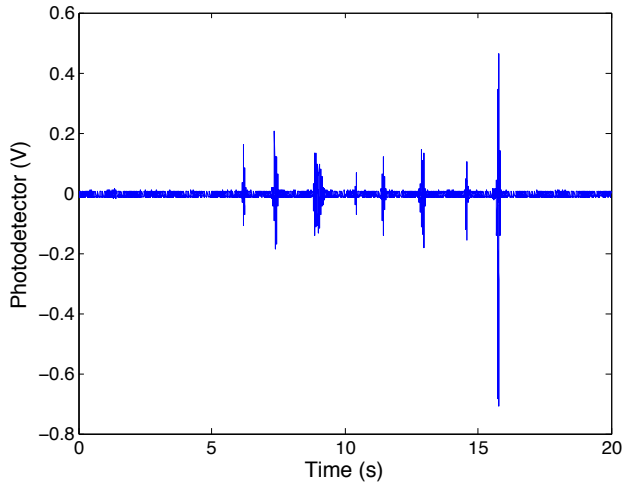

Figure 31: Initial test of the optical sensor. Eight balls were passed under the sensing optical fiber. The eight spikes in the photodetector voltage correspond to the eight balls.

a power of 300 µW, which corresponds to an efficiency of 6%. Spikes in the photodetector voltage, which resulted from reflected light returning up the fiber, were not detectable until a power of 300 µW was obtained. This indicates that for this test setup it is necessary to have a minimum power of approximately 300 µW.

The photodetector signal plot of the initial test contained eight distinct voltage spikes. These eight spikes correspond to the eight balls that pass the sensor tip. It is apparent that some of the spikes seen in Figure 31 are significantly larger than the others. The reason for the varying amplitudes in the peaks was discovered after the sensor tip was placed inside a bearing and the DC signal was recorded. This reason will be explained shortly, after the explanation of the positioning of the fiber tip within the ball bearing.

To place the fiber tip within close proximity of the balls a hole with a diameter of 482 µm is machined through the bearing block to one of the loaded races using EDM. The fiber tip is then placed into the hole, where it is glued into position using an optical adhesive (NOLA81) that is cured using UV light. The optical adhesive is used to hold the fiber tip

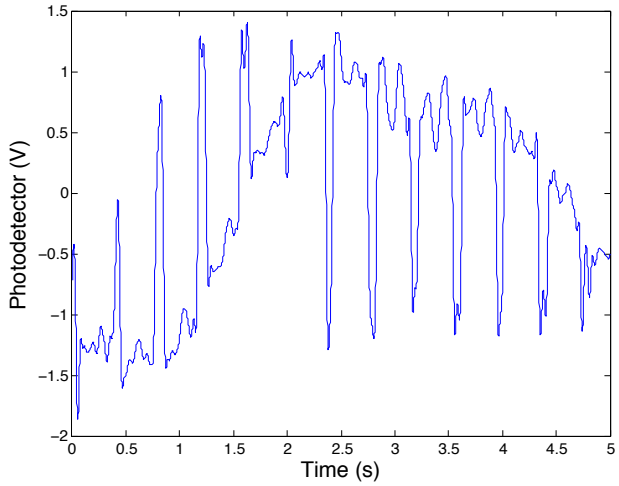

Figure 32: Test of the optical sensor for a tracking velocity of 20 mm/s (corresponds to $f_c = 2.46\,\mathrm{Hz}$).

in close proximity to the balls without affecting the optical properties of the fiber. Because the optical adhesive can affect the light leaving and returning up the fiber it is necessary to make sure that the tip of the fiber is not exposed to the optical adhesive.

Once the fiber was properly placed into the rolling element bearing the air bearing stage performed a tracking velocity motion to determine the performance of the sensor. The acquired signal from the photodetector for a tracking velocity of 20 mm/s can be seen in Figure 32.

Initially only the AC component of the signal was recorded. This was done because the coupling efficiency of the light into the sensing fiber was poor initially, and the DC component at a gain that made the peaks observable was greater than the dSPACE limitations. After improving the coupling of the light into the sensing fiber a lower gain was used, allowing the DC component to be observed as well.

The first observation from Figure 32 is that there are peaks in the signal every 0.406 s. The tracking velocity is 20 mm/s, which corresponds to $f_c = 2.46\,\mathrm{Hz}$. This indicates that a ball should pass the sensor every $1/f_c = 0.406\,\mathrm{s}$. Therefore, as expected, each spike in the photodetector voltage corresponds to a ball passing the sensor.

It was observed from the signal of the optical sensor that the signal had a periodic component with a period of 5 s. Figure 32 shows one period of this periodic component. During the troughs of this low frequency component a ball passing the sensor tip caused peaks upward, while during the crests the peaks are inverted. Finally, it can be observed that when the signal passes through the undistributed level of the sinusoidal component, the amplitude of the peaks are smaller. This explains why during the initial test, seen in Figure 31, the amplitude of some peaks are smaller than others.

The low frequency sinusoidal component of the voltage measured by the photodetector can be removed using AC coupling of the voltage, as was done in the initial test of the optical sensor. However, this does not solve the problem of the varying peak sizes. Also, peaks which occur in the neighborhood of the undistributed level of the low frequency sinusoid could be attenuated to the point where their amplitude is on the order of the signal noise. Essentially making them undetectable.

The individual components of the optical sensor were each tested to determine if they were the cause of the fluctuation in the voltage of the photodetector. It was determined that none of the individual components were the source of the fluctuation. Therefore, it is most likely that some combination of the components in the setup is the cause of the observed fluctuation.

The frequency of the sinusoidal component was observed to increase as strain in the optical fibers increased. From this it was concluded that the combination of the fibers and the HeNe laser were the source of the sinusoidal fluctuation. Single-mode optical fibers affect very few properties of the light source, with the exception of its polarization. For a linearly polarized light source, like the HeNe laser used in the test setup, the direction of the linear polarization may be modified by the optical fiber. This change in the direction of the linear polarization is referred to as polarization degeneracy [17].

Initially, it was believed that the instability in the power was caused by a change in the relative angle between the polarization planes of the incident light and the reflected light as a result of a varying strain applied to the optical fiber. A change in the relative angle between the polarization planes of the incident and reflected light would change how they interfere, thus causing a strain dependent fluctuation in the power. Due to an ideal property of fibers,

called two-pass polarization stability, we can assume that any change in polarization caused by light passing one direction through a fiber will be corrected as the light returns back up the fiber [17]. Although the fiber will not change the polarization of the light, the reflective surface could cause a change in the light's polarization. One may conclude that because of two-pass polarization the power fluctuations are not a result of varying strain in the fiber.

Since it can be concluded that the relative polarization angle is not the cause of the instability, due to two-pass polarization stability, it could be possible that the strain in the fiber is somehow causing a variation in relative phase. This variation in relative phase, between the incident and reflected beams, could vary how the two beams interfere. This varying interference could cause an instability in the power, which is dependent on the strain in the fiber.

5.3 REDESIGN OF OPTICAL SENSOR USING INCOHERENT LIGHT SOURCE

An incoherent light source was used to correct for the interference problems in the sensor. The incoherent source corrects the instability because its interference is a stationary process, meaning there is no change in the time averaged interference between the incident and reflected beams. Since there is no change in how the beams interfere, the signal from the photodetector is stable [17].

The original design of the optical sensor was designed for a red wavelength light source (633 nm). A mounted high power red LED from Thor Labs (Model M625L2) was chosen because its wavelength is compatible with the other components. The red LED has a broader spectrum than the HeNe laser. However, the majority of the LED's power is at a wavelength of 625 nm, which is within the working spectrum of the individual parts of the first setup. The red LED also provides a much higher power at 440 mW, compared to the 5 mW HeNe laser. Coupling an incoherent source into a fiber is often very inefficient, but since the

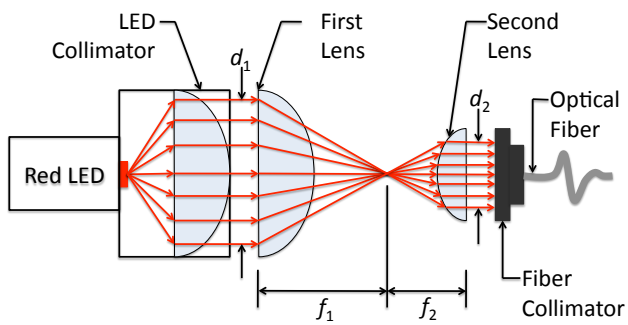

Figure 33: Setup for collimation of incoherent light source into optical fiber. The light from the LED is collimated and then the diameter of the collimated beam is reduced so that more light can enter the fiber collimator. f_1 and f_2 are the focal lengths of the first and second lenses respectively. d_1 and d_2 are the diameters of the first and second collimated beams respectively.

first setup only required a power of approximately 300 µW from the sensing fiber it can be concluded that the setup would be operational with the LED and an overall efficiency of approximately 0.05%.

Incoherent light sources can be very difficult to focus into a fiber because they are difficult to collimate. Although there are collimators designed for LED sources, the beam coming from the collimator is still very divergent in comparison to collimated coherent sources. Assuming that the LED collimator perfectly collimates the source, the ideal setup would be as illustrated in Figure 33.

To focus the collimated LED into an optical fiber it was necessary to reduce the diameter of the beam to approximately the diameter of the fiber port collimator. Assuming that the beam leaving the LED collimator is collimated, the diameter of the beam can be reduced, as illustrated in Figure 33, using two plano-convex lenses. For two lenses the reduced beam diameter can be determined using

$$d_2 = \frac{f_2}{f_1} d_1, \tag{5.1}$$

where d_1 and f_1 are the diameter and focal length of the first lens, respectively, and d_2 and f_2 are the diameter and focal length of the second lens, respectively.

Since we would like to optimize the efficiency of the optical sensor we must focus as much light as possible into the collimator. A ratio of focal lengths should be selected such that d_1 is no more than the diameter of the fiber collimator. This all assumes that the beam coming from the LED collimator is perfectly collimated and not diverging at all, which is known to not be the case. Since the beam from the LED collimator will not be perfectly collimated it is known that there will be some losses in the setup.

Collimating the LED into the smaller core single mode optical fibers, that were previously used in the first test setup, proved to be incredibly inefficient with almost no measurable light leaving the sensing optical fiber. It was decided that it would be necessary to use optical fibers with a much larger diameter. Multimode fibers offer larger core diameters and higher numerical apertures than single mode fibers. A wide range of core diameters are offered for multimode fibers; however, the largest core diameter available was selected to allow us to determine the maximum realizable output using the LED source. The optical fiber selected from Thorlabs has a core diameter of 1 mm and a NA of 0.48 (Model BFH48-1000).

With the new fibers, and using the beam diameter reducer in Figure 33, the efficiency of coupling the LED light source into the optical fibers was greatly improved. With the smaller core single mode fibers the amount of light leaving the tip of the sensing fiber was not visible or measurable. With the larger core diameter fiber a power of 50 µW was easily achievable. This test setup had an efficiency of approximately 0.01%. For the initial setup, discussed in Section 5.2, it was determined that a power of at least 300 µW is necessary to detect a ball as it passes the sensing fiber. It is possible that with the larger core fibers we may not require as much power because it is capable of capturing more light reflected by the balls. To determine if 50 µW is a sufficient amount of power the photodetector output was observed as the sensing fiber was touched to a mirror. As the tip of the sensing fiber came into close proximity, and touched the mirror, there was an increase in the photodetector voltage. Also, there did not appear to be any fluctuations in the voltage measured in the photodetector, or any inverting peaks as the sensing fiber touched the mirror.

After concluding that the reflected light could be detected by the photodetector by simply touching the fiber sensor tip to a mirror it was decided that a new hole would be tapped through the side of a ball bearing into one of the loaded races. The same active race that

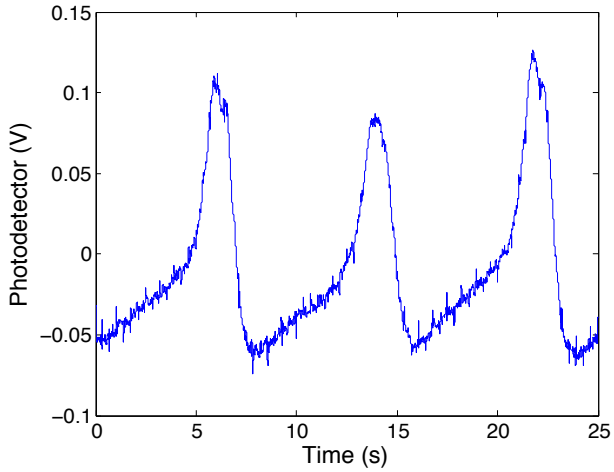

Figure 34: Voltage output of optical sensor using the LED light source for a velocity tracking test at 1 mm/s (corresponds to $f_c = 0.123$ Hz).

was used for the previous test setup was used again for consistency. Since EDM holes would be too small for the 1 mm diameter core of the fiber the hole would be tapped using a 1 mm diameter carbide drill bit. For the first group of tests the optical fiber was not adhered into position using the optical adhesive, in case any adjustments needed to be made. The resulting signal from the photodetector for a velocity tracking test at 1 mm/s can be seen in Figure 34. The signal from the photodetector was AC coupled and the analog signal was low-pass filtered with a cutoff frequency of 400 Hz to prevent aliasing. The AC coupling allowed for the use of higher gains without exceeding the ±10 V limitations of the dSPACE board.

As seen in Figure 34, there are no low-frequency fluctuations in the photodetector voltage or inversions in peaks that were present in the first test setup. The time between the peaks in Figure 34 is approximately 8 s. The balls are passing the sensor tip at approximately a frequency of 0.123 Hz, which is the frequency predicted using Equation (1.2) for a tracking velocity of 1 mm/s. To determine the performance of the sensor at higher velocities a velocity tracking test at 20 mm/s was performed. The resulting signal from the photodetector for a velocity tracking test is shown in Figure 35.

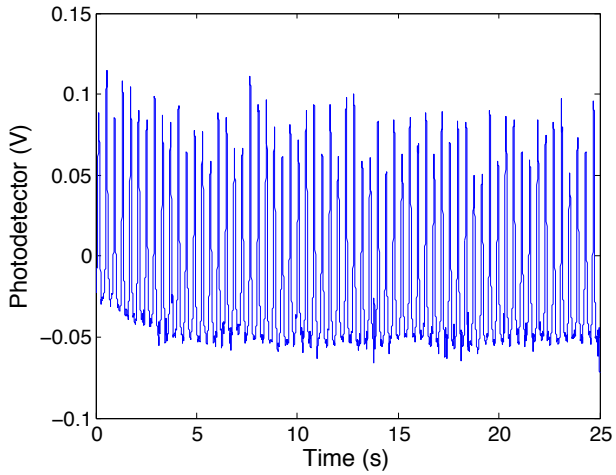

Figure 35: Voltage output of optical sensor using the LED light source for velocity tracking test at 20 mm/s (corresponds to $f_c = 2.46\,\mathrm{Hz}$).

Just like Figure 34, Figure 35 shows no low frequency fluctuation in the signal and no inversions in the peaks that result from balls passing the tip of the sensing fiber. There is also very little variation in the height of the peaks in both Figures 34 and 35. This will make it simpler to calculate the number of balls that pass the sensor tip and the frequency of the balls passing the sensor tip.

To determine if the combination of the HeNe laser and the single mode fiber was in fact the cause of the power instabilities the HeNe laser was used with the larger diameter fibers. The HeNe laser was attached to the new setup and some alignment adjustments were performed. The alignment adjustments resulted in a power of 140 µW exiting the sensing fiber. This is less power than what was previously achieved with the first setup using the HeNe laser. However, since it is three times the operating power achieved when using the LED we should be able to obtain measurements of the reflected light. The result, as seen in Figure 36 for a 1 mm/s velocity tracking test shows no evidence of the instabilities seen in the tests when the single mode fibers were used (See Figure 32). Although the photodetector voltage in Figure 36 does not show any inversions or instability some slight drift in the DC component was observed. This could mean that the same strain dependent power fluctuation

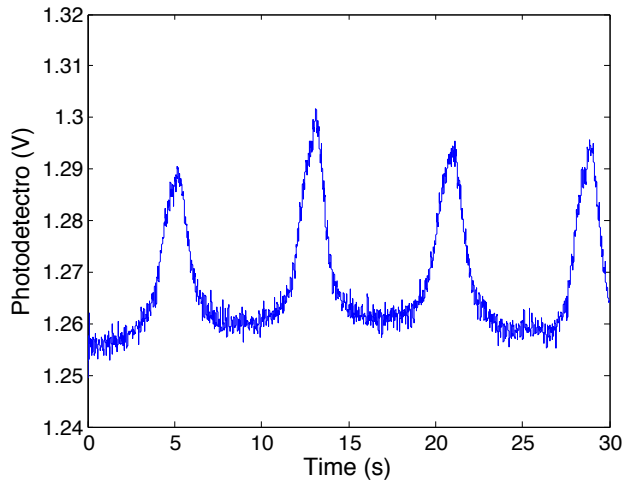

Figure 36: Voltage output of optical sensor using the 1 mm core diameter fibers and the HeNe light source for a velocity tracking test at 1 mm/s (corresponds to $\tau_c = 8.13\,\mathrm{s}$).

previously observed is still occurring. However, since the new fiber is thicker and stiffer it is likely that it is less susceptible to the low frequency oscillations that were causing the low frequency strain variation in the optical fiber. Since some drift in the optical sensor signal was observed when the HeNe was used it was decided that the LED would be used instead, despite the fact that the LED is more challenging to collimate into a fiber.

To increase the power of the light exiting the sensing fiber the Keplerian telescope, used to reduce the diameter of the beam, was exchanged for a Galilean telescope, as illustrated in Figure 37. This allows more light to be captured in the fiber. Using a Galilean telescope in the test setup allows the lenses to be placed closer together because of the negative focal length of the plano-concave lens. More of the light that is still diverging may be captured and potentially collimated into the optical fiber. Equation (5.1) still applies for the Galilean telescope, except that f_2 is now negative, and can be used to determine the diameter of the reduced beam. After changing the beam diameter reducer the power was increased from 50 µW, which was obtained using the Keplerian telescope, to 100 µW. A power of 100 µW for the LED light source corresponds to an efficiency of 0.02%.

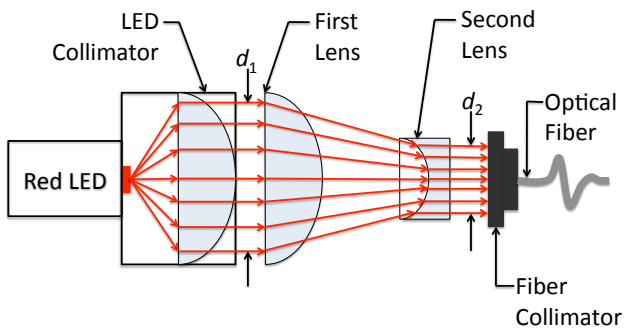

Figure 37: Galilean telescope is used to increase the amount of light captured in the optical fiber. A Galilean telescope uses a plano-concave lens as the second lens, which has a negative focal length. This means the two lenses can be placed closer together, allowing the second lens to capture more of the light.

AC coupling the signal from the photodetector allowed the use of higher gains to make the spikes in voltage, due to a ball passing the sensor, more significant. The AC coupling, which is essentially a high-pass filter with a very low cutoff frequency, will compensate for slow increases in the voltage from the photodetector. The compensation of the AC coupling creates abnormal peaks in the voltage, as illustrated by Figure 38. Since the AC coupling causes irregular peaks it would be best to use the DC coupled signal, even though the peaks are less apparent.

Using the DC coupled signal from the photodetector means that high gains cannot be used because of the dSPACE limitations. This means that the DC coupled signal may have a lower signal-to-noise ratio, and the voltage peaks will be smaller. Although the signal may be noisier and the peaks may be smaller the DC coupling preserves the profile of the peaks that indicate a ball passing the sensor tip, as illustrated in Figure 39. The peaks seen in Figure 39 do not experience an abnormal drop in voltage, like the peaks in Figure 38, because there is no component which compensates for slow increases in voltage.

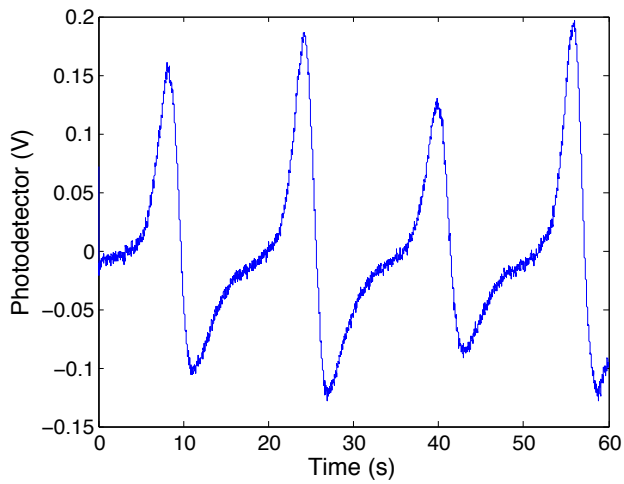

Figure 38: AC coupled signal from photodetector for a velocity tracking test at 0.5 mm/s (corresponds to $\tau_c = 16.22\,\mathrm{s}$). The increase in voltage due to a ball reflecting light occurs at such a low frequency that the AC coupling compensates for the slow increase in voltage.

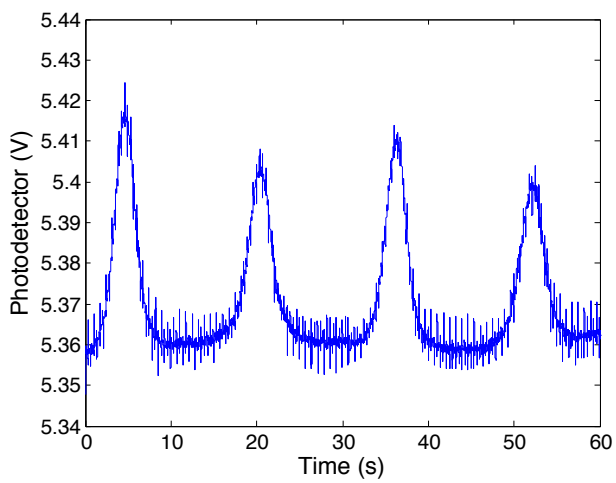

Figure 39: DC coupled signal from photodetector for a velocity tracking test at 0.5 mm/s (corresponds to $\tau_c = 16.22\,\mathrm{s}$). The DC coupled signal cannot use high gains to make signal clearer but can preserve the profile of the peaks that indicate a ball passing the sensor.

6.0 SYSTEM AND MODEL SIGNALS ANALYSIS

This chapter focuses on a qualitative analysis of the system and the signals from the sensors. The system being studied is modeled using a block diagram determined from the dynamics of the system. The analysis of the signals is done using functions that have characteristics that are believed to be present in the actual signals, which are recorded during a velocity tracking test. The most important characteristic of the signals from the load cell, optical encoder, and the optical sensor is their frequency content. The model signal functions are processed using techniques, such as correlation and power spectral density calculations, that will be used on the actual measurement signals for a velocity tracking test. This should give insight into what should be expected from the results of the signal processing.

6.1 SYSTEM ANALYSIS

A simple block diagram of the system that is being studied is illustrated in Figure 40, and a description of the variables used can be seen in Table 6.1. First, although the friction force, f_f, is shown as an independent input to the system (see Figure 40), it is important to note that the friction force has a dependence on velocity and position. Some of the friction models described by Olsson et al. [26] describe this dependence. The dependence of friction on velocity and position described in each of the models are based on experimental observations. For our analysis of the system in Figure 40 we will prescribe a function for the friction force that is an explicit function of velocity. The function of friction force will not be

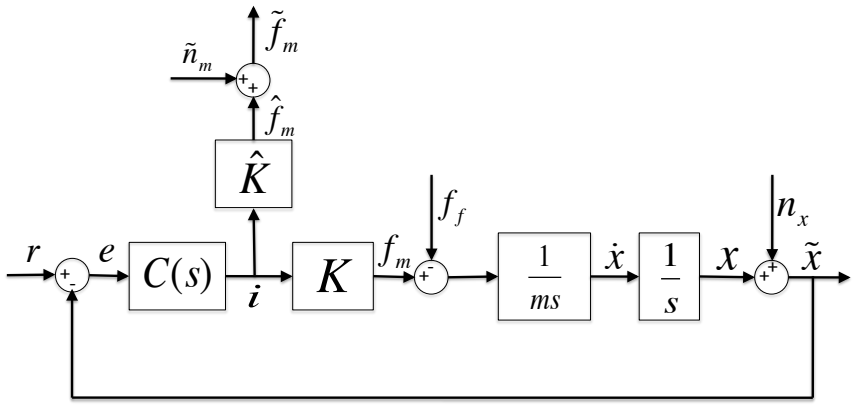

Figure 40: Simple block diagram of the system being studied.

Table 2: Variables used in block diagram and analysis of the system.

r	The position reference signal
x	The position of the air bearing stage
n_x	The noise introduced into the position signal before it is measured
$\tilde{x}$	The measured position of the air bearing stage with measurement noise
$\dot{x}$	The velocity of the air bearing stage
e	The error between the position reference and the actual position
$C(s)$	The controller of the air bearing stage
i	The motor command current
K	The back EMF constant
f_m	The force generated by the linear motor
$\hat{K}$	The estimated back EMF constant
$\hat{f}_m$	The estimated force generated by the linear motor
$\tilde{n}_m$	The noise introduced into the estimated friction force before it is measured
$\tilde{f}_m$	The measured force generated by the linear motor that includes measurement noise
f_f	The friction force between the guide rail and the ball bearing
m	The mass of the object in motion

given as a function of position because friction's dependence on position is only significant in the sticking regime, which is the regime in which static friction has not been exceeded [26]. Since during velocity tracking the balls are not in the sticking regime we can consider friction's dependence on position negligible.

As can be seen in Figure 40 the system is a multi-input multi-output (MIMO) system. The system has two inputs, the reference signal and the friction force, and two outputs, the measured motor force and the measured position of the air bearing stage. To qualitatively evaluate the system we will need to determine the transfer functions from each input to each output. The transfer functions will give us an idea of how the system will react for a given input.

For simplification we will assume that the controller used by the linear air bearing stage, $C(s)$, is a proportional-derivative controller described by

$$C(s) = K_D s + K_P, \tag{6.1}$$

where K_D is the the derivative gain and K_P is the proportional gain. A PD controller was chosen because it simplifies the analysis of the system, while allowing for control of the systems natural frequency and damping. Also, the derivative control is necessary so that the system is stable for a position command. From Figure 40 and Equation (6.1) we can conclude that the loop gain of the system, $L(s)$, can be described by

$$L(s) = \frac{K(K_P + K_D s)}{ms^2}. \tag{6.2}$$

Knowing the loop gain will help to evaluate the transfer functions that relate an input to an output.

The transfer function from the reference signal, $r(t)$, to the position of the stage, $x(t)$, is

$$\frac{X(s)}{R(s)} = G_{xr}(s) = \frac{K(K_P + K_D s)}{ms^2 + KK_D s + KK_P}. \tag{6.3}$$

Since we will be observing the system for velocity tracking motion we know that the reference will be $r(t) = Vt$, where V is the tracking velocity and the Laplace transform of $r(t)$ is $R(s) = V/s^2$. The transfer function given by Equation (6.3) is a type 0 system because it contains zero poles at the origin. The transfer function has two poles and one zero, which

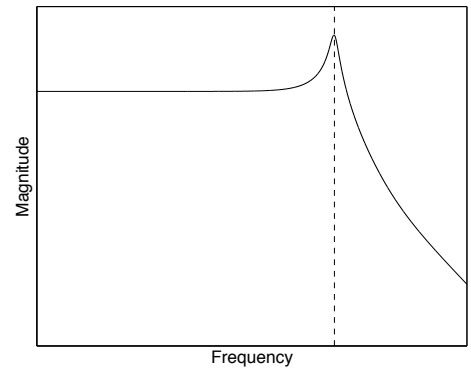

Figure 41: Plot of magnitude versus frequency for the transfer function $G_{xr}(s)$. The vertical dashed line illustrates the natural frequency of the system, where the resonant peak occurs, and the slope of the magnitude at high frequencies will be $-20\,\mathrm{dB}$ per decade

means that the slope of the magnitude at high frequencies will be $-20\,\mathrm{dB}$ per decade. The magnitude of this system will have a frequency response like the one illustrated by Figure 41. The vertical dashed line illustrates the natural frequency of the system that will occur at $\omega_n = \sqrt{\frac{KK_P}{m}}$, as can be determined from Equation (6.3). The qualitative plot of the system $G_{xr}(s)$ is shown to be underdamped in Figure 41. This was done simply to illustrate the presence of a resonance peak. Since it is not favorable for a linear stage to have a large resonance peak it is likely that the peak will not be as pronounced as it is in Figure 41.

It is also important to note that the zero of $G_{xr}(s)$ can affect the slope of the magnitude at low frequencies. If the zero of $G_{xr}(s)$ occurs at a frequency below the natural frequency then the slope of the magnitude at low frequencies will be $20\,\mathrm{dB}$ per decade, instead of zero as shown in Figure 41.

If we were to consider the steady state of the velocity of the system, $\dot{x}(t)$, we would simply have to take the derivative of the position. In the Laplace domain this means that we would simply multiply $X(s)$ by the Laplace variable s. The steady state velocity, for a tracking velocity reference $R(s) = V/s^2$, can be solved for using the final value theorem

$$\lim_{t\to\infty} \dot{x}(t) = \dot{x}_{ss} = \lim_{s\to 0} s^2 G_{xr}(s)R(s) = \lim_{s\to 0} s^2 \frac{K(K_P + K_D s)}{ms^2 + KK_D s + KK_P}\frac{V}{s^2} = V. \tag{6.4}$$

As expected, the velocity converges to the tracking velocity, V. This means that after the transients within the system decay the velocity of the stage will settle to the desired tracking velocity.

The relation between the position and the reference signal is important however it is also important to discuss how the position and velocity react to the friction force. The transfer function from the friction force input, $f_f(t)$, to the position output, $x(t)$, can be expressed as

$$\frac{X(s)}{F_f(s)} = G_{xf}(s) = \frac{1}{ms^2 + KK_D s + KK_P}. \tag{6.5}$$

For objects moving at a constant velocity, the friction force is described as being constant by many different friction models. However, it is believed that the balls traveling through the race cause periodic fluctuations in the friction force during velocity tracking motion that act like a periodic disturbance to the velocity. To consider how a friction force with some periodic content may affect the position we must consider what the magnitude of the frequency response of the system described by Equation (6.5) may look like. The transfer function in Equation (6.5) has two poles, like the transfer function $G_{xr}(s)$, but it does not have any zeros. This means that the magnitude at high frequencies will have a slope of $-40\,\mathrm{dB}$ per decade. The plot of the magnitude of $G_{xf}(s)$ will qualitatively have the same shape as the plot of the magnitude of $G_{xr}(s)$, except at high frequencies where the slope of the magnitude will be $-40\,\mathrm{dB}$ per decade.

The resonant peak in Figure 41 means that if there is periodic content in the friction force, and it were to have a frequency at approximately the natural frequency of the system, the disturbance from the friction force would be amplified. It was believed that the fluctuations in friction force caused serious errors at low velocities as a result of the Stribeck effect, which is an increase in friction force as velocity decreases [1]. However, if the damping of the resonance peak is small, and if the frequency of the fluctuations in friction force is approximately the resonant frequency, then the magnitude of the tracking error could be amplified more than it would be by the Stribeck effect. Since the periodic fluctuations in the friction force has a frequency that is dependent on the tracking velocity, as expressed in Equation (1.2), some higher tracking velocities may also cause poor tracking due to the resonant frequency. The natural frequency of the system is determined by the controller

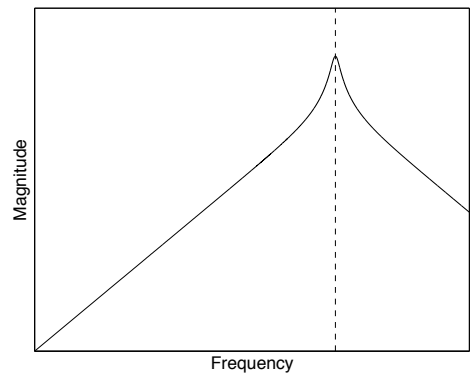

Figure 42: Plot of magnitude versus frequency for the transfer function $G_{vf}(s)$. The vertical dashed line illustrates the natural frequency of the system.

parameter selected. To achieve a favorable response a high natural frequency is often desired, which would give the system a good bandwidth. This means that the disturbance caused by the balls, which occurs at low frequencies, will not be amplified by the natural frequency of the system, which will occur at a much higher frequency.

From the block diagram of the system, the transfer function from friction force to velocity is

$$\frac{V(s)}{F_f(s)} = G_{vf}(s) = \frac{sX(s)}{F_f(s)} = \frac{s}{ms^2 + KK_D s + KK_P}. \tag{6.6}$$

This transfer function is similar to the transfer function from friction force to position except it has a zero at the origin. The magnitude response of $G_{vf}(s)$ will have the same natural frequency as $G_{xf}(s)$. The zero at the origin will cause the magnitude response of the transfer function to have a slope of 20 dB per decade at low frequencies. Similar to the transfer function $G_{xr}(s)$, the magnitude of $G_{xf}(s)$ at high frequencies will have a slope of -20 dB per decade. A qualitative plot of the magnitude response of Equation (6.6) is illustrated in Figure 42.

Shown in Figure 6.6, the plot of the magnitude response of $G_{vf}(s)$ shows that for periodic content of the friction force, with a frequency less than the natural frequency, as frequency increases so will the magnitude of the velocity. Since it is believed that the frequency of the periodic disturbance found in velocity is proportional to the tracking velocity, as the

tracking velocity increases the magnitude of the periodic velocity error should increase as well. This could explain why there is an increase in the standard deviation of the velocity error as tracking velocity increases as previously shown (see Chapter 4, Figure 29).

6.2 MODEL SIGNALS AND ANALYSIS

Functions were selected that model the expected characteristics of the signals, to give an illustration of what to expect from the signal processing that will be done for the actual signals. The most important characteristic of the three signals will be their periodic content, which will have a frequency of f_c. The continuous time signal processing techniques used in this section are referenced from Bendat and Piersol [2].

The function that describes the friction force is

$$F_f(t) = F_c + a_f \sin(2\pi f_c t), \tag{6.7}$$

where F_c is the Coulomb friction, which is constant for a constant velocity, and a_f is the amplitude of the sinusoid. Since the actual tests will be done for a constant velocity F_c in Equation (6.7) will be constant. The sinusoidal component of the friction force will represent the periodic fluctuation in friction force, which is believed to be caused by the motion of the balls.

Since force is proportional to acceleration, and acceleration is the derivative of velocity, the periodic content of the velocity error will be described using a function that is 90° out of phase relative to the friction force. This will allow us to observe how some phase difference may affect the signal processing.

The function that describes the velocity error is

$$v_e(t) = a_v \cos(2\pi f_c t). \tag{6.8}$$

The velocity error, $v_e(t)$, does not contain a DC component because it is believed that the mean of the velocity error will be small, and can be assumed to be zero. The amplitude of the sinusoid of $v_e(t)$ is a_v. The cosine function was used instead of the sine function, which

was used to describe the expected periodic content in the friction force, because the relative phase difference between velocity and friction force is expected to be 90°.

Finally the signal from the optical sensor is described as

$$s(t) = S + a_s \sin(2\pi f_c t), \tag{6.9}$$

where S is the DC component captured by the photodetector, which results from the percent of the incident beam that is reflected in the direction of the photodetector, and a_s is the amplitude of the sinusoidal component.

To show how these signals are correlated with themselves in time the autocorrelations are calculated. The definition for the continuous time autocorrelation of a signal, $x(t)$, is

$$R_{xx}(\tau) = \lim_{T\to\infty} \frac{1}{T} \int_0^T x(t)x(t+\tau)dt. \tag{6.10}$$

The autocorrelation shows how a signal is related to itself by comparing the signal with a time shifted version of itself. Since for autocorrelations a signal is being compared with itself we would expect the maximum correlation to occur at $\tau = 0$, where the shifted version has not been shifted and is exactly identical to the stationary signal.

The autocorrelations of the signals $F_f(t)$, $v_e(t)$, and $s(t)$ were calculated using the definition of the autocorrelation expressed in Equation (6.10). The resulting autocorrelations of the three signals are

$$\begin{aligned}
R_{F_f F_f}(\tau) &= \lim_{T\to\infty} \frac{1}{T} \int_0^T F_f(t)F_f(t+\tau)dt = F_c^2 + \frac{a_f^2}{2}\cos(2\pi f_c \tau) \\
R_{v_e v_e}(\tau) &= \lim_{T\to\infty} \frac{1}{T} \int_0^T v_e(t)v_e(t+\tau)dt = \frac{a_v^2}{2}\cos(2\pi f_c \tau) \\
R_{ss}(\tau) &= \lim_{T\to\infty} \frac{1}{T} \int_0^T s(t)s(t+\tau)dt = S^2 + \frac{a_s^2}{2}\cos(2\pi f_c \tau).
\end{aligned} \tag{6.11}$$

All three of the autocorrelations are periodic in τ with a period of τ_c, which is the inverse of f_c. Qualitative plots of the autocorrelations calculated from the model signals are illustrated in Figure 43. A signal is correlated with itself for correlation times, τ, where the autocorrelation is at a local maximum. The plots in Figure 43 show increases in correlation for correlation times that are positive and negative integer multiples of τ_c, which are illustrated with vertical red-dashed lines.

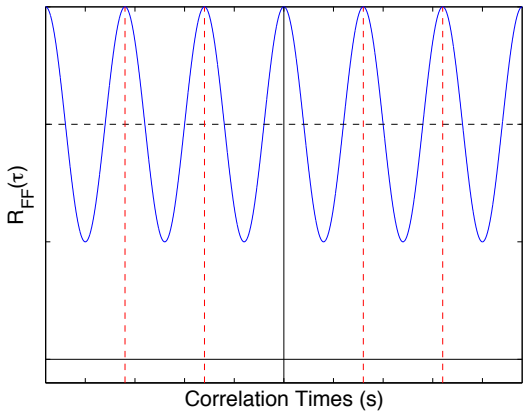

(a) Autocorrelation of model of friction force.

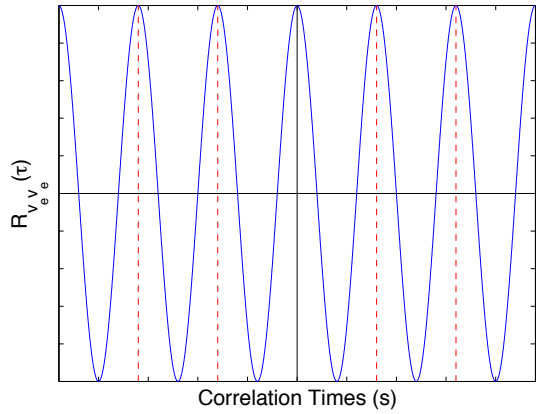

(b) Autocorrelation of model of velocity error.

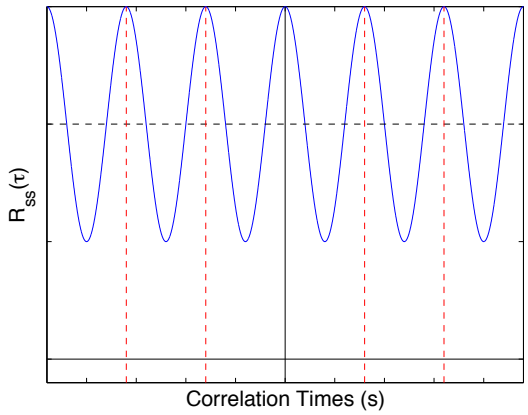

(c) Autocorrelation of model of the optical sensor signal.

Figure 43: Qualitative plots of autocorrelations of model signals.

The amplitude of the periodic components in the autocorrelations are dependent on the amplitudes of the sinusoidal components of the signals. If the amplitudes of the frequency content of the signals are small then the amplitudes of the frequency content of their autocorrelation will also be small. The autocorrelations of sine and cosine functions both result in a cosine component in the autocorrelation. This is because at $\tau = 0$ each signal is perfectly correlated with itself. Because the signals are continuous and are non-convergent as t approaches $\pm\infty$, their autocorrelations are continuous and non-convergent. The correlation times where the signals are the least correlated, or negatively correlated if there is no DC component, occurs for values of τ where each signal is 180° out of phase with itself. In the plots shown in Figure 43 this occurs at positive and negative odd integer multiples of $\tau_c/2$.

To determine how one signal is correlated with another signal in time the cross-correlation can be used. The cross-correlation of two signals, $x(t)$ and $y(t)$, is defined as

$$R_{xy}(\tau) = \lim_{T\to\infty} \frac{1}{T} \int_0^T x(t)y(t+\tau)dt. \tag{6.12}$$

The cross-correlation between two signals can be used to determine how two signals are periodically related, and if there is any phase between the two signals. Periodic content that is shared by two signals will show up in their cross-correlation as periodic content of the same frequency.

There may not be a peak in the cross-correlation at $\tau = 0$, due to some phase difference between the shared periodic content. The distance from $\tau = 0$ to the nearest peak in the cross-correlation can be used to determine the phase difference between the two signals through the relationship $\phi = 360°\tau_\phi/\tau_c$, where τ_ϕ is the correlation time of the peak closest to $\tau = 0$.

It is important to note that the cross-correlation of $x(t)$ with $y(t)$ is equal to the cross-correlation of $y(t)$ with $x(t)$, mirrored about $\tau = 0$. This property can be summarized as $R_{xy}(\tau) = R_{yx}(-\tau)$, and is important because it tells us that it is unnecessary to calculate half of the cross-correlations.

The cross-correlations between $F_f(t)$, $v_e(t)$, and $s(t)$ were calculated using Equation (6.12). The calculated cross-correlations of the three signals are

$$\begin{aligned}
R_{F_f v_e}(\tau) &= \lim_{T\to\infty} \frac{1}{T}\int_0^T F_f(t)v_e(t+\tau)dt = -\frac{a_f a_v}{2}\sin(2\pi f_c \tau) \\
R_{F_f s}(\tau) &= \lim_{T\to\infty} \frac{1}{T}\int_0^T v_e(t)s(t+\tau)dt = F_c S + \frac{a_f a_s}{2}\cos(2\pi f_c \tau) \\
R_{s v_e}(\tau) &= \lim_{T\to\infty} \frac{1}{T}\int_0^T s(t)v_e(t+\tau)dt = -\frac{a_v a_s}{2}\sin(2\pi f_c \tau).
\end{aligned} \tag{6.13}$$

The calculated cross-correlations are all periodic with a period of τ_c, as would be expected since the cross-correlation of two functions is periodic with a frequency equal to the frequency shared by the two signals. A qualitative plot of the cross-correlations can be seen in Figure 44. The cross-correlations $R_{F_f v_e}(\tau)$ and $R_{s v_e}(\tau)$ are not correlated at $\tau = 0$. This is because $v_e(t)$ is 90° out of phase with $F_f(t)$ and $s(t)$. For $R_{F_f v_e}(\tau)$ and $R_{s v_e}(\tau)$ $\tau_\phi = -\tau_c/4$, which means that $\phi = -90°$. This means that periodic component of $v_e(t)$ is $-90°$ out of phase with respect to $F_f(t)$ and $s(t)$. Similar to the autocorrelations, the amplitude of the periodic components of the cross-correlations depends on the amplitude of the frequency content which is shared between the two signals. This means that if the shared frequency components have small amplitudes then the periodic component in the cross-correlation will also have a small amplitude, which may be difficult to discern in a plot.

The only cross-correlation function that has a DC component is $R_{F_f s}(\tau)$. This is because $F_f(t)$ and $s(t)$ are the only two signals which share a DC component. This can be thought of as the two signals sharing frequency content at 0 Hz.

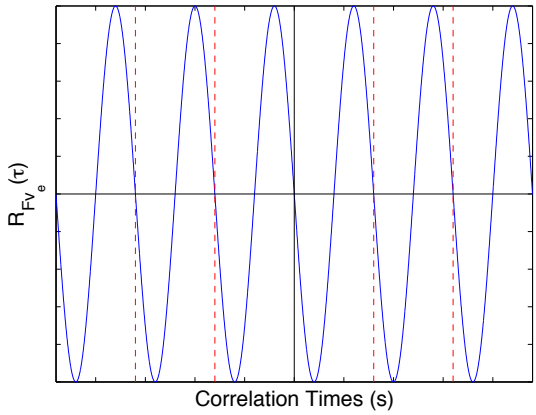

(a) Cross-correlation between model signals of friction force and velocity error.

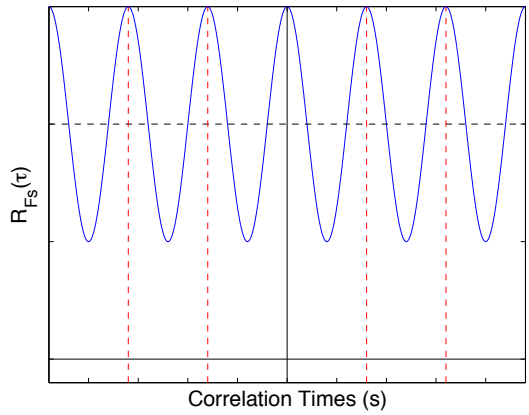

(b) Cross-correlation between model signals of friction force and optical sensor.

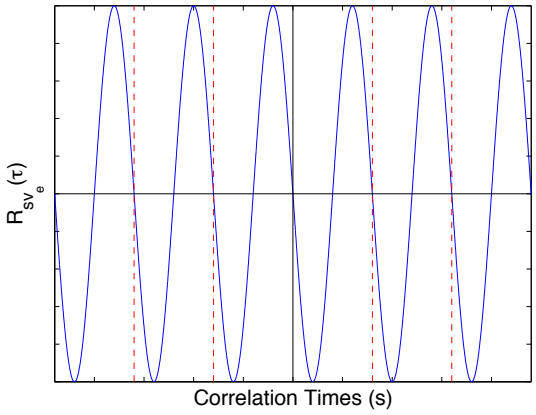

(c) Cross-correlation between model signals of optical sensor and velocity error.

Figure 44: Qualitative plots of cross-correlations of model signals.

To determine the frequency content of a signal the auto-spectral density is used. For a signal $x(t)$ the auto-spectral density, or auto-spectrum, is defined as the Fourier transform of the autocorrelation $R_{xx}(\tau)$ which is expressed as

$$S_{xx}(\omega) = \mathcal{F}[R_{xx}(\tau)] = \frac{1}{\sqrt{2\pi}} \int_{-\infty}^{\infty} R_{xx}(\tau) e^{-j\omega t} d\tau, \tag{6.14}$$

where j is the imaginary number and ω is angular frequency with units of radians per unit time.

The auto-spectra of the three model signals were calculated to be

$$\begin{aligned}
S_{F_f F_f}(\omega) &= \mathcal{F}[R_{F_f F_f}(\tau)] = F_c^2 \sqrt{2\pi}\delta(\omega) + \tfrac{a_f^2}{2}\sqrt{\tfrac{\pi}{2}}\delta(\omega - 2\pi f_c) + \tfrac{a_f^2}{2}\sqrt{\tfrac{\pi}{2}}\delta(\omega + 2\pi f_c) \\
S_{v_e v_e}(\omega) &= \mathcal{F}[R_{v_e v_e}(\tau)] = \tfrac{a_v^2}{2}\sqrt{\tfrac{\pi}{2}}\delta(\omega - 2\pi f_c) + \tfrac{a_v^2}{2}\sqrt{\tfrac{\pi}{2}}\delta(\omega + 2\pi f_c) \\
S_{ss}(\omega) &= \mathcal{F}[R_{ss}(\tau)] = S^2 \sqrt{2\pi}\delta(\omega) + \tfrac{a_s^2}{2}\sqrt{\tfrac{\pi}{2}}\delta(\omega - 2\pi f_c) + \tfrac{a_s^2}{2}\sqrt{\tfrac{\pi}{2}}\delta(\omega + 2\pi f_c).
\end{aligned} \tag{6.15}$$

where $\delta(\omega)$ is the Dirac delta function that is infinite for $\omega = 0$, and zero elsewhere. All of the calculated auto-spectra have Dirac delta functions that are infinite at $\pm 2\pi f_c$. This means that there is some periodic content in each of the signals with an angular frequency of $2\pi f_c$. The auto-spectral densities of $F_f(t)$ and $s(t)$ also have Dirac delta functions that are infinite at $\omega = 0$. This is because both of those signals contain periodic content at $\omega = 0$. Qualitative plots of the auto-spectral densities are shown in Figure 45.

To determine the frequency of the periodic content that is shared between the three signals their cross-spectral densities are calculated. Similar to the auto-spectral density, the cross-spectral density is calculated by taking the Fourier transform of the cross-correlation. The cross-spectral density of two signals $x(t)$ and $y(t)$, whose cross-correlation is $R_{xy}(\tau)$, is calculated as

$$S_{xy}(\omega) = \mathcal{F}[R_{xy}(\tau)] = \frac{1}{\sqrt{2\pi}} \int_{-\infty}^{\infty} R_{xy}(\tau) e^{-j\omega t} d\tau. \tag{6.16}$$

The cross-spectral densities of the three model signals were calculated using Equation (6.16) to be

$$\begin{aligned}
S_{F_f v_e}(\omega) &= \mathcal{F}[R_{F_f v_e}(\tau)] = -\tfrac{a_f a_v j}{2}\sqrt{\tfrac{\pi}{2}}\delta(\omega - 2\pi f_c) + \tfrac{a_f a_v j}{2}\sqrt{\tfrac{\pi}{2}}\delta(\omega + 2\pi f_c) \\
S_{F_f s}(\omega) &= \mathcal{F}[R_{F_f s}(\tau)] = F_c S \sqrt{2\pi}\delta(\omega) + \tfrac{a_f a_s}{2}\sqrt{\tfrac{\pi}{2}}\delta(\omega - 2\pi f_c) + \tfrac{a_f a_s}{2}\sqrt{\tfrac{\pi}{2}}\delta(\omega + 2\pi f_c) \\
S_{s v_e}(\omega) &= \mathcal{F}[R_{s v_e}(\tau)] = -\tfrac{a_v a_s j}{2}\sqrt{\tfrac{\pi}{2}}\delta(\omega - 2\pi f_c) + \tfrac{a_v a_s j}{2}\sqrt{\tfrac{\pi}{2}}\delta(\omega + 2\pi f_c).
\end{aligned} \tag{6.17}$$

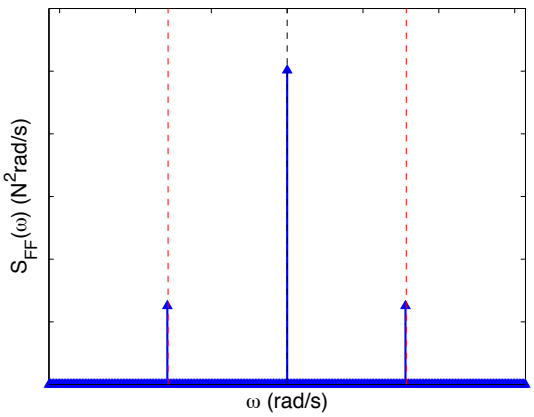

(a) Auto-spectral density of model signal of friction force.

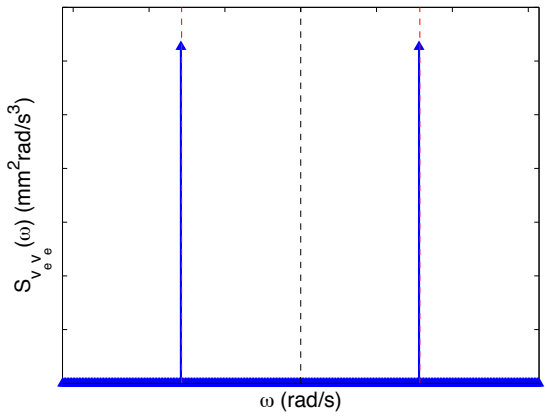

(b) Auto-spectral density of model signal of velocity error.

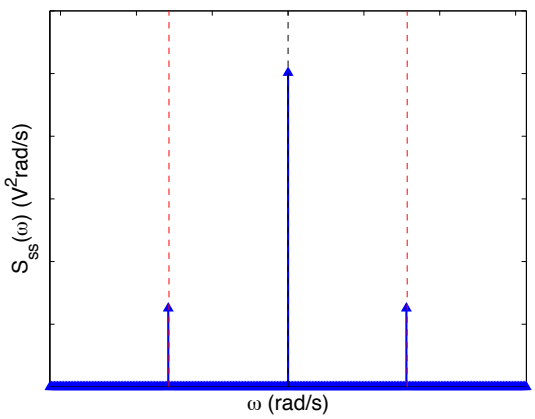

(c) Auto-spectral density of model signal of optical sensor.

Figure 45: Qualitative plots of auto-spectral densities of model signals.

Since all of the model signals share periodic content at $\omega = 2\pi f_c$ all of the cross-spectral densities have the Dirac delta functions $\delta(\omega \pm 2\pi f_c)$. The cross-spectra between $F_f(t)$ and $s(t)$ is the only cross-spectrum that has the Dirac delta function $\delta(\omega)$. This is because those two signals each contain a DC component, while $v_e(t)$ does not. Qualitative plots of the magnitude of the cross-spectrum can be seen in Figure 46.

These qualitative examples of the signal processing, that will be done to the actual test signals, should give some insight as to what should be expected. The autocorrelations and auto-spectra can be used to determine the period and frequency of each of signals, while the cross-correlation and cross spectra can be used to determine what periodic content they share with one another. The cross-correlations can give information about the two signals, such as the phase difference between shared periodic content of two signals.

6.3 MODELING THE PHOTODETECTOR SIGNAL

In the previous section, the optical sensor signal was modeled using a sine wave with a DC component. Although it is a good approximation because it has characteristics we would expect the signal to have, it does not match the shape of the signal seen in Chapter 5 very well.

The signal from the optical sensor could possibly be better modeled as a rectangular pulse train with a DC component, whose period and pulse width are dependent upon the tracking velocity. One period of a rectangular pulse train, with a DC component, S, and a pulse height, P, can be described as a piecewise function

$$s_r(t) = \begin{cases} S & \text{if } 0 \leq t < \tau_c - \tau_p \\ S + P & \text{if } \tau_c - \tau_p \leq t < \tau_c, \end{cases} \tag{6.18}$$

where τ_p is the pulse width. τ_c is the period of the balls passing by the sensing fiber, which is the inverse of $f_c = v/(2d_{avg})$ that is determined from the tracking velocity and the diameter of the balls, as shown in Equation (1.2). Since f_c is the center frequency of the disturbance τ_c is the center period of the periodic disturbance.

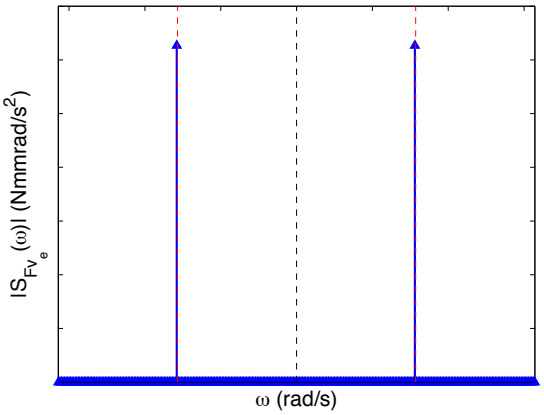

(a) Cross-spectral density between model signal of friction force and velocity error.

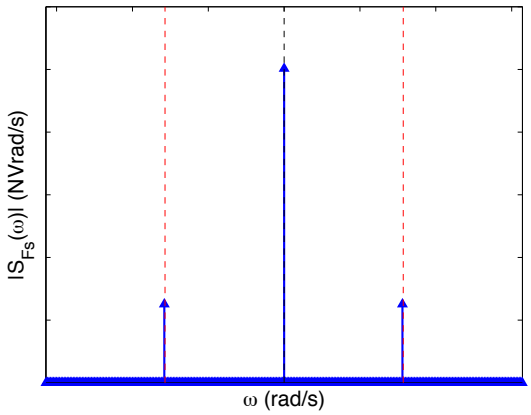

(b) Cross-spectral density between model signal of friction force and optical sensor.

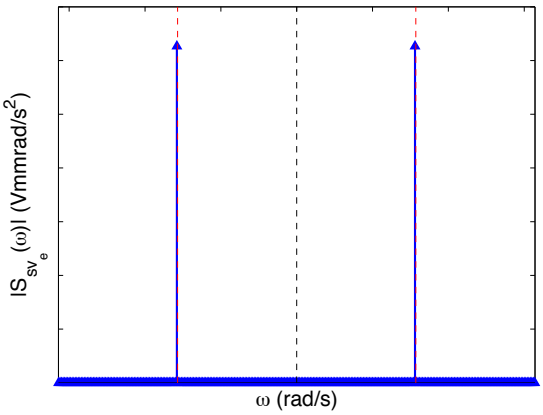

(c) Cross-spectral density between model signal of optical sensor and velocity error.

Figure 46: Qualitative plots of cross-spectral densities of model signals.

A continuous-periodic function of time can be created from the piecewise function of one rectangular pulse using a Fourier series expansion, creating a rectangular pulse train. The periodic function, determined from the Fourier series expansion of the piecewise function, can be written as

$$s_r(t) = S + \frac{a_0}{2} + \sum_{n=1}^{\infty}[a_n \cos(2\pi f_c nt) + b_n \sin(2\pi f_c nt)], \tag{6.19}$$

where a_0, a_n, and b_n are Fourier coefficients that must be solved for. In solving for the Fourier series expansion of the function $s(t)$ the DC component, S, is removed from Equation (6.18) and then added back into the solution. This is why the constant term S appears in the Fourier series described by Equation (6.19). The piecewise function that is used to solve for the Fourier coefficients is

$$\hat{s_r}(t) = \begin{cases} 0 & \text{if } 0 \leq t < \tau_c - \tau_p \\ P & \text{if } \tau_c - \tau_p \leq t < \tau_c. \end{cases} \tag{6.20}$$

Using Equation (6.20) the coefficients of the Fourier series can be solved as

$$\begin{aligned} a_0 &= \tfrac{2}{\tau_c}\int_0^{\tau_c} \hat{s_r}(t)dt = P\frac{\tau_p}{\tau_c} \\ a_n &= \tfrac{2}{\tau_c}\int_0^{\tau_c} \hat{s_r}(t)\cos(2\pi f_c nt)dt = \frac{P\tau_c}{2n\pi}\sin\left(\frac{2\pi\tau_p}{\tau_c}\right) \\ b_n &= \tfrac{2}{\tau_c}\int_0^{\tau_c} \hat{s_r}(t)\sin(2\pi f_c nt)dt = \frac{P\tau_c}{2n\pi}\left[\cos\left(\frac{2\pi\tau_p}{\tau_c}\right) - 1\right], \end{aligned} \tag{6.21}$$

which makes the final solution to the Fourier series expansion, using Equations (6.19) and (6.21),

$$s_r(t) = S + \frac{P\tau_p}{\tau_c} + \sum_{n=1}^{\infty}\frac{P\tau_c}{n\pi}\cos\left(\frac{\pi(2nt+\tau_p)}{\tau_c}\right)\sin\left(\frac{\pi\tau_p}{\tau_c}\right). \tag{6.22}$$

The function for a rectangular pulse train, given by Equation (6.22), can be compared to a signal from an actual test, once the parameters have been determined. The rectangular pulse train model, of order 20, is compared to a measured signal from the optical sensor for a velocity tracking test of 10 mm/s in Figure 47. The comparison of the rectangular pulse train and the measured signal show some similar characteristics. As expected, the frequency and width of the rectangular pulses match the frequency and the width of the pulses from the optical sensor. The Gibbs phenomena causes the oscillations in the neighborhood of

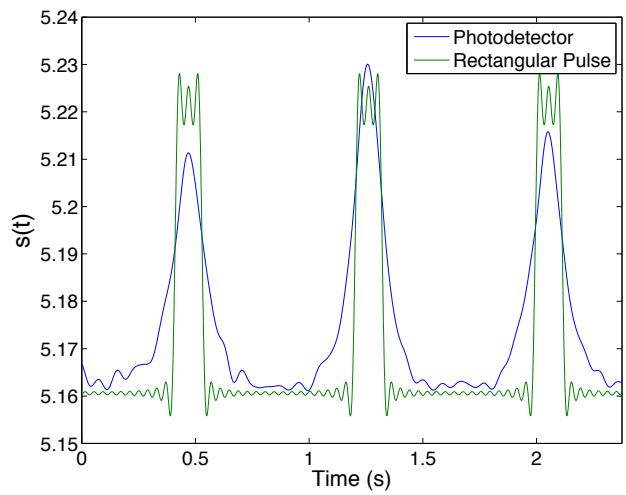

Figure 47: Comparison of the Fourier series expansion of a rectangular pulse train to the signal from the optical sensor. The DC components, amplitudes, pulse frequency, and pulse widths match but there are obvious differences in the shapes of the signals.

jump discontinuities, which is evident in Figure 47 [27]. As the order of the Fourier series of the rectangular pulse train is increased the magnitude of the oscillations at the jump discontinuity will increase. This means that higher order approximations will have greater error at the jump discontinuities.

It can be observed from the plots of the signal from the optical sensor for a velocity tracking test that the shape of the peaks resemble a Gaussian function better than a rectangular pulse. A Gaussian pulse train can be modeled using a sum of Gaussian pulses where each pulse can be described as

$$g_n(t) = P_n \exp\left[-\frac{(t - n\tau_c - t_0)^2}{2\tau_p^2}\right], \tag{6.23}$$

where P_n is the amplitude of the nth pulse and t_0 is the delay of the zeroth pulse. The delay, t_0, is used to align the Gaussian model of the signal with a measured signal to determine how accurately the model fits. By adding up the individual Gaussian pulses, described by Equation (6.23), the signal from the optical sensor can be approximated as

$$s_g(t) = \sum_{n=0}^{\infty} g_n(t) = \sum_{n=0}^{\infty} P_n \exp\left[-\frac{(t - n\tau_c - t_0)^2}{2\tau_p^2}\right]. \tag{6.24}$$

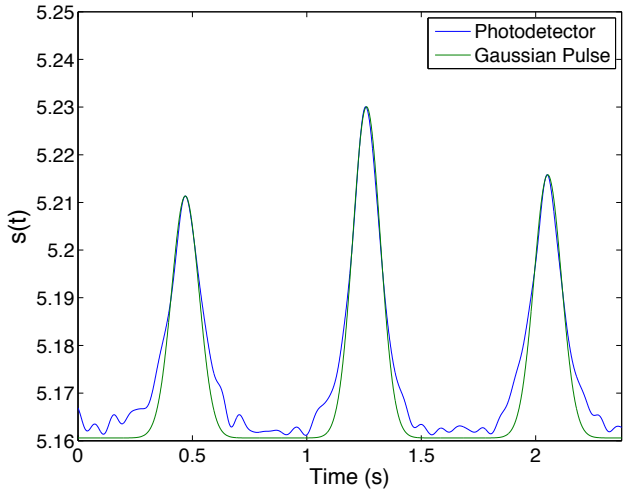

Figure 48: Comparison of the Gaussian function approximation to the signal from the optical sensor. All characteristics of the Gaussian function approximation match the signal from the optical sensor quite well.

To determine how well the Gaussian pulse function approximates the signal from the optical sensor the first three peaks were calculated using Equation (6.24). The plot of the signal from the optical sensor and the Gaussian pulse approximation can be seen in Figure 48. The Gaussian pulse train is clearly a better model of the signal from the optical sensor than the rectangular pulse train or the cosine function, which was used in the previous section. This means that the correlations and the spectral densities calculated with the optical sensor signal will be different from the ones previously calculated and discussed.

It is expected that each time a ball enters the loaded section of the race there is a spike in the friction force. We do not expect the friction force to have a steady oscillation, as was described by the sinusoidal model of friction force in Section 6.1. For this reason, it is likely that the Gaussian pulse train is also a better model of the friction force than the sinusoidal model. If the friction force is modeled using the Gaussian pulse train (described by Equation (6.25)) we can conclude the the frequency response of the friction force will be similar in shape to the frequency response of the optical sensor signal.

From the coefficients of a Fourier series expansion of a Gaussian pulse train the frequency response of a Gaussian pulse train can be determined. Since it has been determined that the Gaussian pulse train is a good model for the optical sensor signal and the friction force, the Fourier coefficients will give some insight into what the frequency responses of the two signals may look like.

The Gaussian pulse function can be approximated through using the Fourier series expansion

$$s_g(t) = \sum_{n=-\infty}^{\infty} C_n \exp\left(j2\pi n \frac{t}{\tau_c}\right), \tag{6.25}$$

where C_n are the Fourier coefficients of the Gaussian pulse train. The coefficients can be calculated using a similar method as used in calculating the coefficients of the Fourier series expansion of the rectangular pulse. The Gaussian Fourier series coefficients can be solved as

$$C_n = \frac{1}{\tau_c} \int_{-\tau_c/2}^{\tau_c/2} g_0(t) \exp\left(-j\pi n \frac{t}{\tau_c}\right) dt, \tag{6.26}$$

where $g_0(t)$ is the zeroth pulse, which can be calculated from Equation (6.23), for $n = 0$. Substituting $g_0(t)$ into Equation (6.26) and solving, the coefficients for the Gaussian Fourier series expansion of the signal are

$$C_n = \sqrt{\pi} \frac{\tau_p}{2\tau_c} \exp\left[-\left(\frac{\pi n \tau_p}{2\tau_c}\right)^2\right]. \tag{6.27}$$

Substituting the coefficients into Equation (6.25) the signal can now be approximated as

$$s_g(t) = \sum_{n=-\infty}^{\infty} \sqrt{\pi} \frac{\tau_p}{2\tau_c} \exp\left[-\left(\frac{\pi n \tau_p}{2\tau_c}\right)^2\right] \exp\left[-j2\pi n \frac{t}{\tau_c}\right]. \tag{6.28}$$

The Gaussian Fourier coefficients are used in Equation (6.28) to model the signal from the optical sensor, however, they can also be used to illustrate the frequency responses of the optical sensor and the friction force. The nth Fourier coefficient, C_n, corresponds to the magnitude of the frequency response at the nth harmonic. A plot of the Fourier coefficients versus normalized frequency can be seen in Figure 49, where the vertical axis is logarithmic. The plot of the Fourier coefficients illustrates that the magnitudes of the harmonics decrease exponentially. This is to be expected since the Fourier coefficients of the Gaussian pulse are

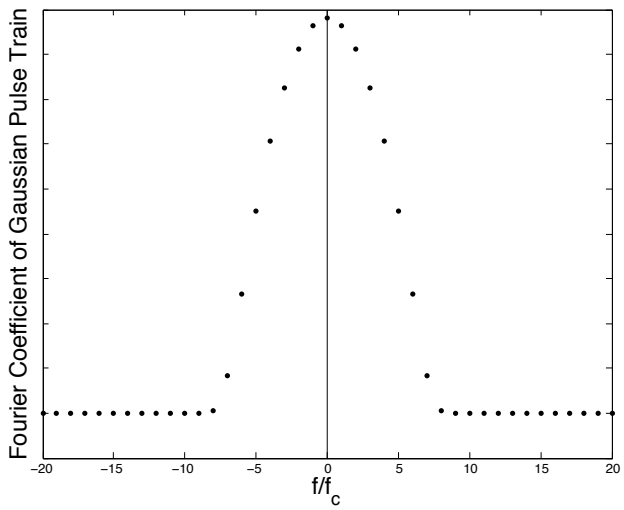

Figure 49: Qualitative plot of Fourier coefficients of a Gaussian pulse train. The vertical axis is logarithmic.

also Gaussian. The exponential decay in the Fourier coefficients means that in the spectral density of the optical sensor signal and the friction force only the first few harmonics will be noticeable. The higher harmonics will likely be indiscernible. From the spectra of the friction force and the transfer function from the friction force to velocity, we can determine what one period of the velocity may look like. This is done by first determining the Fourier coefficients of velocity from the Fourier coefficients of the friction force and the magnitude of their transfer function at the harmonics of f_c.

The transfer function between friction force and the velocity is $G_{vf}(s)$, as determined in Section 6.1, Equation (6.6). The frequency response of velocity can be determined from the frequency response of the friction force and the frequency response of $G(s)$, which is found by setting $s = j\omega$. Thus, the magnitude of the frequency response of velocity is $|V(j\omega)| = |G(j\omega)||F_f(j\omega)|$. A plot of the magnitude of the frequency response of the Gaussian pulse approximation of friction force, the frequency response of the transfer function $G(s)$, and the resulting frequency response of the velocity can be seen in Figure 50. The frequency response of $G(s)$ shows a system with a natural frequency that occurs at a frequency that is

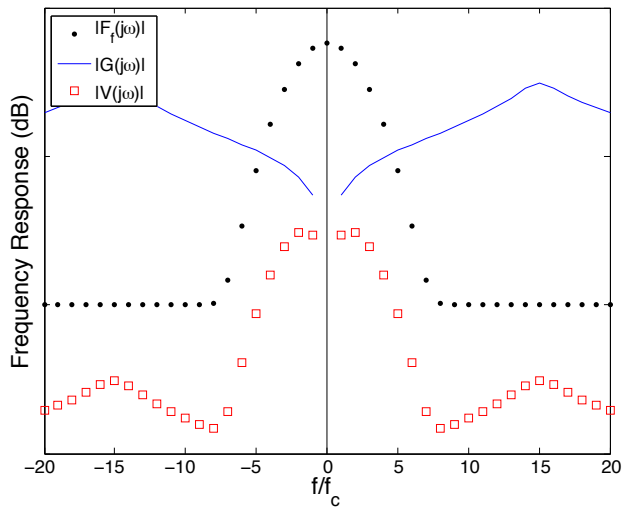

Figure 50: Qualitative plot of the frequency reposes $|F_f(j\omega)|$, $|G(j\omega)|$, and $|V(j\omega)|$. The vertical axis is logarithmic and the horizontal axis is normalized with respect to f_c.

fifteen times f_c, and has very little damping. This was done to make the natural frequency more apparent in the plot. Since f_c is expected to be small, on the order of a few hertz, it is likely that the natural frequency of $G(s)$ will be much greater than f_c. Only the first few harmonics of the frequency response of the friction force will be discernible, and they will likely be well below the natural frequency of $G(s)$. Therefore, it can be concluded that the systems natural frequency will not increase the magnitude of the disturbance in the velocity caused by the increases in friction force.

One period of the expected velocity can be calculated to be

$$v(t) = \sum_{n=-\infty}^{\infty} D_n \exp(jn2\pi f_c t), \tag{6.29}$$

where $D_n = C_n|G(jn2\pi f_c)|$ is the Fourier coefficients of velocity and $|G(jn2\pi f_c)|$ is the magnitude of $G(s)$, evaluated at the harmonics of f_c. A plot of one period of the expected velocity is shown in Figure 51. It is important to recall that plot of the expected velocity

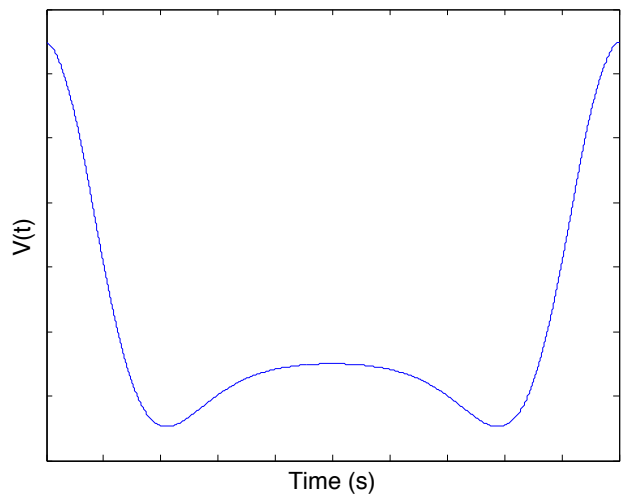

Figure 51: One period of the velocity time response reconstructed from the Fourier coefficients of velocity.

assumes that the system is modeled by $G(s)$, which includes a PD controller, and that the friction force is modeled by a Gaussian pulse train. This plot indicates that if the system is as predicted we can expect the velocity to have spikes with some oscillations at the base of the spikes.

6.4 CENTER PERIOD AND PULSE WIDTH OF OPTICAL SENSOR SIGNAL

The parameters τ_c, the center period, and τ_p, the pulse width, appear in many of the equations described in this chapter. It has been observed from velocity tracking tests that these parameters vary with the tracking velocity, and it is believed that they are both inversely proportional to tracking velocity. If they are both proportional to tracking velocity then it can be concluded that their ratio, which appears in multiple equations in the previous section, should be constant for all tracking velocities. To show that the parameters τ_c and τ_p are both inversely proportional to velocity, the two parameters were calculated from the

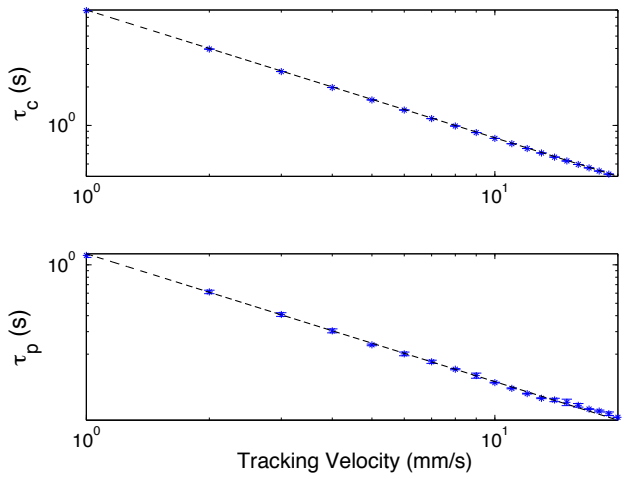

Figure 52: Logarithmic plots of τ_c and τ_p versus tracking velocity. These logarithmic plots show that τ_c and τ_p are both inversely proportional to the tracking velocity.

optical sensor signal during velocity tracking tests. Five tests were performed at each tracking velocities ranging from 1 mm/s to 20 mm/s, incrementing by 1 mm/s. The values of τ_c and τ_p were averaged for each peak during each test, and then averaged over the five tests at that velocity. The resulting calculated values for τ_c and τ_p are plotted versus the tracking velocity on a logarithmic scale as seen in Figure 52. The standard deviations are also shown using error bars; however, because the vertical axis is logarithmic they appear insignificant. By plotting the parameters versus tracking velocity on a logarithmic scale if the τ_c and τ_p are inversely proportional to tracking velocity then their plots will appear to be linear, as it does in Figure 52. This means that the parameters are both inversely proportional to velocity. Since both τ_c and τ_p are inversely proportional to tracking velocity then their ratio is constant for all tracking velocities.

The ratio τ_p/τ_c was calculated from the average values of τ_c and τ_p for each trial, and then averaged over the five tests at that tracking velocity. The result is plotted versus the tracking velocities, as seen in Figure 53. The horizontal black-dashed line in the plot illustrates the mean of the twenty data points from the twenty different constant tracking velocities that were tested. The error bars in Figure 53 illustrate the standard deviation calculated for the

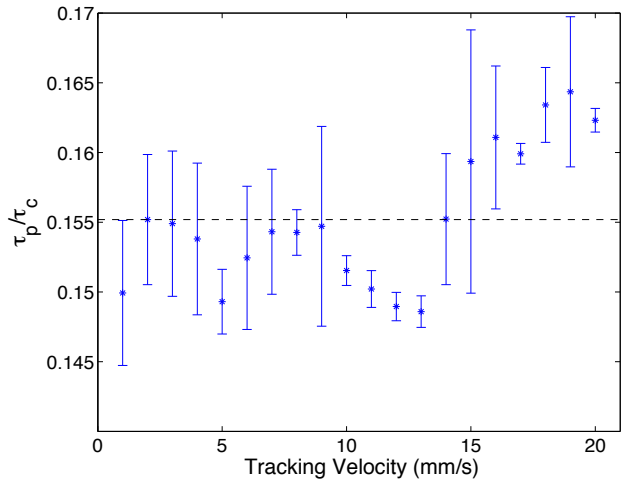

Figure 53: Ratio of τ_p and τ_c. The horizontal black-dashed line is the mean of all of the ratios and the error bars are generated from the variance of τ_p and τ_c for each individual peak in the signal.

τ ratio of the five trials at each tracking velocity. From Figure 53 it can be concluded that $\tau_p/\tau_c = 0.155$, which is the mean of all of the τ ratios, is a good approximation for the τ ratio that is constant for all tracking velocities.

7.0 VELOCITY TRACKING TESTS

To demonstrate that the friction force, velocity error, and the signal from the optical sensor contain periodic content, with a frequency of approximately f_c, multiple velocity tracking tests were run at different velocities. The autocorrelations and auto-spectrum of the three signals will be used to show that each signal contains periodic content at the frequency $f_c = v/(2d_{avg})$. The cross-correlations and cross-spectrum of the three signals will be used to show what frequencies the signals are correlated at.

For each velocity tracking test the air bearing stage begins from rest, accelerates to the tracking velocity, and then travels at a controlled velocity. Once the stage has settled to the tracking velocity the signals from the load cell, optical encoder, and optical sensor are sampled and recorded. The data recording does not begin at the exact moment the stage begins moving so that the inertial effects from the acceleration of the stage are not recorded. The transients, which result from the acceleration of the stage, are are excluded by giving the signal acquisition a distance that triggers the recording. This distance is determined from the acceleration rate and the tracking velocity, and allows enough time for the transients to dissipate before the signal is recorded. The transients are not recorded because they could potentially affect the signal processing that will be done. An example of the sampled signals for a velocity tracking test of 9 mm/s with $F_s = 1000\,\text{Hz}$ can be see in Figure 54.

In the plot of the friction force, $F_f(t)$, seen in Figure 54 we can see that the signal does not maintain its DC component very well. The load cell's specified time constant should be $\geq 50\,\text{s}$, as previously discussed, however it appears that the signal dissipates much quicker than expected, and also goes negative after approximately 10 s. Since we are more concerned with the AC components of the signal from the load cell, the fast dissipation of the load cell's DC component should not affect the signal processing that will be done later.

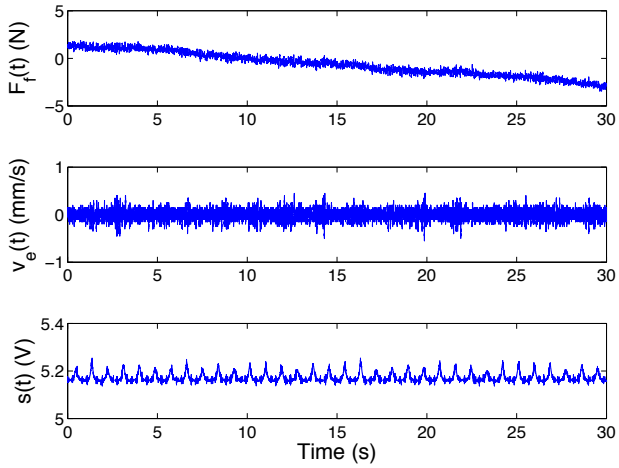

Figure 54: Signals acquired for a velocity tracking test at 9 mm/s (corresponds to τ_c =0.901 s). The signals from top to bottom are the signals from the load cell, the encoder, and the photodetector respectively.

Velocity tracking test were performed for tracking velocities of 1 mm/s to 20 mm/s, incrementing by 1 mm/s. Five velocity tracking tests were performed for each tracking velocity. Since the velocity tracking error at 9 mm/s showed the highest standard deviation in Chapter 4 (see Figure 29), the calculations of the correlations and the power spectral densities shown in this chapter will all be for a tracking velocity of 9 mm/s. The time duration of each test was 30 s, with a sampling frequency of $F_s = 1000$ Hz. The signals of the friction force and the optical sensor were filtered using analog low-pass filters, with a cutoff of 400 Hz, before sampling to reduce aliasing. The signal from the optical encoder is decoded by dSPACE and therefore cannot be analog filtered before it is sampled. The digital signals were then low-pass filtered, using a 5th order Butterworth filter with a cutoff frequency of 20 Hz, and detrended before the correlations and power spectral densities were calculated. This was done to make the lower frequency content more apparent. The correlations and spectral densities were calculated for each test. Then the five resulting correlations and spectral densities that were calculated for the same tracking velocity were averaged to reduce noise.

The signals acquired from the sensors are discrete time signals, unlike the continuous time signals used in the analysis of the model signals. This means that the continuous time signal processing methods, discussed in Section 6.2, must be redefined for discrete time signals. Although the signal processing methods will be redefined for discrete time signals, we expect the resulting correlations and spectra to be similar to the results achieved for the continuous time model signals. The discrete time signal processing techniques used are referenced from Oppenheim and Schafer [27].

7.1 CORRELATION ANALYSIS

Given two discrete time signals, $x[n]$ and $y[n]$, the cross-correlation of $x[n]$ with $y[n]$ is defined as

$$R_{xy}[m] = \sum_{n=-\infty}^{\infty} x[n+m]y[n], \tag{7.1}$$

where n is the index of the discrete time signal and m is the index of the cross-correlation. The index n is related to time t through the sampling period, $T_s = 1/F_s$, which for these tests is 1 ms. Similarly, the index m is related to the correlation time τ through T_s. These relations are expressed as $t = nT_s$ and $\tau = mT_s$.

The cross-correlation of two signals is used to show how two signals are related in time. Periodic increases in the cross-correlation of two signals illustrates that the two signals share periodic content, with a period equal to the difference in τ between peaks. Information about the phase between the shared periodic content can also be determined from the cross-correlation. Cross-correlations that are low at $\tau = 0$ and then increase periodically indicate that there is some phase between the shared periodic content of the signals. Also, as previously discussed in Chapter 6, because $R_{xy}(\tau) = R_{yx}(-\tau)$ it is only necessary to calculate three cross-correlations for the three signals.

From the definition of the cross-correlation in Equation (7.1) we can define the discrete time autocorrelation, which is the cross-correlation of a signal with itself. The autocorrelation of a discrete time signal, $x[n]$, is defined as

$$R_{xx}[m] = \sum_{n=-\infty}^{\infty} x[n+m]x[n]. \tag{7.2}$$

The autocorrelation is used to show how a signal is correlated with itself in time, and is used to reveal periodic content of a signal. Like the cross-correlation, periodic increases in the autocorrelation indicate that the signal contains periodic content, whose period is equal to the change in τ between peaks in the autocorrelation. Since the phase between any signal and itself is always zero the autocorrelation of a signal will always be greatest at $\tau = 0$, and the periodic content of a signal will appear as increases in the autocorrelation for positive and negative integer multiples of its period.

First to illustrate the periodic content of the friction force, velocity error, and the optical sensor signal the autocorrelation of each signal was calculated. The signals were low-pass filtered and detrended before their autocorrelations were calculated to make the lower frequency content more apparent in the plots. The calculated autocorrelation of the friction force is shown in Figure 55. The vertical red-dashed lines in the zoomed plot of the autocorrelation of the friction force are used to illustrate the positive and negative integer multiples of $\tau_c = 0.901\,\mathrm{s}$, the expected period of the disturbance for a tracking velocity of $9\,\mathrm{mm/s}$. As seen in Figure 55 there is an increase in the autocorrelation of the friction force at the integer multiples of τ_c. This means that the measured signal of the friction force has some periodic content with a period of approximately $\tau_c = 0.901\,\mathrm{s}$.

Next the autocorrelation was calculated from the velocity error for a $9\,\mathrm{mm/s}$ velocity tracking test. The calculated autocorrelation of the velocity error is shown in Figure 56. Again vertical red-dashed lines are used to indicate integer multiples of $\tau_c = 0.901\,\mathrm{s}$. The periodic increases in the autocorrelation of the velocity error at integer multiples of τ_c indicate that the velocity error contains some periodic content with a period of $\tau_c = 0.901\,\mathrm{s}$.

Finally the autocorrelation of the optical sensor signal, for a $9\,\mathrm{mm/s}$ velocity tracking test, was calculated. The resulting autocorrelation of the signal from the optical sensor is shown in Figure 57. Like the autocorrelations of friction force and velocity error, the autocorrelation

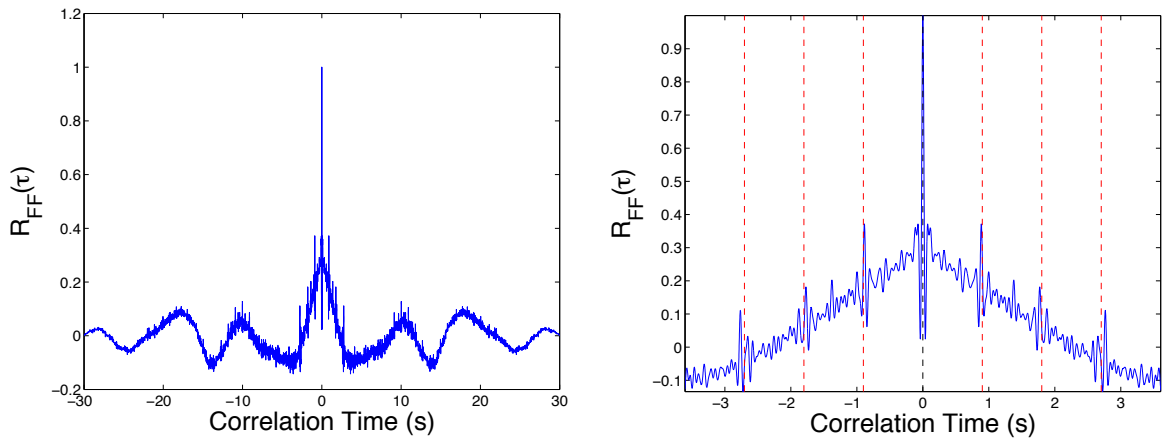

(a) (b)

Figure 55: Autocorrelation of friction force for a velocity tracking test at 9 mm/s (corresponds to $\tau_c = 0.901$ s). (a) Full temporal range for the $R_{F_f F_f}(\tau)$ (b) Zoomed section of $R_{F_f F_f}(\tau)$ showing the range of delay times within a few multiples of the expected period of the disturbance. The vertical red-dashed lines indicate periodicities of τ_c.

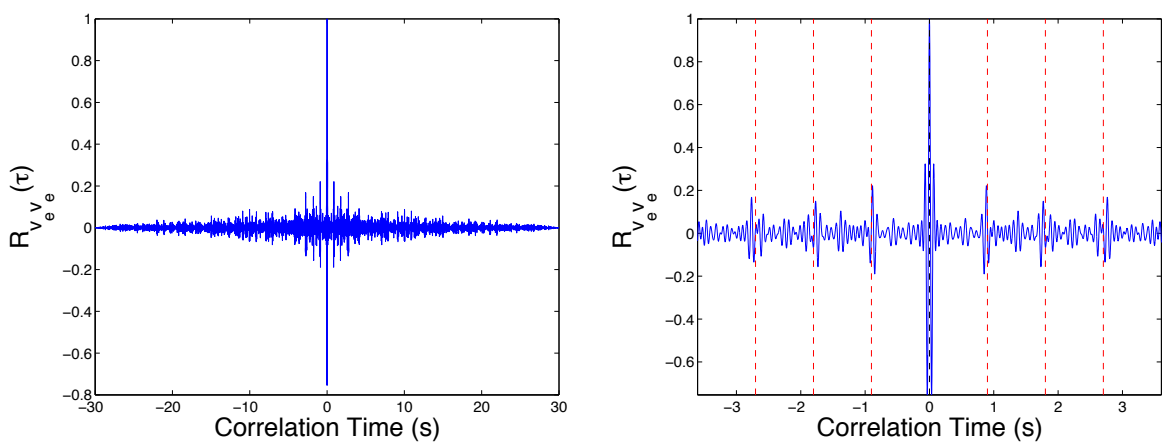

(a) (b)

Figure 56: Autocorrelation of velocity error for a velocity tracking test at 9 mm/s (corresponds to $\tau_c = 0.901$ s). (a) Full temporal range of $R_{v_e v_e}(\tau)$. (b) Zoomed section of $R_{v_e v_e}(\tau)$ showing the range of delay times within a few multiples of the expected period of the disturbance. The vertical red-dashed lines indicate periodicities of τ_c.

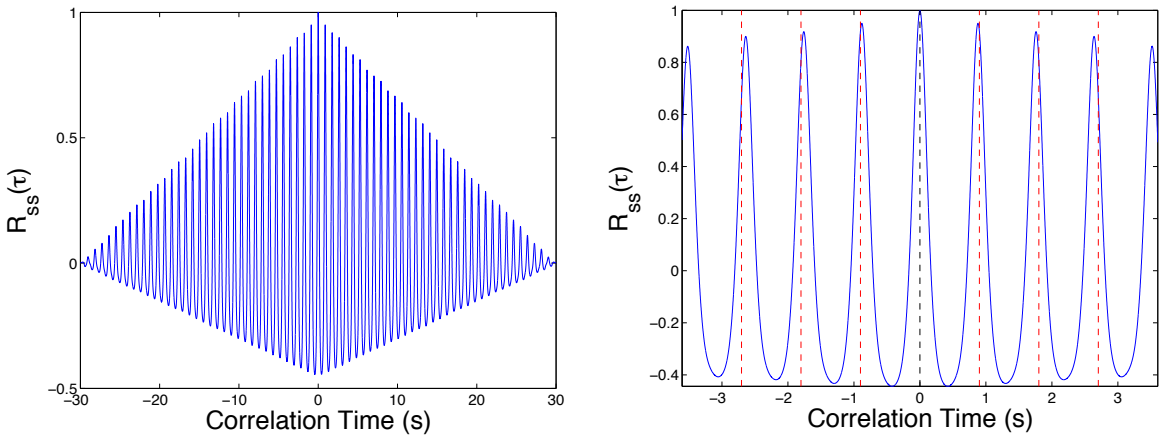

(a) (b)

Figure 57: Autocorrelation of the optical sensor signal for a velocity tracking test at 9 mm/s (corresponds to $\tau_c = 0.901\,\mathrm{s}$). (a) Full temporal range of $R_{ss}(\tau)$. (b) Zoomed section of $R_{ss}(\tau)$ showing the range of delay times within a few multiples of the expected period of the disturbance. The vertical red-dashed lines indicate periodicities of τ_c.

of the optical sensor signal increases periodically at integer multiples of $\tau_c = 0.901\,\mathrm{s}$. This illustrates that the estimated value of τ_c, calculated from the inverse of Equation (1.2), is a good approximation for the period of the ball passage. Also it can be observed from Figure 57 that the shape of the peaks in the autocorrelation have a Gaussian shape.

The autocorrelations of the friction force, velocity error, and optical sensor signal all showed that each signal contained some periodic content with a period that was approximately equal to τ_c. The cross-correlations between the three signals can reveal how the signals are periodically related with each other in the time domain and if the shared periodic content has any relative phase. Since the autocorrelations of the three signals revealed that they each contain periodic content with a period of approximately τ_c we would expect the cross-correlations to illustrate that they share that periodic content. Like the autocorrelation, periodic increases in the cross-correlation of two signals illustrate that the two signals share periodic content with a period equal to the difference in τ between peaks. Unlike the autocorrelation, a phase difference between shared periodic content of two signals can be de-

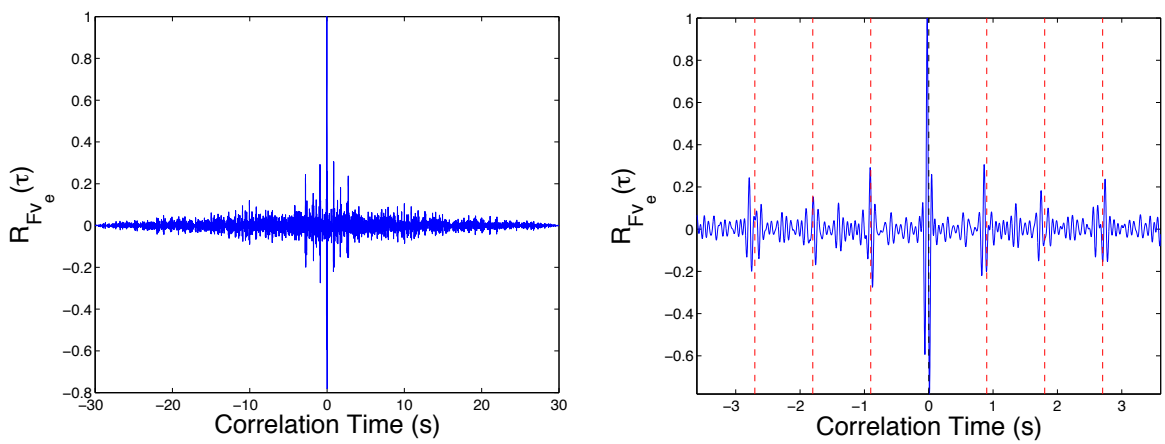

(a) (b)

Figure 58: Cross-correlation between friction force and velocity error for a velocity tracking test at 9 mm/s (corresponds to $\tau_c = 0.901$ s). (a) Full temporal range of $R_{F_f v_e}(\tau)$. (b) Zoomed section of $R_{F_f v_e}(\tau)$ showing the range of delay times within a few multiples of the expected period of the disturbance. The vertical red-dashed lines indicate periodicities of τ_c.

termined from the cross-correlation. The relative phase difference will result in the periodic increases in the cross-correlation being shifted from $\tau = 0$. The phase difference between the shared periodic content can be determined from the peak in the cross-correlation that occurs closest to $\tau = 0$.

The calculated cross-correlation between friction force and velocity error is shown in Figure 58. As previously done with the autocorrelations the plots of the cross-correlations will also use vertical red-dashed lines to indicate the first few periodicities of τ_c. The plot of the cross-correlation of friction force with velocity error has periodic increases in the cross-correlation at integer multiples of τ_c. This illustrates not only that the two signals share periodic content with a period of $\tau_c = 0.901$ s, but it also illustrates that the phase difference of the shared periodic content of the two signals is zero. It can be determined that the phase difference is zero because a peak in the cross-correlation occurs at $\tau = 0$.

The calculated cross-correlation between friction force and optical sensor signal is shown in Figure 59. Unlike the cross-correlation between the friction force and the velocity error the cross-correlation between the friction force and the optical sensor signal does not have periodic peaks occurring at integer multiples of τ_c. Although the periodic peaks do not occur at integer multiples of τ_c it can be observed from Figure 59 that distance between each peak in the cross-correlation is approximately $\tau = 0.901\,\mathrm{s}$. This indicates that the friction force and the optical sensor signal share periodic content with a period of $0.901\,\mathrm{s}$, as expected.

In Figure 59, the periodic peak in the cross-correlation that occurs closest to $\tau = 0$ is the peak at $\tau = -0.39\,\mathrm{s}$. This means that the optical sensor signal must be delayed by $0.39\,\mathrm{s}$ for the periodic content of the optical sensor signal to be in phase with the friction force. A delay of $0.39\,\mathrm{s}$, corresponding to a periodicity of $0.901\,\mathrm{s}$, would result in a phase difference of $-125°$. This means that the periodic content with a period of τ_c of the signal from the optical sensor signal has a phase of $-125°$ relative to the similar periodic content of the friction force.

The calculated cross-correlation between the velocity error and the optical sensor signal is shown in Figure 60. Like the cross-correlation between friction force and optical sensor signal, the cross-correlation between the velocity error and the optical sensor signal has periodic peaks that do not occur at integer multiples of τ_c. However, the distance between the peaks is approximately τ_c. This means that the velocity error and the optical sensor signal shared periodic content with a period of approximately $\tau_c = 0.901\,\mathrm{s}$, and have some phase difference.

In Figure 60 the periodic peak in the cross-correlation closest to $\tau = 0$ occurs at $\tau = 0.41\,\mathrm{s}$, which would correspond to a phase difference of $133°$. The phase of the optical sensor signal relative to the friction force is $-125°$ and the phase of the velocity error relative to the optical sensor signal is $133°$. Therefore it would make sense that the phase of the velocity error relative to the friction force is approximately zero, as was illustrated in the plot of the cross-correlation of the friction force and the velocity error.

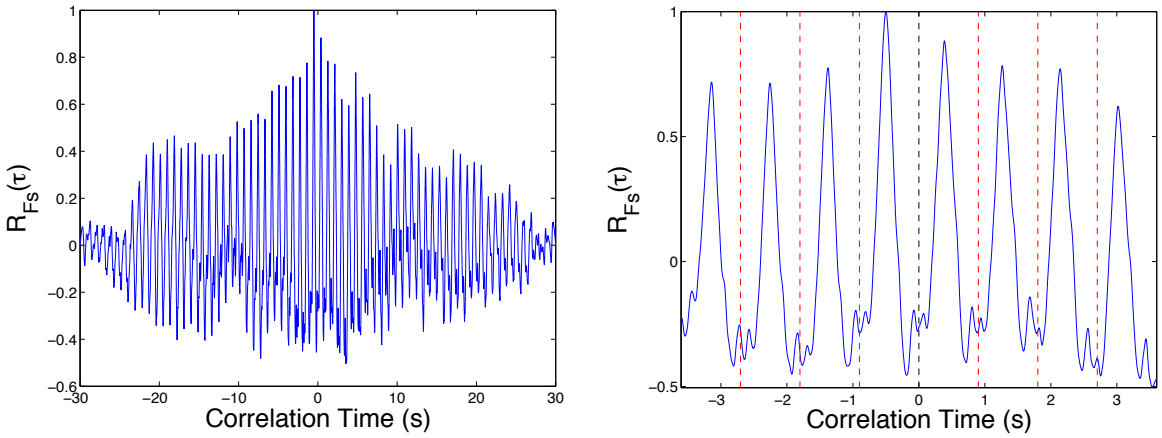

(a) (b)

Figure 59: Cross-correlation between friction force and optical sensor signal for a velocity tracking test at 9 mm/s (corresponds to $\tau_c = 0.901$ s). (a) Full temporal range of $R_{F_f s}(\tau)$. (b) Zoomed section of $R_{F_f s}(\tau)$ showing the range of delay times within a few multiples of the expected period of the disturbance. The vertical red-dashed lines indicate periodicities of τ_c.

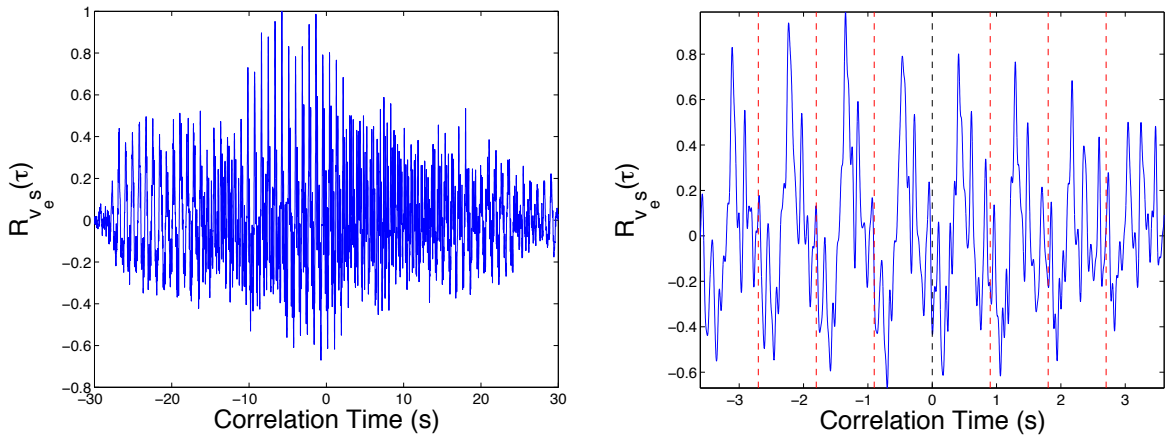

(a) (b)

Figure 60: Cross-correlation between velocity error and optical sensor signal for a velocity tracking test at 9 mm/s (corresponds to $\tau_c = 0.901$ s). (a) Full temporal range of $R_{vies}(\tau)$. (b) Zoomed section of $R_{v_e s}(\tau)$ showing the range of delay times within a few multiples of the expected period of the disturbance. The vertical red-dashed lines indicate periodicities of τ_c.

7.2 POWER SPECTRAL DENSITY ANALYSIS

Given two discrete time signals, $x[n]$ and $y[n]$, the cross-spectral density between the two signals is defined as

$$S_{xy}[\omega] = \mathcal{F}[R_{xy}[m]] = \frac{1}{2\pi} \sum_{m=-\infty}^{\infty} R_{xy}[m] e^{-j\omega m}, \tag{7.3}$$

where $\mathcal{F}$ is the discrete Fourier transform (DFT). Like the continuous time cross-spectral densities, illustrated in Section 6.2, the discrete time spectral density shown in Equation (7.3) is symmetric about $\omega = 0$. It is for this reason that it is only necessary to observe one side of the spectral density. However, since the left-half plane of the cross spectrum contains half the power if only one side is being observed $S_{xy}[\omega]$ must be doubled for magnitude correction.

Similar to the cross-spectral density, defined by Equation (7.3), the auto-spectral density is defined as the DFT of the autocorrelation, which is expressed as

$$S_{xx}[\omega] = \mathcal{F}[R_{xx}[m]] = \frac{1}{2\pi} \sum_{m=-\infty}^{\infty} R_{xx}[m] e^{-j\omega m}. \tag{7.4}$$

Like the cross-spectral density the auto-spectral density is symmetric about $\omega = 0$, which means that it is only necessary to observe one side of the spectrum. Also like the cross-spectrum, if only one side of the auto-spectrum is being observed $S_{xx}[\omega]$ must be doubled for magnitude correction. The auto-spectrum will illustrate frequency content of one signal, while the cross-spectrum will illustrate frequency content shared by two signals.

The Nyquist-Shannon sampling theorem states that the bandwidth of discrete time signals are limited to half of the sampling frequency. As discussed previously in this chapter the sampling frequency used in the tests is $F_s = 1000\,\text{Hz}$. This means that the Nyquist frequency is $F_N = 500\,\text{Hz}$. Due to the range of tracking velocities used in the tests, which is $1\,\text{mm/s}$ to $20\,\text{mm/s}$, we would expect the range of f_c to be $0.12\,\text{Hz}$ to $2.47\,\text{Hz}$. This range of f_c is well within the bandwidth of the spectral densities, according to the Nyquist-Shannon sampling theorem. Although the range of frequencies that we wish to observe are well within

the bandwidth it may be difficult to achieve a good estimation of the power spectrum at such low frequencies. This is because the frequency bin spacing is too large, or there is too much noise in the spectrum.

The frequency bin spacing is calculated as $\Delta f = F_N/N$, where N is the number of points used in the DFT. This means that the resolution of the power spectrum can be increased by increasing N, or by decreasing F_N. For tests of the same time duration if N was increased, or if F_N was decreased, the length of the recorded signal would be decreased. This would decrease the number of averages used to calculate the power spectrum, increasing the noise in the power spectrum. To increase the resolution of the power spectrum while maintaining the number of averages the time duration of the tests would have to be increased. However, due to physical limitations, specifically the length of the guide rail, the time duration of the tests is limited.

To increase the resolution of the power spectrum, without reducing the number of averages or increasing the time duration of the tests, a method of zoom processing is used. The recorded signals from the sensors are processed using a series of decimations and delays, which reduces the bandwidth of the power spectrum without reducing F_s. A discrete block diagram of the method is illustrated in Figure 61, where M is the decimation factor. If a decimation factor of M is used then the signal $x[n]$ is split into M signals. The M signals that result from the series of decimations and delays each contain unique data points of the original signal, and all have the same frequency content. The bandwidth of each of the M signals has been reduced from F_N to F_N/M, and the frequency bin spacing has been reduced from F_N/N to $\frac{F_N}{NM}$, without decreasing the number of averages used in calculating the power spectrum. This method allows for increased resolution at lower frequencies while maintaining a sufficient number of averages to reduce the noise.

From the test signals acquired, and using the discussed method of a series of delays and decimations to better resolve lower frequencies, the auto and cross-spectral densities were calculated. The auto-spectra of the three acquired signals will illustrate the frequency content of each signal, while the cross-spectra of the three signals will illustrate the frequency content which they share.

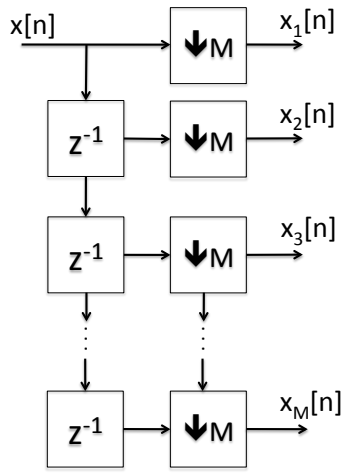

Figure 61: Series of delays and decimations used to segment the signal $x[n]$ into M segments that each contain unique points of $x[n]$ but have the same frequency content. The bandwidth of the signals is reduced from F_N to F_N/M.

First, the full range of the auto-spectra was calculated using Welch's method. Since the sampling frequency used was 1000 Hz the range of the auto-spectra is 0 Hz to 500 Hz. The full range of the calculated auto-spectra of the friction force, velocity error, and optical sensor are shown in Figure 62. The plot of the full available range of the auto-spectra show that most of the frequency content of the three signal is in the lower frequency range, approximately 0 Hz to 25 Hz. The higher frequency content appears flat for the most part, which indicates that it is mostly white noise.

As previously discussed, the low frequencies cannot be resolved very well from these auto-spectra, so the zoom processing method discussed in this chapter was used alongside Welch's method. Before the auto-spectra were calculated the signals were low-pass filtered and detrended, as done before calculating the correlations, to make the low frequency content more apparent. The auto-spectra of friction force, velocity error, and optical sensor signal resolved in the range of 0 Hz to 10 Hz is shown in Figure 63.

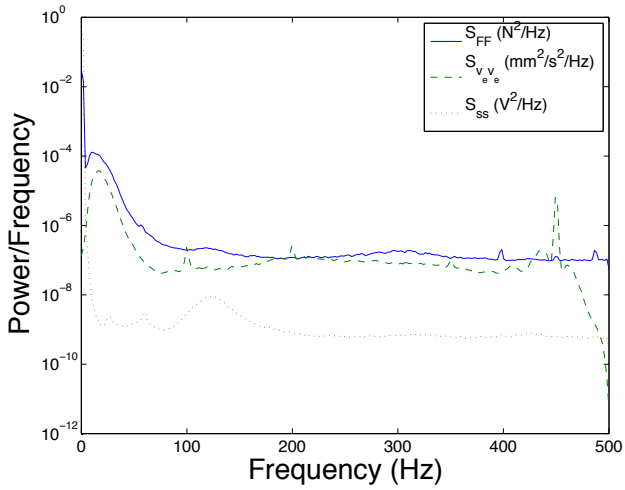

Figure 62: Full range of auto-spectra calculated from friction force, velocity error, and optical sensor signal for a velocity tracking test at 9 mm/s .

The vertical red-dashed lines in Figure 63 are used to illustrate $f_c = 1.110\,\text{Hz}$, as well as higher harmonics. The auto-spectra from the friction force and velocity error, as seen in Figure 63 (a) and (b), do not appear to have frequency content at f_c, even though their autocorrelations appeared to have some periodic content at that frequency. The auto-spectrum of optical sensor signal, shown in Figure 63 (c), shows that the optical sensor signal does have frequency content at f_c because of the increases in the auto-spectrum at f_c and its harmonics. As can also be observed from the auto-spectrum of the optical sensor signal the harmonics appear to decrease exponentially. This is as would be expected, considering the Fourier coefficients of the Gaussian pulse train discussed in Section 6.2.

To illustrate the frequency content that is shared by friction force, velocity error, and optical sensor signal their cross-spectra were calculated. The full available range of the cross-spectra, that was calculated before the signals were low-pass filtered and detrended, is shown in Figure 64. The cross-spectra in Figure 64 show that the shared periodic content with the greatest magnitudes occur at low frequencies, as would be expected from the plot of the full available range of the auto-spectra.

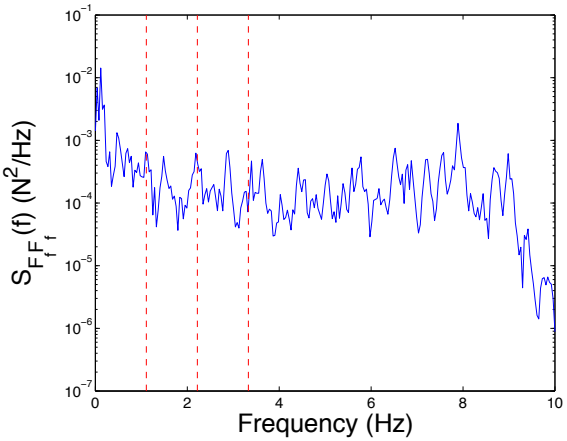

(a) Zoom processed auto-spectrum of friction force.

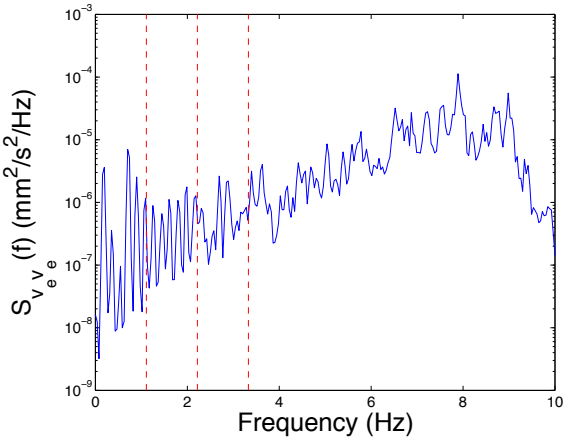

(b) Zoom processed auto-spectrum of velocity error.

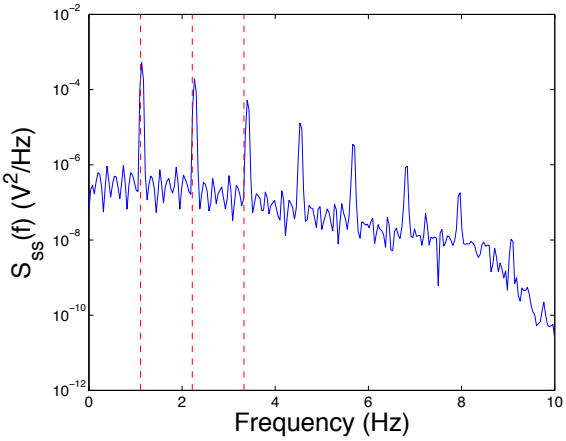

(c) Zoom processed auto-spectrum of optical sensor signal.

Figure 63: Auto-spectra of friction force, velocity error, and optical sensor signal for a velocity tracking test at 9 mm/s (corresponds to $f_c = 1.110$ Hz). The vertical red-dashed lines indicate indicate the expected fundamental frequency of the disturbance and higher harmonics.

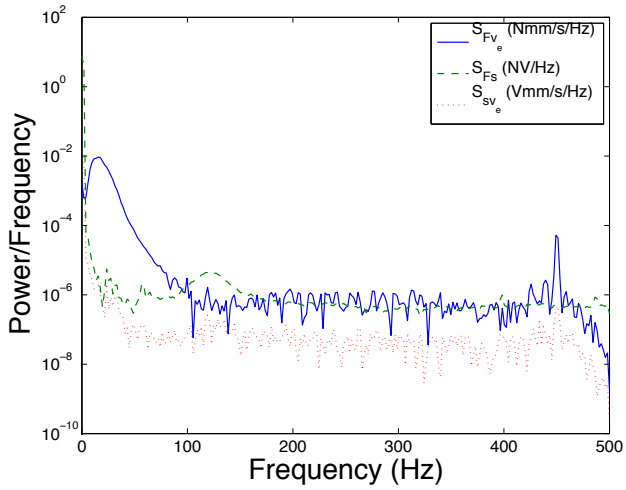

Figure 64: Full range of cross-spectra calculated from friction force, velocity error, and optical sensor signal.

As was done with the auto-spectra, the zoom processing method alongside Welch's method was used to achieve better resolution at low frequencies. Also, the signals were low-pass filtered and detrended before the cross-spectra were calculated. The zoom processed cross-spectra of the three signals can be seen in Figure 65.

As previously done for the plots of the zoom processed auto-spectra, vertical red-dashed lines in the plots of the cross-spectra are used to indicate $f_c = 1.110\,\text{Hz}$, and higher harmonics. Although the optical sensor signal appears to share frequency content with the velocity error and the friction force at approximately f_c, as seen in Figure 65 (b) and (c), the friction fore does not appear to share frequency content with the velocity error at f_c. This is unexpected because both signals appear to share frequency content with the optical sensor signal at the same frequency, and the cross-correlation of friction force and velocity error (see Figure 58) illustrated that the two signals share some periodic content with a period of approximately τ_c. It was shown in Section 6.2 that the magnitude of the peaks in the cross-spectrum are dependent on the amplitudes of the periodic components of the signals. It is likely that the amplitudes of the periodic components with frequency f_c are quite small, making the peaks in the cross-spectrum indiscernible from the noise in the spectrum.

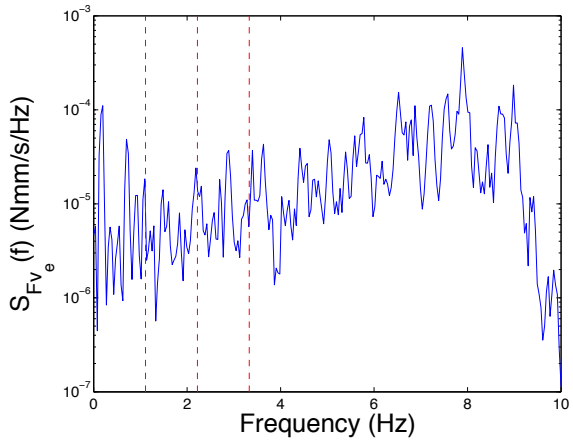

(a) Zoom processed cross spectrum between friction force and velocity error.

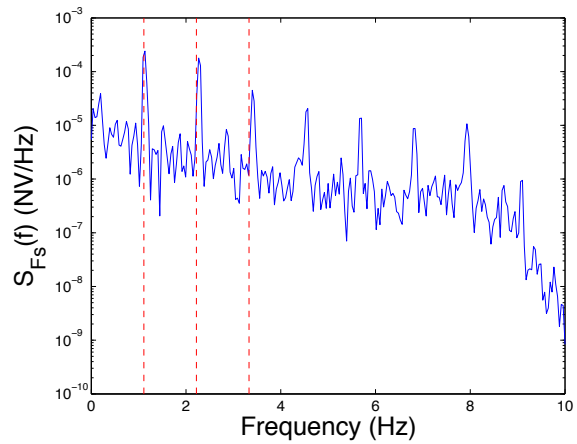

(b) Zoom processed cross spectrum between friction force and optical sensor signal.

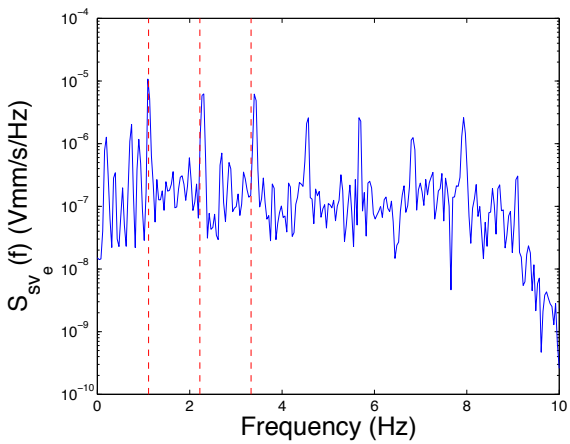

(c) Zoom processed cross spectrum between velocity error and optical sensor signal.

Figure 65: Cross-spectra between friction force, velocity error, and optical sensor signal for a velocity tracking test at 9 mm/s (corresponds to $f_c = 1.110\,\mathrm{Hz}$). The vertical red-dashed lines indicate indicate the expected fundamental frequency of the disturbance and higher harmonics.

8.0 EVALUATION OF ROLLING ELEMENT BEARINGS PERFORMANCE USING FRICTION FORCE AUTO-SPECTRA

Some rolling element bearings have exhibited abnormal and unsystematic behavior, such as sticking during tracking velocity motion. This behavior can be noticed simply by pushing a mechanical bearing by hand along a guide rail, and is believed to be caused by the motion of the balls. While moving the bearing along the guide rail at certain erratic positions the ball bearing will feel as if it is stuck in its current position along the rail. The force needed to move the bearing from the position in which it sticks is much greater than the maximum static friction force.

To determine how this behavior could be identified five SR25W ball bearings were tested ten times each for a tracking velocity of 20 mm/s using the previously discussed test setup. One of the ball bearings exhibited the irregular sticking behavior previously discussed. That ball bearing is Bearing 4 in the following discussion of the results. A plot of the load cell signals for Bearing 1 and Bearing 4, during one of the tracking velocity tests, can be seen in Figure 66. It is apparent in Figure 66 that Bearing 4 exhibits erratic spikes in friction force whose magnitude is up to ten times the friction force seen by Bearing 1. The magnitude of these spikes appear to be very random; however, the spikes in the friction force appear to be periodic with a period of approximately $\tau_c = 0.405\,\mathrm{s}$. To investigate the periodic nature of the friction force spikes the auto-spectra of the five test bearings were calculated, as done in the previous chapter, and compared. The resulting auto-spectra of the friction force of the five bearings is shown in Figure 67. From Figure 67 it can be observed that the auto-spectrum of Bearing 4 is an order of magnitude greater than the auto-spectra of the other bearings at low frequencies (less than 25 Hz). This is expected because the frequency of the spikes in the friction force of the bad bearing occur at a frequency of $f_c = 2.47\,\mathrm{Hz}$.

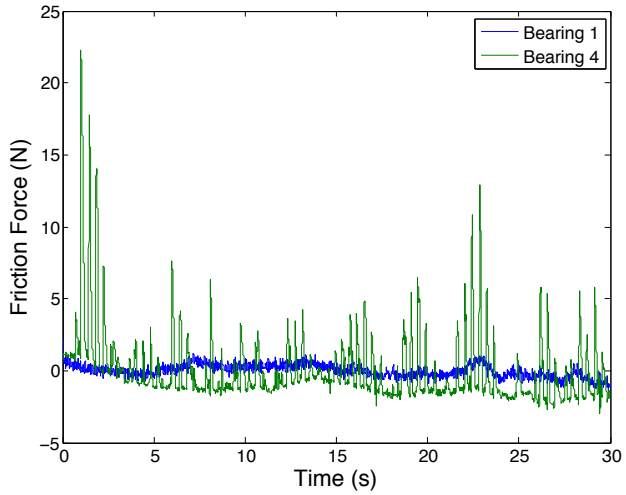

Figure 66: Friction force measurements from two different bearings during constant tracking velocity motion. Bearing 1 is considered to be a good bearing while Bearing 4 is considered to be a bad bearing.

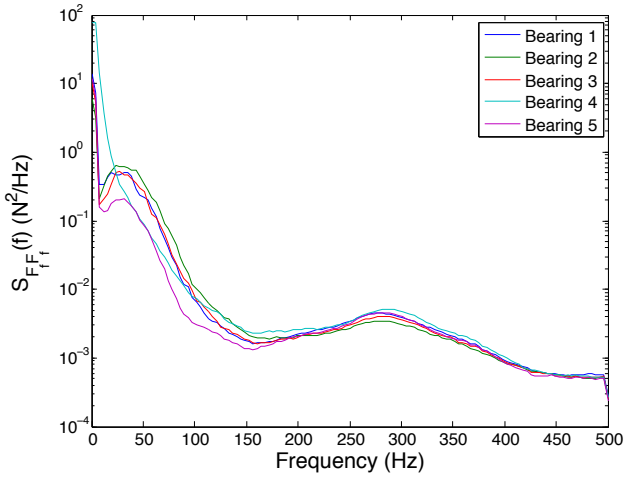

Figure 67: Auto-spectra of the friction force for 5 different bearings that were calculated from tracking velocity tests at 20 mm/s. Bearing 4 is considered to be a bad bearing that exhibits an abnormal sticking behavior during motion.

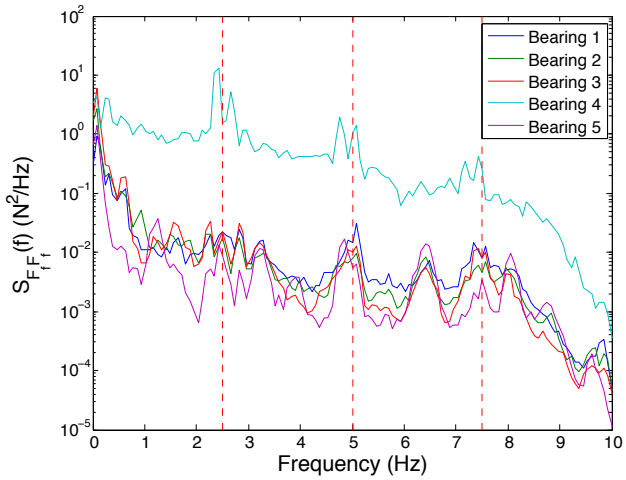

Figure 68: Auto-spectra at low frequencies of the friction force of 5 different bearings that were tested during a constant tracking velocity of 20 mm/s. Bearing 4 is considered to be a bad bearing that exhibits a sticking behavior during motion.

Since the greatest difference in the auto-spectra of the five bearings appears to occur in the low frequency range the previously discussed method of using a series of delays and decimations for zoom processing was used to evaluate the auto-spectra at lower frequencies. The resulting zoomed auto-spectra of the five bearings can be seen in Figure 68. From Figure 68 it can be seen that the auto-spectrum of Bearing 4 is two orders of magnitude greater than the auto-spectra of the other bearings at low frequencies. The auto-spectra of the friction force of the bearings at 0 Hz are approximately equal in Figure 68, unlike in the plot of the full range of the auto-spectra. This is a result of the detrending, which is done to the friction force signal to make the lower frequency components more apparent in the auto-spectra.

As previously done in plots of the auto-spectra vertical red-dashed lines are used to indicate f_c and its higher harmonics, which for a tracking velocity of 20 mm/s is 2.47 Hz. The plot of the auto-spectrum of the friction force shown in Chapter 7 (see Figure 63 (a)) contained no discernible peaks at f_c or its higher harmonics. The good bearings do not have any discernible peaks at f_c either. However, the bad bearing clearly has peaks in its

auto-spectrum at f_c and its higher harmonics. This indicates that the motion of the balls traveling through the race are the cause of the sticking behavior. It can be concluded from these results that the spectral density of the friction force of a bearing can be used to diagnose its performance.

9.0 CONCLUSION

This research has illustrated that ball-element bearings show periodic fluctuations in friction force for velocity tracking motion. This periodic fluctuation in friction force is caused by the motion of the balls. This was concluded by demonstrating that the frequency of the periodic fluctuation is equal to the frequency of the balls passing a position in the race, which can be approximated by $f_c = \frac{v}{2d_{avg}}$.

To illustrate the relation between the fluctuating friction force and the motion of the balls a testbed was built. The testbed measures friction force, ball passage rate, and position. The velocity error is calculated from the measurement of position, and can show how the periodic fluctuations in friction force acts like a periodic disturbance to the velocity. The testbed measures friction force using a load cell, and measures position using an optical encoder. To detect the motion of the balls in the race an optical sensor was designed and built that would be minimally intrusive to the motion of the balls.

The optical sensor, discussed in this paper, measures light that is reflected off of a ball as it passes the sensing fiber. It was necessary to make some adjustments to the original design of the optical sensor to correct for an instability in the signal, which resulted from the single-mode fiber and the coherent light source. The measurement of the ball passage rate allowed us to determine the frequency of the balls motion, which was compared to the predicted frequency. The measurement of the balls motion was also necessary because it is known that it is possible for the frequency to vary slightly, but it is limited by the physical parameters of the ball bearing.

Before analyzing the test results some qualitative analysis of the system and signals were discussed to give insight into what we may expect from the results. The qualitative analysis discussed the characteristics of the system being studied, and model signals that imitate

attributes that we hoped to observe in the measured signals. The expected output of a system for a given input can be concluded from the block diagram analysis of the system. The analysis of the model signals discussed what we may expect the resulting correlations and spectral densities of the signals to look like, and what we may conclude from them, should they contain the proposed characteristics.

In the correlation calculations, which resulted from measurements taken during tracking velocity tests, the friction force, velocity error, and optical sensor signals were each shown to contain some periodic content with a period of τ_c. The cross-correlations of the signals illustrated that the three signals shared periodic content with a period of τ_c, and that some of the signals had some relative phase. From the correlations it can be concluded that each signal contains periodic content at a period of τ_c, as was expected. This demonstrates that the motion of the balls is affecting the precision of the velocity tracking.

The auto-spectrum of the optical sensor signal showed that the signal contained periodic content with a frequency f_c, while the auto-spectrum of the friction force and the velocity error signals did not appear to have any distinct frequency content. It was odd to see that the friction force and velocity error did not contain distinct periodic content, despite their correlations illustrating otherwise. This was most likely a result of the noise in that range of the spectrum being greater than the magnitude of their periodic content. The cross-spectra between friction force and optical sensor signal, and optical sensor signal and velocity error illustrated that those signals share frequency content with a frequency of f_c. The cross-spectrum of the friction force with the velocity error did not show shared frequency content at f_c. This was most likely because the noise in that range had a greater magnitude than the magnitude of their shared periodic content.

During the velocity tracking tests it was noticed that some ball bearings exhibited a sticking behavior during their motion, where the friction force greatly increased periodically with a period of τ_c and with randomly varying amplitudes. This sticking behavior, which would characterize a bad bearing, was evaluated using the auto-spectrum of the friction force measurement. The bearing that exhibited the discussed sticking behavior had a higher

spectral density at low frequencies, especially at integer multiples of f_c. This illustrated that the balls are the cause of the sticking behavior, and it also emphasized how the motion of the balls are causing periodic fluctuations in the friction force.

BIBLIOGRAPHY

[1] Brian Armstrong-Helouvry. *Control of Machines with Friction*. Kluwer Academic Publishers, 1991.

[2] Julius S. Bendat and Allan G. Piersol. *Random Data Analysis and Measurement Procedures*. John Wiley & Sons, Inc., 2010.

[3] A. Biyiklioğlu, H. Çuvalci, H. Adatepe, H. Ƀas, and M.S. Duman. A new test apparatus and method for friction force measurement in journal bearings under dynamic loading: Part II. *Experimental Techniques*, 29(6):33–36, March 2005.

[4] Brian A. Bucci. *A Practical Method For Friction Compensation In Rapid Point-To-Point Motion*. PhD thesis, University of Pittsburgh, 2011.

[5] Brian A. Bucci, Daniel G. Cole, Jeffrey S. Vipperman, and Stephen J. Ludwick. Friction modeling of linear rolling element bearings in high precision linear stages. In *Proceedings of the American Society American Society for Precision Engineering*, 2009.

[6] Steven C. Chapra and Raymond P. Canale. *Numerical Methods for Engineers*. McGraw-Hill, sixth edition, 2010.

[7] C.A. Coulomb. Théorie des machines simples. *Mémoire de Mathématique et de Physique de l'Académie Royale*, pages 161–342, 1785.

[8] J. de Nicente, J. R. Stokes, and H. A. Spikes. Rolling and sliding friction in compliant, lubricated contact. *Journal of Engineering Tribology*, 220(2):55–63, February 2006.

[9] Duncan Dowson. *History of Tribology*. Wiley, 2 edition, 1998.

[10] Pierre E. Dupont and Eric P. Dunlap. Friction modeling and control in boundary lubrication. In *American Control Conference, 1993*, pages 1910–1915. American Control Conference, June 1993.

[11] Yusaka Fuji. Measurement of force acting on a moving part of a pneumatic linear bearing. *Review of Scientific Instruments*, 74(6):3137–3141, June 2003.

[12] Shigeru Futami, Akihiro Furutani, and Shoichiro Yoshida. Nanometer positioning and its micro-dynamics. *Nanotechnology*, 1(1):31–37, 1990.

[13] Douglas Godfrey. Friction oscillations with a pin-on-disc tribometer. *Tribology International*, 28(2):119–126, 1995.

[14] Avraham Harnoy, Bernard Friedland, and Simon Cohn. Modeling and measuring friction effects. *IEE Controls Systems Magazine*, 2008.

[15] Avraham Harnoy, Bernard Friedland, Richard Semenock, Hanuman Rachoor, and Atif Aly. Apparatus for empirical determination of dynamic friction. In *American Control Conference, 1994*, volume 1, pages 546–550. American Control Conference, June 1994.

[16] D.P. Hess and A. Soom. Friction at a lubricated line contact operating at oscillating sliding velocities. *Journal of Tribology*, 112(1):147–153, January 1990.

[17] Philip C. D. Hobbs. *Building Electro-Optical Systems*. John Wiley & Sons, Inc., 2000.

[18] Craig T. Johnson and Robert D. Lorenz. Experimental identification of friction and its compensation in precise, position controlled mechanisms. *IEEE Transactions On Industry Applications*, 28(6):1392–1398, December 1992.

[19] P. Korpiharju, K. Hanhi, and H. Koivo. Utilization of an industrial robot with a force transducer equipment in measuring friction. In *IECON Proceedings 1991*, volume 2, pages 1055–1060. IEEE, November 1991.

[20] V. Lampaert, F. Al-Bender, and J. Swevers. Experimental characterization of dry friction at low velocities on a developed tribometer setup for macroscopic measurements. *Tribology Letters*, 16(1-2):95–105, February 2004.

[21] V. Lampaert, J. Swevers, and F. Al-Bender. Experimental comparison of different friction models for accurate tracking. In *Proceedings of the 10th Mediterranean Conference On Control and Automation*, 2001.

[22] Ta-Wei Lin, Alireza Modafe, Benjamin Shapiro, and Reza Ghodssi. Characterization of dynamic friction in MEMS-based microball bearings. *IEEE Transactions On Instrumentation and Measurement*, 53(3):2004, June 2004.

[23] Patricia M. McGuiggan, Jun Zhang, and Stephen M. Hsu. Comparison of friction measurements using the atomic force microscope and the surface forces apparatus: the issue of scale. *Tribology Letters*, 10(4):217–223, 2001.

[24] A. J. Morin. New friction experiments carried out at Metz in 1831–1833. *Proc. of the French Royal Academy of Sciences*, 4:1–128, 1833.

[25] Jun Ni and Zhenqi Zhu. Experimental study of tangential micro deflection of interface of machined surface. *Journal of Manufacturing Science and Engineering*, 123:365–367, May 2001.

[26] H. Olsson, K.J. Astrom, C. Canudas de Wit, M. Gafvert, and P. Lischinsky. Friction models and friction compensation. *European Journal Of Control*, 4(3):176–195, 1997.

[27] Alan V. Oppenheim and Ronald W. Schafer. *Discrete-Time Signal Processing*. Pearson Higher Education, Inc., third edition, 2010.

[28] Jiro Otsuka and Tadashi Masuda. The influence of nonlinear spring behavior of rolling elements on ultraprecision positioning control systems. *Nanotechnology*, 9(2):85–92, 1998.

[29] M.K. Ramasubramanian and Steven D. Jackson. A sensor for measurement of friction coefficient on moving flexible surfaces. *IEEE Sensors Journal*, 5(5):844–849, October 2005.

[30] O. Reynolds. On the theory of lubrication and its applications to Mr. Beauchamp tower's experiments. including an experimental determination of the viscosity of olive oil. *Philosophical Transactions of the Royal Society of London*, 177:157–234, 1886.

[31] Daniel Sidobre and Vincent Hayward. Calibrated measurement of the behaviour of mechanical junctions from micrometre to subnanometre scale: The friction force scanner. *Measurement Science and Technology*, 15(2):451–459, January 2004.

[32] R. Stribeck. Kugellager für beliebige Belastungen. *Zeitschrift des Vereines Deutscher Ingenieure*, 1901.

[33] Jan Swevers, Farid Al-Bender, Chris G. Ganseman, and Tutuko Prajogo. An integrated friction model structure with improved presliding behavior for accurate friction compensation. *IEEE Transactions On Automatic Control*, 45(4):675–686, April 2000.

[34] Xiaobo Tan, Alireza Modafe, and Reza Ghodssi. Measurement and modeling of dynamic friction in linear microball bearings. *Journal of Dynamic Systems, Measurement, and Control*, 128(4):891–898, December 2006.